Mitochondria-Lysosome Crosstalk Shapes Metabolic Transition in Neonatal Enterocytes

Gonzalo Herranz,[1,2] Diego Alonso-Larre,[1,2,10] Tamara González,[1,2,10] Laura Akintche,[1,2] Alejandra Ramos-Manzano,[1,2,7] Marta Iborra-Pernichi,[1,2,8], María Velasco de la Esperanza[1,2], Covadonga Díaz-Díaz,[1,2,9] Ian G Ganley,[3] Patricia Boya,[4,5] Sara Cogliati,[6] Nuria Martínez-Martín,[1,2]* and Fernando Martín-Belmonte[1,2,11]**

[1]Program of Tissue and Organ Homeostasis, Centro de Biología Molecular Severo Ochoa, Consejo Superior de Investigaciones Científicas-Universidad Autónoma de Madrid, Madrid, Spain

[2]Intestinal Morphogenesis and Homeostasis Group, Área 3-Cancer, Instituto Ramón y Cajal de Investigación Sanitaria (IRYCIS), Madrid, Spain

[3]MRC Protein Phosphorylation and Ubiquitylation Unit, University of Dundee, Dundee, UK

[4]Dept of Cellular and Molecular Biology, Centro de Investigaciones Biológicas Margarita Salas, CSIC, Madrid, Spain

[5]Department of Neuroscience and Movement Science, Section of Medicine, University of Fribourg, Fribourg, Switzerland

[6]Program of Physiological and Pathological Processes, Centro de Biología Molecular Severo Ochoa, Consejo Superior de Investigaciones Científicas-Universidad Autónoma de Madrid, Madrid, Spain

[7]Present addresses: Immunology Department, Hospital Universitario de La Princesa, Instituto de Investigación Sanitaria (IIS)-Princesa, Madrid, Spain; Medicine Department, School of Medicine, Universidad Autónoma of Madrid, Madrid, Spain

[8]Present address: B Lymphocyte Biology Lab, Centro Nacional de Investigaciones Cardiovasculares (CNIC), Madrid, Spain

[9]Present addresses: Cardiovascular Regeneration Program, Centro Nacional de Investigaciones Cardiovasculares (CNIC), Madrid, Spain; Centro de Investigación Biomédica en Red de Enfermedades Cardiovasculares (CIBERCV), Madrid, Spain

[10]These authors contributed equally

[11]Senior author and Lead contact

*Correspondence: nmartinez@cbm.csic.es

**Correspondence: fmartin@cbm.csic.es

SUMMARY

The neonatal gastrointestinal tract mediates nutrient absorption and the establishment of immune tolerance to commensal microbiota. In early life, lysosome-rich enterocytes (LREs) in the ileum are necessary for the intracellular digestion of maternal milk proteins. However, the molecular mechanisms sustaining their function remain incompletely characterized. Here, we demonstrate that LRE mitochondrial homeostasis and autophagic capacity are critical for efficient nutrient uptake and maintenance of their specialized identity, as disruption of either process leads to premature differentiation into post-weaning enterocytes (PECs) with diminished endolysosomal and metabolic activity. Transcriptomic profiling further revealed that neonatal LREs exhibit a distinctive antioxidant signature, which preserves redox balance and safeguards the expression of the transcriptional regulators MAFB and BLIMP1, both central repressors of the neonatal-to-adult metabolic transition. These findings establish the mitochondria–lysosome axis as a key determinant of LRE function and neonatal metabolic programming. They also provide a mechanistic framework for understanding how organelle dysfunction and redox imbalance may contribute to early-life malnutrition syndromes, such as Kwashiorkor, and suggest therapeutic strategies aimed at preserving mitochondrial and lysosomal integrity.

KEYWORDS

Intestine, Enterocyte, Autophagy, Mitochondria, Lysosome, Neonatal, Metabolic Switch, ROS, Nutrient Absorption, Mouse

43 **INTRODUCTION**

44 The small intestine is a specialized section of the gastrointestinal tract (GIT) engaged in nutrient digestion
45 and absorption, while simultaneously acting as a barrier against harmful substances. It consists of a variety
46 of cell types, with epithelial and immune cells playing key roles in maintaining intestinal function. Through
47 their interactions with one another and the gut microbiota, these cells help create a finely balanced
48 microenvironment that supports both nutritional and immunological functions (Beumer and Clevers, 2021;
49 Choo et al., 2022). The main absorptive epithelial cells in the intestine are called enterocytes. They are the
50 most numerous cells in the intestinal epithelium and, along with secretory epithelial cells (including Paneth,
51 goblet, and enteroendocrine cells), originate from stem cells of the intestinal crypts (Beumer and Clevers,
52 2021).

53 Dietary protein is a macronutrient essential for growth and overall organismal homeostasis. In weaned
54 mammals, protein digestion takes place in the lumen of GIT, where gastric pepsin and intestinal proteases
55 sequentially break down proteins into oligopeptides and free amino acids, which are then absorbed by
56 enterocytes via specific transporters (Henning, 1981, 1985; Rombout et al., 1985).

57 However, in the intestinal lumen of suckling mammals and stomachless fishes, protease activity remains
58 low and protein digestion is incomplete (Henning, 1981, 1985; Rombout et al., 1985). For this reason, their
59 posterior-mid small intestine contains a population of lysosome-rich enterocytes (LREs), formerly referred
60 to as vacuolated enterocytes (Kleinman and Walker, 1984; Park et al., 2019; Rodríguez-Fraticelli et al.,
61 2015). These cells possess a highly developed endolysosomal system, including a prominent lysosomal
62 vacuole (LV), which is capable of internalising and metabolising intact proteins via non-specific fluid-phase
63 processes (pinocytosis) and receptor-mediated endocytosis and membrane adsorption (Fujita et al., 1990;
64 Gonnella and Neutra, 1984; Park et al., 2019; Rombout et al., 1985). Moreover, LREs facilitate the
65 transcytosis of antigens, maternal immunoglobulins, and antibodies across the epithelial barrier while
66 preserving their biological activity, contributing to the immune system development (Kulkarni and Newberry,
67 2019; Rombout et al., 1985). Recent studies have highlighted the nutritional importance of LREs during the
68 neonatal period. Key endolysosomal proteins, whose absence leads to developmental defects, have been
69 identified, including Mucolipins 1 and 3 (Remis et al., 2014), Pllp (Rodríguez-Fraticelli et al., 2015), Mamdc4
70 (also known as endotubin) (Cox et al., 2018) and Dab2 (Park et al., 2019). Despite these findings, the
71 molecular mechanisms that regulate endocytic and lysosomal pathways in LREs are still not fully
72 understood.

73 Autophagy is a conserved lysosome-dependent catabolic pathway that recycles intracellular components
74 and nutrients. This process involves the sequestration of cytoplasmic material into double-membraned
75 autophagosomes, which subsequently fuse with lysosomes for degradation and breakdown. The lipidation
76 of LC3, a key step in autophagosome formation, is mediated by the ATG12–ATG5–ATG16L1 complex (He,
77 2022; Kaur and Debnath, 2015). Mutations in components of this complex have been linked to intestinal
78 pathologies (Foerster et al., 2022; Larabi et al., 2020), and *Atg5*-deficient neonates exhibit increased

79 neonatal mortality under fasting conditions, underscoring the essential role of autophagy during early
80 postnatal life (Kuma et al., 2004). Despite this, the homeostatic role of autophagy throughout the entire
81 neonatal period, particularly in LRE biology, remains unclear.

82 Autophagy plays a crucial role in cellular metabolism and differentiation, primarily through the selective
83 elimination of mitochondria (mitophagy), thereby contributing to the control of reactive oxygen species
84 (ROS) levels (Wang et al., 2023; Zhong et al., 2024). Beyond their role in energy production, mitochondria
85 and ROS also function as key regulators of cell signalling and differentiation (Lennicke and Cochemé, 2021;
86 Morris and Jasper, 2021; Popov, 2023). In the intestinal epithelium, a gradient of increasing mitochondrial
87 mass, activity, and ROS levels has been described along the crypt–villus axis, correlating with higher
88 degrees of cellular differentiation (Rath et al., 2018). However, how mitochondrial homeostasis and ROS
89 dynamics influence the developmental remodelling of enterocytes remains poorly understood. In particular,
90 their role in regulating the metabolic and functional transition of neonatal LREs into post-weaning
91 enterocytes (PECs) has not yet been explored.

92 This study reveals that the mitochondria–lysosome axis is essential for the function and maturation of LREs.
93 We show that LREs rely on high autophagic and mitophagic activity to sustain nutrient absorption and
94 lysosomal integrity, and that disruption of either autophagy (*Atg16*cKO) or mitochondrial homeostasis
95 (*Tfam*cKO) leads to impaired endolysosomal function, oxidative stress, and premature weaning transition
96 through the repression of the transcription factors BLIMP1 and MAFB. These findings establish organelle
97 homeostasis as a critical determinant of neonatal enterocyte identity and provide mechanistic insights into
98 how its disruption contributes to early-life malnutrition.

99

100 **RESULTS**

101 ***Lysosome-rich enterocytes (LREs) display heightened basal autophagy levels essential for***
102 ***absorptive function***

103 Unlike PECs, LREs rely on intracellular digestion within lysosomes to process macromolecular nutrients.
104 This process demands a highly active endolysosomal system that breaks down complex proteins into
105 absorbable units, which confers a particular architecture to LREs (**Figures S1A and S1B**) (Fujita et al.,
106 1990). Autophagy, the cellular mechanism responsible for degrading and recycling cellular components,
107 plays a central role in maintaining lysosomal function and turnover (Yim and Mizushima, 2020). In LREs,
108 elevated basal autophagy may support endolysosomal activity. Exploring this hypothesis could clarify the
109 role of autophagy in the absorption and processing of nutrients in neonates, as well as its contribution to
110 early development.

111 Utilising the GFP-LC3 transgenic mouse model (*GFP-Map1lc3a*$^{TG/+}$) (Mizushima et al., 2004), we visualised
112 autophagosomes as GFP-LC3 positive puncta and monitored autophagy flux via western blot (WB) by
113 assessing the levels of free GFP, a byproduct of lysosomal degradation of GFP-LC3 II (**Figures 1A, 1B and**

114 **S1C**) (Mizushima et al., 2010; Ni et al., 2011). The presence and activity of LREs was determined by probing
115 with mCherry/ fluorescent dextrans that are internalised as a macromolecule by LREs, but not by PECs
116 (**Figures 1A, 1B, S1C, andS1D**) (Park et al., 2019). Following gavage, fluorescent-dextran was rapidly
117 internalised from the lumen into early and late endosomes (**Figure S1D**, arrowheads), accumulating
118 progressively in lysosomal vacuoles (LVs) (**Figure S1D**, arrows). WB analysis was performed on lysates
119 from epithelial cells in both proximal and distal sections of small intestines from GFP-LC3 mice at neonatal
120 stages (P1, P7 and P14), and post-weaning (P21–30). This analysis revealed a proximal-distal gradient of
121 protein absorption and autophagic degradation, mirroring the anterior-posterior intestinal maturation (**Figure**
122 **1B**) (Spence et al., 2011).

123 In the distal intestine, protein absorption preceded the induction of autophagy, with a subtle onset already
124 detectable at P1, although no free GFP signal was observed. By P7, both mCherry uptake and free GFP
125 increased markedly, with a strong accumulation of free GFP (**Figure 1B**, pink rectangle), indicating peak
126 autophagic activity in LREs—coinciding with the establishment of neonatal intestinal features (Hansson et
127 al., 2011). At P14, mCherry absorption persisted in the distal region, while free GFP levels declined, and
128 by weaning (P21) both signals were absent (**Figure 1B**). Quantification of mCherry and free GFP in ileal
129 epithelial lysates at P7 and P21 confirmed these developmental differences (**Figures 1C and S1C**).

130 In contrast, the proximal intestine displayed a different temporal profile. At P1, both mCherry and free GFP
131 were already present, but their levels progressively declined, and at P14 only low residual signals were
132 detectable. Note that undegraded GFP-LC3 forms (I and II) and intermediate degradation products
133 accumulated at P21, in both distal and proximal samples (**Figure 1B**).

134 Given these observations, we conclude that LREs maintain elevated autophagy levels relative to PECs,
135 most probably as a result of their enhanced lysosomal function. To explore the consequences of autophagy
136 disruption in these cells during early development, we utilised a genetic mouse model. ATG16L1 is crucial
137 for both autophagosome formation and LC3 lipidation, two processes essential for autolysosomal
138 degradation (Fujita et al., 2008; Mizushima et al., 2003). This gene has been extensively studied for its
139 association with inflammatory bowel diseases (Foerster et al., 2022; Larabi et al., 2020); nonetheless, its
140 specific role in LRE functionality during the neonatal period remains largely unexplored. For this, we crossed
141 with the *Atg16l1*$^{fl/fl}$ mice (Hwang et al., 2012), with mice expressing the *Villin-creER*^{T2} transgene (el Marjou
142 et al., 2004). This breeding strategy generated an *Atg16l1* knockout offspring in which the *Atg16l1* gene is
143 conditionally deleted in the intestinal epithelium upon administration of tamoxifen (*Atg16*cKO) (**Figure 1D**).

144 Initially, we validated our model via WB analysis by measuring the levels of ATG16L1 and LC3 isoforms
145 (cytoplasmic LC3-I and lipidated LC3-II) in the ileum of both WT and *Atg16*cKO mice at P14 (**Figures 1D**
146 **and 1E**). We observed a significant reduction in ATG16L1 protein levels across all *Atg16*cKO samples,
147 which led to a corresponding decrease in LC3-II/LC3-I ratio (**Figure 1D**). Specifically, our data showed an
148 84.5% reduction in ATG16L1 protein levels and an approximately 8-fold decrease in LC3-II/LC3-I ratio
149 (**Figure 1E**). Furthermore, we observed elevated levels of P62, indicating a reduction in its autophagy-

150 dependent degradation (**Figures 1D and 1E**). These outcomes are consistent with previous results (Cadwell
151 et al., 2008).

152 Subsequently, we examined the developmental trajectory of *Atg16*cKO mice, with a primary focus on their
153 intestinal morphology and function. We observed that the mice reached the post-weaning stage (P30)
154 without apparent issues, showing no weight defects throughout early postnatal development (**Figure S2A**).
155 No significant changes were noted in the length or histological state of the small and large intestines
156 (**Figures S2B and S2C**). However, a reduction in villus length and a decrease in the number of Goblet cells
157 (GCs) were detected in the ileum at P14 (**Figures 1F and 1G**), along with mild oedema at P30, an indicator
158 of inflammation (**Figure S2D**, arrowhead). Inspired by these observations, we quantified specific intestinal
159 epithelial (IEC) and immune cell subpopulations in the ileum of *Atg16*cKO mice at both neonatal and post-
160 weaning stages using flow cytometry (**Figures S2E and S2F**). For this, we applied specific markers to
161 identify various IEC subtypes, including enterocytes and their progenitors (EC), Goblet cells (GC), Paneth
162 cells (PC), and enteroendocrine cells (EEC) (Asano et al., 2017) (**Figure S3**, middle row). We also focused
163 on cells related to innate immunity (IIC), such as CD11b+ cells (including NK cells, granulocytes, and
164 macrophages/monocytes), as well as adaptive immunity, encompassing B lymphocytes (B cells) and CD4+
165 T helper cells (Th cells). We observed an increase in IIC and IEC populations during the neonatal period,
166 accompanied by a concurrent decrease in GC and EEC in adult IECs (**Figure S2E**). In contrast, post-
167 weaning samples showed a rise in B cells, stabilization in IIC and IEC levels, an increase in GC, and a
168 decrease in PC and EEC (**Figure S2F**). These results corroborate our histological findings regarding GCs
169 and inflammation.

170 Next, we investigated the effect of autophagy inhibition on the absorption of macromolecules in the ileum.
171 We gaveged rhodamine B–dextran (Rd-dextran) as a probe in *Atg16*cKO and WT mice as controls (**Figure**
172 **1H**). Our analysis differentiated between the apical and basal regions of enterocytes to assess the
173 sequential entry of Rd-dextran, according to the internalization dynamics observed in these cells (**Figure**
174 **S1D**). Confocal microscopy demonstrated that at P7, *Atg16*cKO enterocytes internalized Rd-dextran
175 similarly to WT counterparts. Nevertheless, it is worth noting that in *Atg16*cKO enterocytes, Rd-dextran
176 levels were slightly elevated in the apical region but reduced in the basal region compared to WT (**Figure**
177 **1H**). This observation suggests a deceleration in the internalisation of macromolecules during this
178 developmental period. Next, at P14, *Atg16*cKO enterocytes exhibited a complete abrogation of
179 macromolecule absorption, resembling post-weaning enterocytes and indicating an advancement in
180 intestinal maturation (**Figure 1H**). To further validate the observed decrease in absorption at P14, we probed
181 neonates from both WT and *Atg16*KO groups with mCherry and quantified the internalised mCherry in the
182 ileum via WB. The results confirmed consistently lower levels of nutrient absorption in *Atg16*KO mice
183 (**Figures 1I and 1J**). Altogether, we conclude that blocking autophagy severely disrupts macromolecule
184 absorption in the neonatal ileum.

185 To further investigate this role autophagy in macromolecule absorption, we examined the expression of the
186 endocytic genes *Dab2*, *Amn*, and *Mamdc4*, as well as the lysosomal genes *Mcoln3*, *Lamp2*, and *Ctsl1*.
187 Previous studies have demostrated the specific role of these genes on the endolysosomal function of LREs
188 (Cox et al., 2018; Park et al., 2019; Remis et al., 2014). Indeed, we validated their expression during early
189 postnatal intestinal development (**Figure 2A**). As expected, an upregulation of these genes was observed
190 in distal samples at P7, coinciding with the presence of LREs (**Figure 2A**). Moreover, a proximodistal
191 expression pattern was observed, consistent with the antero-posterior maturation of the intestine (Spence
192 et al., 2011) (**Figure 2A**).

193 Then, we studied the mRNA expression of *Dab2*, *Mcoln3*, and *Lamp2* genes in both the proximal and distal
194 regions of the small intestines of WT and *Atg16*cKO mice at P7 and P14 (**Figures 2B and S2G**). Since LREs
195 predominantly localise in the distal region, the proximal segment was also analysed to assess potential
196 compensatory mechanisms. In distal *Atg16*cKO samples at P7, mRNA levels of these LRE markers were
197 significantly reduced (**Figure 2B**), while the proximal region showed no significant changes compared to
198 WT mice (**Figure S2G**). By P14, a substantial reduction in gene expression was evident in both proximal
199 and distal *Atg16*cKO mice samples (**Figures 2B and S2G**). Additionally, we analysed *Amn*, *Mamdc4,* and
200 *Ctsl1* mRNA expression in the ileum at P14, finding lower expression levels in the *Atg16*cKO samples
201 (**Figure S2H**).

202 To delve deeper into the protein levels of Dab2, we performed WB and immunofluorescence (IF) analysis
203 in the ileum of *Atg16*cKO mice at P7 and P14. While P7 samples exhibited reduced mRNA expression
204 (**Figure 2B**), Dab2 protein levels remained comparable to WT; however, by P14, a marked reduction in
205 Dab2 was observed in *Atg16*cKO samples (**Figures 2C–2F**).

206 Furthermore, we assess the lysosomal occupancy and content in the apical and basal regions of WT and
207 *Atg16*cKO ileal enterocytes using confocal microscopy with an anti-LAMP1 antibody as a lysosomal marker,
208 as the *Lamp1* and *Lamp2* genes exhibit similar expression patterns (data not shown). Post-weaning (P21–
209 30) WT mice were used as controls (**Figures 2G and 2H**). At P7, both WT and *Atg16*cKO enterocytes
210 exhibited comparable lysosomal occupancy and content, with peak intensity observed in both conditions.
211 However, by P14, while lysosomal occupancy remained similar, *Atg16*cKO enterocytes demonstrated
212 reduced intensity in both the apical and basal regions (**Figures 2G and 2H**). Magnified images also revealed
213 that lysosomes in *Atg16*cKO enterocytes were smaller in P14 neonates, resembling those of PECs (**Figure**
214 **2G**, arrowheads). This reduction in lysosomal content in *Atg16*cKO P14 ileum was further confirmed by WB
215 analysis (**Figures 2I and 2J**).

216 In summary, our results indicate that autophagy plays a crucial role in preserving endolysosomal
217 homeostasis of LREs. Disruption of autophagy in LREs using the *Atg16*cKO mice results in significant
218 defects in macromolecule uptake and lysosomal function, accompanied by the downregulation of key
219 endocytic and lysosomal genes, particularly in the distal ileum of late neonatal mice. These outcomes
220 highlight the importance of autophagy in maintaining LRE function and, consequently, ensuring proper

221 postnatal development. However, the precise mechanisms by which autophagy exerts its effects remain
222 unclear.

223

224 ***LREs show a significant induction of mitophagy to control mitochondrial homeostasis***

225 To elucidate the primary type of autophagy in neonatal enterocytes, we defined the gene expression
226 signature of LREs through bulk RNA sequencing. Leveraging the high levels of macromolecular absorption
227 and autophagy in LREs, we probed neonatal GFP-LC3 mice (P7) with Rd-dextran and isolated LREs from
228 the cellular suspension of the ileum by fluorescence-activated cell sorting (FACS), selecting them as the
229 epithelial cells with high levels of autophagy and Rd-dextran (Dextran^{+}GFP^{high}). Moreover, to highlight their
230 genetic neonatal signature, LREs were compared to post-weaning enterocytes (PECs) from mice (P42).
231 Following RNA extraction, we conducted next-generation sequencing (NGS) analysis (**Figures 3A and**
232 **S4A**).

233 We detected a total of 1,537 differentially expressed genes (DEGs), of which 1,036 were upregulated and
234 501 were downregulated in LREs (**Figure 3B**). Differential expression analysis and principal component
235 analysis demonstrated that each population exhibited unique enrichment signatures (**Figures S4B and**
236 **S4C**). The computational method of over-representation analysis (ORA) identified which biological
237 processes were overrepresented in the differentially expressed genes (DEGs) (Boyle et al., 2004). The
238 majority of differentially regulated pathways were associated with lysosomal function, nutrient absorption,
239 processing, and transport (**Figures 3C, 3D, and S4D**). These findings are consistent with earlier RNA-Seq
240 data from LREs in zebrafish (Park et al., 2019). Nonetheless, the regulation of lipid metabolism pathways
241 differed (**Figure 3C and S4D**), suggesting that mammalian LREs significantly modulate these pathways to
242 process lipids from maternal milk.

243 Among the most upregulated genes were those associated with endocytosis, such as *Mamdc4*, *Dab2*, and
244 *Amn*, as well as lysosome-associated genes like *Mcoln3* and *Ctsl1* (**Figure 3B**). The upregulation of *Dab2*,
245 *Amn*, and *Lamp2* genes corresponded with previously published ileum transcriptome data from mice and
246 zebrafish (Park et al., 2019). Additionally, the overexpression of *Mamdc4* and *Mcoln3* genes also aligned
247 with earlier results in LREs from rodents (Remis et al., 2014; Wilson et al., 1991). We confirmed elevated
248 levels of *Ctsl1* mRNA expression and lysotracker staining in LREs compared to PECs in WT mice (**Figures**
249 **S4E and S4F**), which validated the RNA-Seq data and ensured that the lysosome-associated pathway was
250 not positively regulated due to the selection of neonatal enterocytes with high autophagy levels.

251 Interestingly, the 'positive regulation of autophagy of mitochondrion ' and 'mitochondrial outer membrane'
252 pathways appeared significantly enriched in LREs (**Figures 3C and 3D**). These outcomes, along with the
253 upregulation of several genes involved in mitophagy, such as *Bnip3*, *Atg10*, and *Map1lc3a* (**Figure 3B**) (Li
254 et al., 2022; Yang et al., 2024), indicated that mitophagy is a significant component of the elevated
255 autophagic activity observed in LREs. To explore this hypothesis, we examined the mRNA expression of

256 the canonical mitophagy genes *Prkn* (Parkin) and *Pink1* (Picca et al., 2023), together with *Bnip3* as a
257 control, in ileal samples from WT mice across developmental stages (E18.5-P42). While *Bnip3* exhibited a
258 progressive decrease in expression throughout development, *Prkn* and *Pink1* showed upregulation in
259 neonatal samples, especially *Prkn* (**Figure 3E**). Moreover, we observed that LREs displayed increased
260 Parkin protein levels compared to PECs through IF (**Figure 3F**).

261 Next, we assessed mitophagy in LREs and PECs using the fixable *mito*-QC reporter C57BL/6J mouse
262 (McWilliams et al., 2016), which ubiquitously expresses a chimeric protein consisting of pH-insensitive
263 mCherry, a pH-sensitive GFP, and the mitochondria-targeting sequence (MTS) from the outer mitochondrial
264 membrane protein FIS1 (amino acids 101–152). This allowed us to differentiate between cytoplasmic
265 mitochondria ($mCherry^{+}GFP^{+}$) and mitochondria degraded by mitophagy in lysosomes ($mCherry^{+}GFP^{-}$)
266 (**Figure 3G**). Confocal images of LREs revealed a high concentration of red-fluorescent mitochondria inside
267 their endolysosomal system (**Figures 3H and 3I**). In fact, when we inhibited autophagic flux by treating the
268 neonates with the protease inhibitor Leupeptin (40 mg/kg for 16 hours) (Jiménez-Loygorri et al., 2024), we
269 observed a significant expansion of LVs and a considerable accumulation of red-only mitochondria within
270 them (**Figure 3H**, arrows; **and 3I**). In contrast, PECs exhibited fewer red mitochondria in lysosomes and a
271 uniform distribution of yellow mitochondria throughout the cytoplasm (**Figures 3H and 3I**).

272 Thus, we confirmed the high mitophagic activity of LREs, suggesting severe impairment of mitophagy and
273 mitochondrial integrity in *Atg16*cKO enterocytes. Indeed, we found that mRNA expression levels of both
274 *Bnip3* and *Prkn* (**Figure 3J**), along with Parkin protein levels (**Figure 3K**), were significantly lowered in
275 neonatal *Atg16*cKO enterocytes. To further investigate the robust mitophagic activity of LREs, we generated
276 an autophagy-deficient *mito*-QC mouse line (*mQ-Atg16*cKO) to evaluate their status. We observed that in
277 *Atg16*cKO LREs exhibited reduced mitochondrial mass within the lysosomes (**Figures 3L and 3M**),
278 consistent with the low mitophagy observed in PECs (**Figures 3L**, lower panels). Therefore, the suppression
279 of autophagy in LREs results in the downregulation of mitophagy-related genes and a reduced uptake of
280 mitochondria into lysosomes.

281 Motivated by these results, we addressed the mitochondrial status of *Atg16*cKO mice. Using transmission
282 electron microscopy (TEM), we analysed mitochondrial damage, quantity, and morphology in ileal
283 enterocytes from neonatal *Atg16*cKO mice (**Figure 4A–4C**). Mitochondria were categorized into three
284 classes based on electron density, cristae appearance, matrix loss, and outer membrane integrity: class I
285 (normal), class II (partially affected), and class III (damaged) (**Figure 4B**) (Moschandrea et al., 2023). For
286 each class, the number, percentage, area, and dimensional ratio (aspect ratio, AR: major axis/minor axis)
287 were quantified (**Figure 4C**). The data showed that number and percentage of mitochondria within each
288 class were similar across both WT and *Atg16*cKO enterocytes. However, while class I mitochondria in
289 *Atg16*cKO enterocytes exhibited a smaller area and a higher AR, class III mitochondria showed a larger
290 area, suggesting an accumulation of damaged mitochondrial mass due to impaired autophagy (**Figure 4C**).

291 To further validate the mitochondrial status, we performed flow cytometry on neonatal *Atg16*cKO
292 enterocytes using mitochondrial probes *ex vivo*: Mitotracker Green for mitochondrial mass, Mitotracker Red
293 CMXROS for membrane potential, and CM-H_2DCFDA for ROS (Asano et al., 2017; Iborra-Pernichi et al.,
294 2024). This analysis confirmed an increase in mitochondrial mass, membrane potential, and ROS in
295 *Atg16*cKO enterocytes (**Figure 4D**). In conclusion, the inhibition of mitophagy in LREs leads to an increased
296 in the mass of dysfunctional mitochondrial.

297 Collectively, mitophagy represents a significant component of the heightened autophagic activity observed
298 in LREs. Its inhibition not only contributes to the mitochondrial defects seen in neonatal *Atg16*cKO
299 enterocytes but may also account for the impairment of their endolysosomal system. These findings
300 highlight a compelling link between the mitochondria-lysosomes crosstalk and neonatal development, as
301 well as the associated metabolic adaptations.

302

303 ***Dysfunction of the mitochondria-lysosome axis in the neonatal epithelium causes an early***
304 ***metabolic switch dependent on BLIMP1 and MAFB***

305 An interesting phenotype observed in neonatal *Atg16*cKO enterocytes was their resemblance to PECs,
306 particularly in terms of the abrogation of macromolecule absorption and the reduction in endolysosomal
307 system functionality. This phenotype could suggest an acceleration of their metabolic transition. At the end
308 of lactation, the mammalian intestine becomes capable of digesting nutrients extracellularly, replaces LREs
309 with PECs (without LVs), and regulates the expression of enzymes to adapt to the new solid diet (Henning,
310 1981; Skrzypek et al., 2007). Previous studies have demonstrated that the transcriptional factors BLIMP1,
311 MAFB, and c-MAF (two members of the Maf family of proteins) mediate the metabolic shift in enterocytes
312 during neonatal development (Bara et al., 2022; Harper et al., 2011; Muncan et al., 2011). At weaning,
313 Blimp1 expression decreases, leading to a downregulation of neonatal enzymes such as β-galactosidase
314 (Glb1) and argininosuccinate synthase 1 (Ass1), and an increase in expression of adult enzymes, including
315 sucrase-isomaltase (Sis), trehalase (Treh), and arginase 2 (Arg2) (Harper et al., 2011; Muncan et al., 2011).
316 Similarly, early inhibition of MAFB and c-MAF in neonatal intestine induces a comparable metabolic switch
317 (Bara et al., 2022).

318 Our RNA-Seq analysis comparing LREs and PECs confirmed these dynamics: LREs expressed higher
319 levels of *Mafb*, *Blimp1*, *Glb1*, and *Ass1*, along with a decrease of *Sis*, *Treh*, and *Arg2* (**Figure S5A**). *c-maf*
320 showed no significant differences (**Figure S5A**), though transient regulation at specific neonatal stages
321 cannot be excluded. Consistently, RT-qPCR analysis of proximal and distal small intestine samples from
322 WT mice across development (E18.5–P42) revealed neonatal enrichment of transcription factors and
323 neonatal enzymes, whereas post-weaning samples displayed the opposite profile, with strong induction of
324 adult enzymes (**Figures S5B and S5C**). *Arg2* expression levels closely paralleled those of Sis and Treh
325 (data not shown).

326 To investigate whether autophagy mediated by ATG16 contributes to this transition, we analyzed the
327 temporal expression patterns of these genes in our model. Gene expression analysis revealed a moderate
328 downregulation of the transcription factor genes *Blimp1* and *Mafb*, except for *c-maf*, as well as a more
329 pronounced downregulation of neonatal enzyme genes *Ass1* and *Glb1*. In contrast, there was an
330 upregulation of adult enzyme genes *Treh*, *Sis*, and *Arg2* (**Figure 5A**). Similarly, confocal microscopy
331 analysis revealed reduced levels of MAFB, BLIMP1 (**Figures 5B and 5C**), and ASS1, along with increased
332 levels of TREH in neonatal *Atg16*cKO enterocytes (**Figures 5D and 5E**). This later result was also confirmed
333 by WB analysis in neonates (**Figure 5F and 5G**). In summary, *Atg16*cKO mice advance their metabolic
334 transition in enzymes regulated by MAFB/BLIMP1 in their neonatal epithelium.

335 Next, we studied the metabolic profiles of neonatal enterocytes from *Atg16*cKO mice, in comparison with
336 neonatal and post-weaning WT mice. In order to evaluate deeply the metabolic transition during the
337 neonatal development and the impact of autophagy, we used a pioneer technique called Met-flow. The Met-
338 Flow technique is a flow cytometry-based method that examines the metabolic state of cells by evaluating
339 the levels of rate-limiting enzymes across key metabolic pathways. Specifically, we studied ASS1 and GLS
340 as markers of amino acid (AA) metabolism, HK1 as a marker of glycolysis, CPT1A and ACAC as markers
341 of fatty acid (FA) metabolism, CS and IDH2 for the tricarboxylic acid (TCA) cycle, and ATP5 for oxidative
342 phosphorylation (OXPHOS) (Ahl et al., 2020; Iborra-Pernichi et al., 2024) (**Figure S5D**). Met-Flow analysis
343 revealed higher expression of most metabolic pathways in LREs compared to PECs (**Figure S5E**), reflecting
344 a their hyperconsumptive signature aligned with the high energy demands of this developmental period
345 (Hulzebos and Sauer, 2007). Notably, neonatal *Atg16*cKO enterocytes exhibited a moderate reduction in
346 enzyme protein levels, positioning them between those of WT neonates and post-weaning mice (**Figure**
347 **5H**). This intermediate profile is indicative of a globally accelerated metabolic transition toward a more
348 mature state.

349 In summary, our results reveal that autophagy is essential for coordinating mitochondrial and metabolic
350 remodeling during neonatal ileum development and the weaning transition. Suppression of autophagy
351 perturbs endolysosomal and mitochondrial integrity, thereby altering the transcriptional control of LREs.
352 Consequently, LREs undergo a premature metabolic switch, marked by MAFB and BLIMP1 dysregulation
353 and reduced activity of key metabolic pathways.

354

355 ***Mitochondrial homeostasis is critical for maintaining LREs function and their metabolic transition***

356 After identifying mitochondrial homeostasis defects as a downstream consequence of impaired
357 endolysosomal function in the *Atg16*cKO model, we next investigated whether mitochondria themselves
358 play an intrinsic role in sustaining LRE integrity. For this purpose, we used the *Tfam*cKO mouse model
359 (*Tfam*$^{fl/fl}$*/Villin-creER*^{T2}), which enables inducible deletion of Tfam in the neonatal intestinal epithelium. This
360 approach allowed us to directly test whether mitochondrial dysfunction is sufficient to compromise
361 lysosomal homeostasis in LREs.

362 TFAM is a transcription factor that regulates the transcription and replication of mitochondrial DNA (mtDNA)
363 (Campbell et al., 2012). While the role of mitochondria in maintaining intestinal homeostasis has been
364 extensively explored (Rath et al., 2018), and the consequences of Tfam deletion have been reported in
365 both embryonic and adult intestinal epithelium (Srivillibhuthur et al., 2018), its specific contribution during
366 the neonatal stage, and particularly in nutrient absorption and processing by LREs, remains unexplored.

367 We first characterized the general phenotype of *Tfam*cKO pups during the neonatal period. These mice
368 exhibited developmental defects, a generally poor appearance, and significantly reduced body weight,
369 starting around P8, which ultimately compromised their survival and prevented successful weaning (**Figures**
370 **6A–6C**). Given the severity of the phenotype and in adherence with animal welfare guidelines, euthanasia
371 was performed after two consecutive days without weight gain or upon observing weight loss of around
372 10% (**Figure 6C**). Based on the timing of euthanasia, we defined two experimental groups: mice euthanised
373 between P9–P11 (hereafter referred to as P10), and those euthanised between P13–P15 (hereafter
374 referred to as P14). In the ileum of both groups, we confirmed a marked reduction in *Tfam* mRNA expression
375 (**Figure 6D**), accompanied by decreased levels of mtDNA, as assessed through the quantification of
376 electron transport chain-encoded genes including *mt-Nd1*, *mt-Co*1, *mt-Co2*, and *mt-Atp6* (**Figure S6A**). In
377 addition, *Tfam* deletion resulted in a selective loss of mitochondrial gene expression at P10 (*mt-Nd1*, *mt-*
378 *Co2*), while nuclear *Sdha* expression was unaffected (**Figure S6B**). We also observed a significant reduction
379 in MTCO1 (complex IV subunit) protein levels in ileal sections of *Tfam*cKO at P14 (**Figures S6C and S6D**).
380 These results validated our neonatal *Tfam*cKO model and were consistent with findings from other *Tfam*KO
381 models (Baixauli et al., 2015; Chung et al., 2019; Iborra-Pernichi et al., 2024).

382 Further histological examination of the distal small intestine of *Tfam*cKO mice at P10 and P14 revealed
383 substantial structural alterations. The epithelium exhibited clear signs of disorganization and inflammation,
384 characterised by notably shorter, malformed villi, oedema, reduced GCs, and a thicker submucosa and
385 lower mucosa (**Figures S6E–S6H**). Enterocytes also exhibited aberrant vacuoles, suggesting dysfunctions
386 in nutrient processing (**Figure S6E**, arrows).

387 Moreover, flow cytometry analysis of the ileum at P10 and P14 revealed increased percentages of IIC (B
388 cells, and Th cells) in *Tfam*cKO samples (**Figures S6I–S6K**). Given the elevated OXPHOS activity
389 characteristic of intestinal stem cells (ISCs) (Rodríguez-Colman et al., 2017), we assessed ISC populations
390 in ileal sections from P10 and P14 *Tfam*cKO mice via Olfm4 immunofluorescence (**Figure S6L**, arrows),
391 which revealed a marked reduction in Olfm4^{+} crypts (**Figures S6M**). Additionally, lysozyme staining showed
392 a striking increase in mislocalised PCs (**Figures S6N and S6O**). These PCs exhibited mislocalization,
393 aberrant morphologies and enlarged granules, indicative of disrupted crypt architecture and compromised
394 ISC niche homeostasis (**Figure S6N**, arrowheads).

395 With the systemic and intestinal phenotypes of *Tfam*cKO mice defined, we next investigated how loss of
396 TFAM affects mitochondrial homeostasis in LREs. Firstly, mitochondria from *Tfam*cKO enterocytes at P10
397 and P14 were analyzed by TEM, following the same approach previously used in *Atg16*cKO mice. At P10,

398 *Tfam*cKO enterocytes displayed more class I and II mitochondria, with reduced area and AR (**Figures 6E,**
399 **6F, and S6P**). By P14, damaged class III mitochondria increased while class I mitochondria decreased in
400 number, size, shape and AR (**Figures 6E, 6F, and S6P**). This progressive mitochondrial damage resembles
401 that observed in a previously described *Tfam*KO model in renal epithelial cells (Chung et al., 2019). These
402 data were corroborated by subsequent flow cytometry analysis, which revealed increased mitochondrial
403 mass, membrane potential, and ROS levels in neonatal *Tfam*cKO enterocytes (**Figure 6G**), features
404 reminiscent of those observed in TFAM-deficient lymphocytes (Baixauli et al., 2015; Iborra-Pernichi et al.,
405 2024).

406 In summary, deletion of *Tfam* in the neonatal intestinal epithelium severely disrupted mucosal structure and
407 function, leading to developmental defects that culminated in early mortality. Specifically, in LREs, TFAM
408 loss caused the accumulation of damaged mitochondria and increased oxidative stress.

409 We next investigated whether mitochondrial dysfunction could similarly drive an accelerated metabolic
410 transition in neonatal enterocytes, as observed in the *Atg16*cKO model. The microscopy analysis indicated
411 a reduction in the expression levels of BLIMP1 and MAFB, with a more pronounced decrease in BLIMP1
412 (**Figures 6H and 6I**). As a result, we also observed lower levels of ASS1 and elevated expression of TREH
413 in the *Tfam*cKO enterocytes (**Figures 6J and 6K**). These results were further supported by gene expression
414 analyses of metabolic transition genes that are regulated by BLIMP1, MAFB, and c-MAF. We obtained a
415 progressive downregulation of *Mafb*, *c-maf*, *Blimp1*, *Ass1,* and *Glb1*, accompanied by an upregulation of
416 *Treh*, *Sis*, and *Arg2* at P14 (**Figure S7A**). Finally, the activity of key metabolic pathways was assessed in
417 neonatal *Tfam*cKO enterocytes using Met-Flow (Ahl et al., 2020; Iborra-Pernichi et al., 2024), revealing a
418 marked reduction in nearly all metabolic proteins, except for ATP5A (**Figure 6L**), which was increased,
419 possibly due to mitochondrial accumulation or as a compensatory response to mitochondrial dysfunction.
420 Taken together, these findings indicate that neonatal *Tfam*cKO enterocytes undergo a premature metabolic
421 transition, resembling the metabolic profile of PECs.

422 Following the analysis of mitochondrial defects in TfamcKO neonatal enterocytes, we next investigated
423 whether impaired mitochondrial function also perturbs the endolysosomal system of LREs. Although
424 lysosome–mitochondria crosstalk has been predominantly characterized in the context of mitophagy, our
425 findings suggest a reciprocal layer of regulation, whereby mitochondria control lysosomal biogenesis and
426 function. This bidirectional communication implies that mitochondrial dysfunction not only disrupts energy
427 metabolism but also secondarily compromises lysosomal integrity, thereby exacerbating the metabolic and
428 absorptive defects observed in neonatal *Atg16*cKO enterocytes. Indeed, neonatal *Tfam*cKO enterocytes
429 exhibited a complete loss of Rd-dextran uptake (**Figures 6M and 6N**) and a progressive downregulation of
430 the endocytic genes *Dab2*, *Amn*, and *Mamdc4* (**Figures S7B–S7D**). Subsequently, we characterised a
431 gradual reduction in the expression of lysosomal genes *Lamp2*, *Mcoln3*, and *Ctsl1* (**Figure S7E**),
432 accompanied by a decrease in lysosomal content and size (**Figures 6M, 6O, S7F and S7G**). Thus, neonatal

433 *Tfam*cKO enterocytes recapitulated the phenotype observed in the *Atg16*cKO model, validating a reciprocal
434 interaction between mitochondria and lysosomes in LREs.

435 In conclusion, the *Tfam*cKO model enabled us to establish a bidirectional relationship between mitochondria
436 and lysosomes by recapitulating the endolysosomal defects observed in autophagy-deficient neonatal
437 enterocytes. Furthermore, we confirmed that mitochondrial and lysosomal dysfunction drive an early
438 metabolic switch in LREs. These alterations, alongside epithelial inflammation, developmental delay, and
439 premature death, position the *Tfam*cKO model as a valuable tool for investigating the pathophysiology of
440 childhood malnutrition.

441

442 ***Antioxidant activity in LREs modulates the onset of metabolic switch***

443 After defining the metabolic switch underlying neonatal development, and the early metabolic switch in both
444 *Atg16*cKO and *Tfam*cKO models, we focused on uncovering the mechanisms responsible for this
445 phenotype. The observation that both *Atg16*cKO and *Tfam*cKO models presented heightened ROS levels
446 in enterocytes (**Figures 4D and 6G**) suggested that redox dysregulation may underlie their accelerated
447 metabolic maturation. Indeed, the high mitophagic activity observed in LREs may contribute to the control
448 of ROS (Wang et al., 2023; Zhong et al., 2024). Previous studies have shown that oxidative stress has
449 been reported to repress *c-maf* expression (Chen et al., 2015) and that antioxidant treatment can induce
450 *Blimp1* expression (Qi et al., 2020). Therefore, we hypothesise ROS regulation could represent a critical
451 mechanism for controlling the timing of the metabolic transition in LREs.

452 We found that LREs exhibited significantly higher levels of mitochondrial ROS (mROS) compared to PECs
453 (**Figure 7A**), possibly reflecting their elevated OXPHOS activity (Murphy, 2008). In contrast, total ROS levels
454 were lower in LREs than in PECs (**Figure 7A**), indicating the presence of mechanisms that tightly regulate
455 oxidative stress.

456 Then, we further explored our LREs vs PECs RNA-Seq dataset analysis to identify additional pathways
457 involved in ROS regulation. Numerous pathways related to ROS, ROS response, and antioxidant activity
458 stood out (**Figure 7B and 7C**). Further, there was an overexpression of genes for the antioxidant enzymes
459 Glutathione Peroxidase-3 (Gpx3) and Catalase (Cat) (not shown), suggesting that these antioxidants could
460 be reducing ROS levels in LREs. Indeed, we observed that neonatal ileal samples showed induction of
461 *Gpx3* and *Cat* expression compared to the embryo and post-weaning ileal samples, with the most drastic
462 changes in *Gpx3* (**Figure 7D**). Moreover, in both *Atg16*cKO and *Tfam*cKO neonates, *Gpx3* and *Cat*
463 expression were significantly decreased in the ileum (**Figure 7E and 7F**), and GPX3 protein levels were
464 likewise reduced, as shown by IF (**Figure 7G-J**). Thus, oxidative stress may act as a trigger for the metabolic
465 transition in LREs. To validate this hypothesis, neonatal mice were treated with hydrogen peroxide (H_2O_2)
466 to induce oxidative stress (Liang et al., 2024). mRNA expression analysis revealed a downregulation of the
467 transcription factors *Blimp1*, *Mafb*, and *c-maf*, alongside an upregulation of adult enzymes such as *Treh*

468 and *Arg2*. However, the expression of neonatal enzyme genes *Ass1* and *Glb1* remained unchanged (**Figure**
469 **7K)**. Subsequently, we characterised a reduction of BLIMP1 and ASS1 levels by both IF and flow cytometry
470 (**Figure 7L–7N**), while TREH expression was found to be increased (**Figure 7L and 7M**).

471 The data collectively suggest that elevated antioxidant activity is a key characteristic of LREs. When this
472 antioxidant function is compromised in neonatal *Atg16*cKO and *Tfam*cKO enterocytes, alongside
473 mitochondrial dysfunction, the oxyidative stress rise. This increase in ROS contributes to the repression of
474 genes such as *Blimp1*, *Mafb*, and *c-maf*, ultimately triggering an early metabolic transition (**Figure 7O**).
475 Therefore, this study emphasizses the critical role of mitochondrial-lysosomal coordination in mitigating
476 oxidative stress and regulating the transcriptional programs essential for neonatal intestinal development.
477 Additionally, it paves the way for future research into therapeutic strategies aimed at restoring mitochondria-
478 lysosome homeostasis and redox balance in early gut disorders.

479

480 **DISCUSSION**

481 In this work, we have elucidated new molecular mechanisms fundamental to the function and differentiation
482 of mammalian LREs, highlighting the role of the mitochondria-lysosome axis. Disruption of autophagy in
483 the neonatal gut, either through *Atg16*cKO or mitochondrial dysfunction via *Tfam*cKO, resulted in defective
484 nutrient absorption and a reduction in lysosomal content. Most importantly, *Tfam*cKO neonates exhibited
485 weight loss and premature death, resembling hallmarks of infant malnutrition. Notably, the early enzymatic
486 maturation of *Atg16*cKO and *Tfam*cKO enterocytes indicates a direct connection between autophagic and
487 mitochondrial processes in enterocytic maturation. Additionally, the associated increase in ROS observed
488 in both models may contribute to this metabolic switch by suppressing the expression of transcription factors
489 BLIMP1, MAFB, and c-MAF. These findings are consistent with our transcriptomic data, which reveal
490 upregulation of mitophagy- and antioxidant-related pathways in LREs compared to PECs, supporting the
491 concept that mitochondrial quality control and redox homeostasis are defining features of LRE identity and
492 function. Taken together, our outcomes offer interesting mechanistic insights into the mitochondria-
493 lysosome crosstalk and its role in postnatal intestinal physiology, with implications for understanding the
494 pathophysiology of neonatal malnutrition and related disorders.

495 Autophagy and endocytosis are vesicle-mediated pathways that converge at the lysosome to degrade and
496 recycle intra- and extracellular components. These processes intersect at multiple stages (vesicle
497 formation, trafficking, and fusion) and share several key regulators. Mounting evidence indicates reciprocal
498 dependence between these processes (Birgisdottir and Johansen, 2020; Yim and Mizushima, 2020). Using
499 GFP-LC3 mice, we demonstrated that neonatal ileal samples exhibit increased autophagosome
500 degradation compared to post-weaning counterparts (**Figures 1A–1C and S1C**). Consistently, *Atg16*cKO
501 neonates displayed impaired absorption (**Figures 1H–1J**) and showed reduced expression of crucial
502 endocytic genes characteristic of LREs (**Figures 2B–2F, S2G and S2H**). Moreover, *Atg16*cKO neonatal

503 enterocytes displayed reduced lysosomal size and content (**Figures 2G–2J**), along with downregulation of
504 key lysosomal genes (**Figures S2G and S2H**). These outcomes reveal a functional interplay between
505 autophagy and the endolysosomal system in LREs.

506 Despite these endolysosomal defects, *Atg16*cKO mice reached the post-weaning stage without apparent
507 physiological abnormalities, aside from mild signs of intestinal inflammation (**Figures S2A–S2D**). This
508 observation aligns with findings in mice lacking the lysosomal cation channels Mucolipin-1 and -3 (Mcoln1
509 and Mcoln3), which also exhibit pronounced endolysosomal abnormalities in neonatal enterocytes but
510 develop into phenotypically normal adults (Remis et al., 2014). Together, these results suggest that
511 endolysosomal and autophagic processes primarily affect LREs. Accordingly, once the neonatal period
512 concludes and LREs are replaced by PECs, the phenotype becomes attenuated or fully resolves. However,
513 further investigations will be needed to assess intestinal physiology and metabolism in adult *Atg16*cKO
514 mice comprehensively.

515 We characterized a significant increase in autophagic activity in LREs as primarily due to the lysosomal
516 degradation of mitochondria, a process known as mitophagy. Indeed, mitophagy-related genes exhibit a
517 higher expression in neonatal ileum compared to post-weaning samples (**Figures 3B–3F**). Correspondingly,
518 neonatal *mito*-QC mice (McWilliams et al., 2016) demonstrated enhanced mitochondrial degradation within
519 the LVs of LREs compared to PECs (**Figures 3H and 3I**). Furthermore, this process was inhibited either by
520 leupeptin treatment (Jiménez-Loygorri et al., 2024) (**Figures 3H and 3I**) or through genetic ablation of
521 autophagy (*Atg16*cKO) (**Figures 3L and 3M**), confirming the dependence of mitochondrial clearance on
522 lysosomal-autophagic activity. Consistent with this, neonatal *Atg16*cKO enterocytes accumulated
523 dysfunctional mitochondrial mass (**Figure 4**). Specifically, these cells showed an increase in the area of
524 damaged mitochondria (class III), whereas healthy mitochondria (class I) exhibited a smaller area but an
525 increased aspect ratio (**Figures 4A–4C**). These differences possibly reflect not only mitophagy blockade
526 but also alterations in mitochondrial dynamics, such as enhanced fusion or reduced fission, which are aimed
527 at preserving oxidative phosphorylation (OXPHOS) capacity (Zemirli et al., 2018). Future studies should
528 investigate the expression of proteins involved in mitochondrial fusion and fission in the *Atg16*cKO model
529 to define better the molecular landscape that integrates mitochondrial dynamics with mitophagy in LREs.

530 After identifying mitochondrial homeostasis defects secondary to impaired endolysosomal function in the
531 *Atg16*cKO model, we next investigated the reverse relationship by directly disrupting mitochondrial function
532 using the *Tfam*cKO model. *Tfam*cKO neonates exhibited severe growth impairment and premature death
533 (**Figures 6A–6C**), and their enterocytes accumulated markedly damaged mitochondria (**Figures 6E–6G and**
534 **S6P**). These mice also reproduced key features of the *Atg16*cKO phenotype, including loss of uptake
535 capacity, reduced lysosomal content, and downregulation of endolysosomal genes (**Figures 6M-6O and**
536 **S7B–S7G**). Interestingly, these lysosomal defects differ from what has been observed in *Tfam*-deficient T
537 and B lymphocytes, where dysfunctional acidic lysosomal compartments are expanded (Baixauli et al.,
538 2015; Iborra-Pernichi et al., 2024). In neonatal enterocytes, however, Tfam deletion results in diminished

539 lysosomal size and content, highlighting that mitochondria–lysosome interactions are highly cell-type
540 specific. Beyond this bidirectional crosstalk, our data raise the possibility of a retrograde signalling
541 mechanism. Mitochondria are increasingly recognized as signalling hubs that influence nuclear
542 transcriptional programs, as shown in immune cells. In LREs, two interconnected processes may be at play:
543 first, endolysosomal-mediated nutrient internalization, which is defective in both *Atg16*cKO and *Tfam*cKO
544 models; and second, mitophagy-driven mitochondrial degradation, which provides retrograde signals to the
545 nucleus. This latter pathway could be essential for controlling the transcriptional networks that govern the
546 metabolic switch (via BLIMP1 and MAFB) and for sustaining lysosomal functionality itself. In this view,
547 lysosomes must degrade mitochondria not only to preserve organelle quality control but also to control the
548 transcriptional reprogramming required for the neonatal-to-adult metabolic transition.

549 At weaning, the mammalian intestine undergoes a shift to extracellular nutrient digestion and adjusts its
550 enzymatic profile to meet the metabolic demands of a carbohydrate-rich solid diet (Henning, 1981). At the
551 same time, LREs are replaced by PECs lacking large lysosomal vacuoles (Skrzypek et al., 2007). The
552 transcription factors BLIMP1 (PRDM1), along with MAFB and c-MAF (both members of the Maf protein
553 family) have been positioned as central repressors of this switch. Neonatal mice lacking these transcription
554 factors in the intestinal epithelium exhibited impaired nutrient absorption, premature downregulation of
555 neonatal enzymes, and upregulation of adult counterparts, ultimately leading to developmental defects
556 (Bara et al., 2022; Harper et al., 2011; Muncan et al., 2011). Furthermore, our research demonstrated that
557 dysfunctions in autophagic, lysosomal, and mitochondrial processes in LREs —induced by the deletion of
558 *Atg16l1* and *Tfam*— led to a repression of these transcription factors, resulting in similar phenotypes
559 (**Figures 1H, 5, 6H–6N and S7A**).

560 We further analysed the activity of core metabolic pathways in WT, *Atg16*cKO, and *Tfam*cKO neonatal
561 enterocytes, comparing them to PECs (**Figures 5H, 6L, and S5E**). This analysis revealed a moderate
562 reduction in metabolic activity in *Atg16*cKO cells and a more noticeable decline in *Tfam*cKO enterocytes,
563 suggesting a shift toward an adult-like metabolic state. These findings contrast with previous transcriptomic
564 data from neonatal mice lacking MAFB and c-MAF, which reported an upregulation of OXPHOS and fatty
565 acid degradation pathways (Bara et al., 2022). However, that study did not include a direct comparison to
566 PECs, leaving open the possibility of compensatory mechanisms. In this context, our results may provide
567 a more accurate reflection of the metabolic trajectory during neonatal-to-adult transition and its dependence
568 on the mitochondria-lysosome axis.

569 We have defined the metabolic evolution of enterocytes during neonatal development beyond the genes
570 classically associated with the transcription factors BLIMP1, MAFB, and c-MAF, and established a
571 functional link between this transition and the maintenance of lysosomal and mitochondrial homeostasis.
572 At the same time, our data reinforce the idea that, in enterocytes, genetic programs prevail over the sensing
573 of external cues: despite the neonatal context (milk-based diet, reduced microbiota, and limited immune

activation) (Walker, 2013), the repression of these transcription factors leads to inevitable epithelial maturation. Yet, the cellular mechanisms that regulate these genetic pathways still need to be clarified.

Reactive oxygen species (ROS) are oxygen-derived molecules that play a crucial role in various cellular processes, including energy production, mitochondrial signalling, and cell differentiation (Sena and Chandel, 2012; Sies et al., 2017). Their intracellular levels are tightly regulated through multiple mechanisms: the mitochondrial electron transport chain constitutes a major source of ROS, while antioxidant enzymes serve as key systems for neutralizing their excess (Murphy, 2008; Sena and Chandel, 2012; Sies et al., 2017). In the intestine, ROS have been primarily associated with more differentiated epithelial cells exhibiting higher OXPHOS activity (Rath et al., 2018). However, their role in epithelial maturation during neonatal intestinal development continues to be unexplored.

Our results indicate that LREs display a transcriptional signature consistent with elevated antioxidant activity, possibly as a compensatory mechanism to counteract high levels of mitochondrial ROS resulting from hyperactivated OXPHOS (**Figures 7A–7D**). Beyond this homeostatic role, recent studies suggest that this antioxidant signature may also be linked to the repression of transcription factor genes *Blimp1*, *Mafb*, and *c-maf*, and consequently, to the maintenance of LRE identity and function. The antioxidant vitamin ascorbic acid has been shown to increase the expression of Blimp1 in B lymphocytes through the activity of DNA demethylases TET2 and TET3 (Qi et al., 2020). Conversely, treatment with H_2O_2 decreases the expression of *c-maf*, whereas the ROS scavenger N-acetyl cysteine (NAC) can restore *its* levels in human adipose tissue-derived mesenchymal stem cells (Chen et al., 2015).

This hypothesis is further supported by the elevated ROS levels and the loss of the antioxidant signature observed in our knockout models (**Figures 4D, 6G, 7E–7J**), as well as by our experiments in which H_2O_2 treatment of neonatal WT mice accelerated the metabolic transition of enterocytes (**Figures 7K–7N**). Together, these outcomes suggest that both ROS levels and ROS-regulated genetic programs actively shape epithelial differentiation and metabolic programming in the neonatal intestine (**Figure 7O**). This may represent a physiological mechanism to prevent premature transitions until the tissue is developmentally prepared. In this context, therapeutic strategies aimed at fine-tuning redox homeostasis could offer a powerful approach to supporting neonatal intestinal health.

In addition to their role in nutrient absorption, LREs may act as immunometabolic sentinels during the neonatal period, integrating microbial cues and intracellular metabolic status to modulate immune responses. Due to their high endolysosomal activity, LREs could internalise and process luminal antigens, including microbial components, thereby contributing to the development of the intestinal immune system (Massaquoi and Guillemin, 2019). In line with this, our RNA-Seq analysis revealed multiple differentially regulated immune-related pathways (data not shown).

Disruption of lysosomal and mitochondrial homeostasis in *Atg16*cKO and *Tfam*cKO mice likely impairs these immune functions, as suggested by the inflammatory status observed in both models (**Figures S2D–S2F, S6E, and S6H–S6K**). In fact, mice with autophagy defects also exhibit gut microbiota alterations and

610 immune dysregulation (Larabi et al., 2020). Furthermore, cytosolic mtDNA resulting from mitochondrial
611 damage due to TFAM deficiency has been shown to activate the cGAS–STING inflammatory pathway
612 (Chung et al., 2019), while mitophagy induction, along with improved mitochondrial status, attenuates this
613 response (Jiménez-Loygorri et al., 2024). Additionally, *c-maf* KO mice exhibit changes in intraepithelial
614 lymphocytes and microbiota composition (Cosovanu et al., 2022), suggesting that genetic programs
615 involved in epithelial maturation, affected in our KO models, may be tightly linked to intestinal immune and
616 microbial homeostasis.

617 Given the immunometabolic imbalance observed in *Atg16*cKO and *Tfam*cKO neonates, it is plausible that
618 these models experience alterations in their gut microbiota. These changes may not only reflect enterocytic
619 dysfunction but could also actively contribute to the phenotype by disrupting microbial-derived cues
620 essential for LRE maintenance and programming. Future studies involving microbiota profiling and
621 transplantation will help determine whether restoring a balanced microbial ecosystem can rescue LRE
622 function.

623 Finally, the potential microbiota alterations described above, together with the inflammation and oxidative
624 stress observed in our KO models, suggest parallels with known hallmarks of children's malnutrition
625 disorders. Particularly, *Tfam*cKO mice display a more pronounced phenotype and marked developmental
626 defects, resembling features of Kwashiorkor, a severe form of protein deficiency prevalent in low-income
627 settings (Bhutta et al., 2017; Trehan and Manary, 2015). Notably, the redox imbalance observed in our
628 models resembles clinical features reported in malnourished children, who typically exhibit reduced levels
629 of antioxidants (Bhutta et al., 2017). Accordingly, pilot studies have demonstrated that antioxidant
630 supplementation may provide therapeutic benefit in conditions such as Kwashiorkor (Becker et al., 2005).
631 Moreover, our H_2O_2 treatment experiments, which replicated the epithelial maturation phenotype
632 characterized in our gene-deficient mice, might similarly induce nutritional, microbial, and inflammatory
633 disturbances. Indeed, intestinal tissues from H_2O_2-treated neonates displayed signs of inflammation (data
634 not shown).

635 Collectively, these considerations suggest that malnourished children may also experience premature
636 intestinal maturation and highlight the need for deeper investigation into antioxidant therapies as potential
637 interventions. Furthermore, our KO models may serve as valuable experimental platforms to investigate
638 the mechanisms underlying neonatal malnutrition and to explore interesting avenues for its treatment.
639 Altogether, future studies aimed at restoring LRE mitophagy and metabolism, as well as modulating the
640 redox balance, could yield promising strategies to counteract the devastating consequences of malnutrition-
641 related disorders in early life.

642 In conclusion, our study uncovers novel mechanisms underlying the function and metabolic transition of
643 neonatal enterocytes. We demonstrate that lysosomal and mitochondrial homeostasis is indispensable for
644 efficient nutrient absorption and for sustaining the high metabolic activity required during this energy-
645 demanding stage of life. Further investigation of the mitochondria-lysosome axis in LREs will not only

advance our understanding of neonatal intestinal physiology but also contribute significantly to the development of targeted interventions against childhood malnutrition.

Limitations of the study

This work demonstrates that neonatal intestinal deficits in autophagy and mitochondrial homeostasis lead to endolysosomal dysfunction in enterocytes, impairing development and ultimately triggering inflammation and early lethality. However, since we used *Villin-cre*-based models, where gene deletion occurs in all intestinal epithelial cells, we cannot exclude their contribution to the observed phenotypes. Indeed, we detected altered abundance and morphology of these cells in both *Atg16*cKO (**Figures 1F, 1G, and S2E–S2F**) and *Tfam*cKO mice (**Figures S6G, S6L–S6O**). Previous studies support this interpretation: defects in GCs and PCs are linked to intestinal inflammatory diseases (Hodzic et al., 2017; Wallaeys et al., 2023), and intestinal autophagy loss has been associated with increased oxidative stress in ISCs (Asano et al., 2017), which could partially explain the elevated ROS levels in *Atg16*cKO enterocytes (**Figure 4D**). Similarly, *Tfam* deletion in the adult intestinal epithelium causes ISC loss and lethality (Srivillibhuthur et al., 2018), suggesting that depletion of ISCs may contribute to the early death of neonatal *Tfam*cKO mice, limiting our ability to study mitochondrial function in enterocytes at later developmental stages.

To address these limitations, we plan to develop an LRE-specific tamoxifen-induced conditional knockout (cKO) model to target critical genes specifically in neonatal enterocytes. Although selectively targeting neonatal enterocytes would yield a more precise model, this is hindered by the lack of fully specific promoters and the technical difficulty of isolating and culturing LREs, which are highly sensitive to dissociation-induced cell death. To overcome these challenges, we are also studying *in vitro* systems that recapitulate the properties of LREs and may serve as a platform for future functional validation.

RESOURCE AVAILABILITY

Lead contact

Further information and requests for resources and reagents should be directed to and will be fulfilled by the lead contact, Fernando Martin-Belmonte (fmartin@cbm.csic.es).

Materials availability

This study did not generate new unique reagents.

Data and code availability

RNA-seq Illumina paired-end reads (FASTQ) generated for this study are available at the European Nucleotide Archive (ENA; http://www.ebi.ac.uk/ena/) under the study accession number PRJEB46511.

ACKNOWLEDGMENTS

680 We thank Carmen M. Ruiz-Jarabo for her comments on the manuscript and members of the Martin-
681 Belmonte and Martinez-Martin labs for their support and helpful discussions. This work was supported by
682 MICINN (BFU2017-83243-P; PID2020-120367GB-I00; PID2023-151844OB-I00; RED2022-134927-T),
683 Fondos FEDER investigación (Horizon-MSCA-2022-DN-101119504**)** and Fundación Ramon Areces
684 (CIVP18A3904). HR22-00447 from ¨La Caixa¨, RTI2018-101586-A-I00, PID2021-126298OB-100 to N.M.-
685 M. G.H. and M.I.-P. were supported by FPI fellowships BES-2018-077789 and PRE2019-089076,
686 respectively, funded by the Spanish Ministry of Science and Innovation and the State Research Agency
687 (MCIN/AEI /10.13039/501100011033). D.A.L was supported by FPU and JAE fellowships FPU23/03569
688 and JAEINT_22_01549. L.A was supported by Horizon-MSCA-2022-DN -101119504. I.G.G. was funded
689 by the Medical Research Council, UK (MC_UU_00038/2). We thank Victor Lazaro Morato (currently at IMN-
690 CNM, CSIC, Madrid, Spain) for his contribution to the initial analyses of the general phenotype and
691 mitochondrial status by TEM in the *Tfam*cKO model. We acknowledge Michel Bagnat (Duke University,
692 USA) for the generous donation of mCherry plasmid, and Juan M. Serrador, Catalina Grabowski and
693 Dionisio Ureña (CBM), for their essential contribution to the protocol for the growth and purification of
694 mCherry plasmid. We are thankful to the Animal, Flow Cytometry, Advanced Optical Microscopy, and
695 Electron microscopy facilities at the CBM, as well as the Histology Service at the Centro Nacional de
696 Biotecnologia (CNB, CSIC, Madrid, Spain), for their excellent technical support. We acknowledge the
697 Centro de Análisis Genómico (CNAG-CRG, Barcelona, Spain) for the RNA sequencing, and to
698 Biocomputational Analysis Core Facility at the CBM, specially to Sandra González de la Fuente, for the
699 NGS data analysis and plotting. We thank the computational resources and support provided by the Centro
700 de Computación Científica at Universidad Autónoma de Madrid (CCC-UAM).

701 Certain Figures were inspired by or adapted from previously published sources, some of which are licensed
702 under Creative Commons (CC BY 4.0) (https://creativecommons.org/licenses/by/4.0/). While every effort
703 has been made to credit original sources, any omissions are unintentional and will be corrected in future
704 revisions if identified. Some figures were created with BioRender.com.

705

706 **DECLARATION OF INTERESTS**

707 The authors declare no competing interests.

708

709 **FIGURE TITLES AND LEGENDS**

710 **Figure 1. High Autophagic Activity of LREs Is Required for Nutrient Absorption**

711 **(A and B)** Assessment of autophagic flux and protein absorption along the small intestine of GFP-LC3 mice
712 during postnatal development. GFP-LC3 mice at postnatal days (P) 1, 7, 14, and 21 were orally gavaged
713 with mCherry and sacrificed 3 hours later (n = 3) (A). Proximal and distal intestinal segments were harvested
714 (A), and epithelial cell lysates analysed by immunoblotting for mCherry and GFP-LC3 isoforms (B). The

representative western blot in (B) distinguishes cytosolic LC3-I, membrane-bound LC3-II, and cleaved “free GFP,” a marker of autolysosomal degradation. The pink rectangle highlights mCherry and free GFP in distal-P7, indicating maximal protein uptake and autophagic degradation. USP7, loading control. Figure 1A includes images adapted from Birchenough et al. (2023) (CC BY 4.0) and Zhao et al. (2021), and the GFP-LC3 isoforms scheme is based on Ni et al. (2011).

(C) Quantification of mCherry and free GFP levels in lysates of ileal epithelial cells from P7 (n = 4) and P21 (n = 5) GFP-LC3 mice. Data derived from Figure S1C.

(D and E) Generation and validation of *Atg16l1* intestinal knockout (*Atg16*cKO) mice. Ileal epithelial cell lysates from WT and *Atg16*cKO P14 mice were immunoblotted for ATG16L1, LC3, and P62 (D). (E) Quantification of ATG16L1 (n = 5,6) and P62 (n = 6,7), and LC3-II/LC3-I ratio (n = 17). In ATG16L1 and P62 graphs, data relative to WT.

(F and G) Ileal architecture in *Atg16*cKO neonates. Periodic acid-Schiff (PAS)-haematoxylin staining of P14 ileal sections from WT and *Atg16*cKO mice (F) shows villus shortening (double red arrow) and a decrease in goblet cells (PAS+, arrowheads) in *Atg16*cKO sections (n = 3). L, lumen; scale bar, 100 µm. (G) Quantification of villus length and goblet cells per villus. Dots represent individual villi (n = 30 villi from 3 mice; 10 villi per mouse).

(H) Confocal analysis of Rd-dextran uptake in ileal *Atg16*cKO enterocytes. WT and *Atg16*cKO neonates at P7 (early) and P14 (late), and post-weaning (P21–30) WT mice were gavaged with rhodamine B–dextran (Rd-dext, red) 16 hours prior to sacrifice (n = 3). Ileal sections labelled with β-catenin (βcat, white) and DAPI for DNA (blue). Dashed-line squares indicate magnified areas. Arrows point to lysosomal vacuoles; arrowheads, apical endosomes. L, lumen. Scale bars: 10 µm (main); 5 µm (insets). Dot plot shows the quantification of Rd-dextran intensity (integrated density) in the apical and basal regions of enterocytes. Dots represent individual enterocytes (n = 25–40).

(I and J) *Atg16*cKO mice show impaired mCherry absorption. P14 mice were gavaged with mCherry and ileal epithelial cell lysates collected 16 hours later for immunoblotting (I). Actin, loading control. (J) Quantification of mCherry signal, normalised to WT (n = 9,11).

In (C, E, J), dots represent individual mice and charts depict mean + SEM. In (G, H), dot plots show mean ± SEM (black lines).

(C, E, G): Student’s t-test (mCherry, ATG16L1, P62, villus length) and Mann–Whitney test (free GFP, LC3 ratio, goblet cells/villus). (J): Mann–Whitney test. (H): Kruskal–Wallis test; only statistically significant comparisons between WT and *Atg16*cKO are shown within each region (apical or basal). *$p < 0.05$; ****$p < 0.0001$.

See also Figure S1.

749 **Figure 2. Loss of Autophagy Compromises the Endolysosomal System in LREs**

750 **(A)** Reverse transcription quantitative polymerase chain reaction (RT-qPCR) analysis of *Dab2*, *Mcoln3*,
751 *Lamp2* and *Ctsl1* genes in epithelial cells from proximal and distal samples of small intestines from WT
752 mice at the indicated time points (n = 3). Data relative to values of proximal region of small gut from
753 embryonic day (E) 18.5 mice embryos, and presented as $\log_{10}$ fold changes ($\log_{10}$FC).

754 **(B)** RT-qPCR of *Dab2*, *Mcoln3*, and *Lamp2* in ileal epithelial cells from WT and *Atg16*cKO mice at P7 and
755 P14. Sample sizes: *Dab2* and *Lamp2* (n = 10,6,6,6), *Mcoln3* (n = 9,8,6,6).

756 **(C and D)** Immunoblot analysis of Dab2 protein in ileal epithelial cell lysates from WT and *Atg16*cKO mice
757 at P7 and P14 (C). Actin, loading control. (D) Quantification of Dab2 protein levels (n = 6,8,9,14).

758 **(E and F)** Confocal images of ileal sections from WT and *Atg16*cKO mice at P7 and P14 (n = 3) labelled
759 with anti-Dab2 (green), β-catenin (magenta), and DAPI (blue) (E). Arrowheads mark apical Dab2
760 localization. (F) Violin plot quantifying apical Dab2 intensity (integrated density) of P14 sections, normalised
761 to epithelial area (n = 10,8; 2–4 images per mouse).

762 **(G and H)** Lysosomal occupation and content in WT and *Atg16*cKO mice at P7 and P14, and in post-
763 weaning (P21–30) WT mice. Confocal sections labelled with anti-LAMP1 (green), β-catenin (white), and
764 DAPI (blue) (G). Arrows: endolysosomal system in WT LREs; arrowheads: reduced $LAMP1^+$ vesicles in
765 *Atg16*cKO and post-weaning enterocytes. (H) Dot plots quantify the percentage of $LAMP1^+$ area and
766 LAMP1 intensity (integrated density) within apical and basal regions of interest (ROIs) (n = 26–36).

767 **(I and J)** Immunoblot analysis of LAMP1 protein in ileal epithelial cell lysates from WT and *Atg16*cKO mice
768 at P14 (I). Actin, loading control. (J) Quantification of LAMP1 protein levels (n = 10,13).

769 In (E, F), dashed-line squares indicate magnified areas; L, lumen. Scale bars: 10 μm (main); 5 μm (insets).

770 Dots represent individual mice (B, D, J) or images (F) or cells (H). In (B, D, F, J), data relative to WT values.
771 Graphs of (A) represent mean + SD; graphs of (B, D, J), mean + SEM; violin plot of (F), median (thick line)
772 and interquartile range (IQR, thin lines); dot plots of (H), mean ± SEM (black lines).

773 Statistical analyses: Kruskal–Wallis test (A [*Dab2*, *Mcoln3*], H), two-way ANOVA (A: *Lamp2*, *Ctsl1*),
774 Student's *t*-test (B, D, J), Mann–Whitney test (F). In (A), only the most relevant statistically significant
775 comparisons are shown. In (H), only statistically significant comparisons are displayed within each group
776 (apical or basal). *$p < 0.05$, **$p < 0.01$, ***$p < 0.001$, ****$p < 0.0001$.

777 **See also Figure S2.**

778

779 **Figure 3. LREs Present High Levels of Mitophagy**

780 **(A)** Workflow of RNA sequencing (RNA-seq) analysis comparing LREs from P7 GFP-LC3 mice gavaged
781 with rhodamine B–dextran (16 hours prior) to PECs from post-weaning (P42) GFP-LC3 mice. Enterocytes

782 were isolated from ileal samples by fluorescence-activated cell sorting (FACS) and used for RNA-seq. See
783 Figure S4A for gating strategy. Scheme includes images adapted from Treuting et al. (2018) and Park et
784 al. (2019).

785 **(B)** Volcano plot of differentially expressed genes (DEGs) between LREs and PECs. Each point represents
786 a gene, plotted by $\log_2$ fold change (x-axis) and $-\log_{10}$ adjusted p-value (padj) (y-axis). DEGs (n = 1537;
787 shown in steel blue) were defined as genes with padj < 0.05 and $|\log_2 FC| > 1$. Upregulated genes associated
788 with endocytosis (amber), lysosome (purple), and mitophagy (red) are highlighted. Dashed lines indicate
789 significance (padj < 0.05) and fold-change thresholds (±1). Genes with $-\log_{10}(\text{padj}) > 60$ are not shown.

790 **(C)** Bubble plot of selected Gene Ontology (GO) terms from over-representation analysis (ORA) of the
791 differential gene expression data from the LREs vs PECs. Note the presence of regulation of autophagy,
792 positive regulation of autophagy of mitochondrion and mitochondrial outer membrane pathways. The x-axis
793 represents the z-score, bubble size reflects the number of associated genes, and bubble colour indicates
794 statistical significance (adjusted p-value), with a red-to-blue gradient from most to least significant. GO
795 terms are grouped into three categories: BP, biological process; CC, cellular component; MF, molecular
796 function.

797 **(D)** Enrichment plots of lysosome organization and mitochondrial outer membrane gene sets from gene set
798 enrichment analysis (GSEA) comparing LREs and PECs**.** The top panel shows the Enrichment Score (ES)
799 across ranked genes, with the peak indicating maximum enrichment. The middle panel marks gene
800 positions in the ranked list. The bottom colour bar reflects gene correlation with phenotype (red: positive,
801 blue: negative).

802 **(E)** RT-qPCR analysis of *Bnip3*, *Prkn*, and *Pink1* genes in ileal epithelial cells from WT mice at indicated
803 time points (n = 3). Values are expressed as $\log_{10}$ fold change relative to E18.5 embryonic levels.

804 **(F)** Confocal images of ileal sections from WT mice at P7 (LREs) and P21–30 (PECs), labelled with anti-
805 Parkin (green) and DAPI (blue). Left: violin plot of Parkin intensity (integrated density) normalised to
806 epithelial area.

807 **(G)** Schematic of the *mito*-QC reporter mouse model. Mitochondria are tagged with the chimeric protein
808 mCherry-GFP-FIS1$^{101–152}$. Upon mitophagy, mitochondria are delivered to the lysosome where acidic pH
809 quenches GFP but not mCherry, allowing identification of mitolysosomes as mCherry-only puncta.

810 **(H)** Confocal images of ileal sections from *mito*-QC mice at P7 (LREs) (± leupeptin, LP) and P21–30 (PECs).
811 Samples stained with anti-LAMP1 (white) and DAPI (blue). Arrows indicate enlarged, blocked lysosomes
812 with red-only mitochondrial aggregates in LREs+LP; arrowheads point to LAMP1$^+$/mCherry$^+$ puncta lacking
813 GFP, validating the *mito*-QC model.

814 **(I)** Violin plot of lysosomal mCherry intensity normalised to cellular mCherry intensity from (H), based on
815 integrated density measurements.

816 **(J)** RT-qPCR of *Bnip3* and *Prkn* in ileal epithelial cells from WT and *Atg16*cKO mice at P14. Dots represent
817 individual mice. Sample sizes: *Bnip3* (n = 6, 6), *Prkn* (n = 5, 6).

818 **(K)** Confocal images of ileal sections from WT and *Atg16*cKO mice at P14 stained with anti-Parkin (green)
819 and DAPI. Left: violin plot of Parkin intensity (Integrated Density) normalised to epithelial area.

820 **(L)** Confocal images of ileal sections from *mQ*-WT and *mQ-Atg16*cKO mice at P14 (n = 3), labelled with
821 anti-LAMP1 (white) and DAPI (blue).

822 **(M)** Violin plot of lysosomal mCherry intensity normalised to cellular mCherry intensity from (L), based on
823 integrated density measurements (n = 12–11; 3–4 images per mouse).

824 In images of (F, H, K, L), L, lumen. Scale bars: 5 µm. Images of (H, L) deconvolved with Huygens software.

825 In (A–I) and (K–M), n = 3; in (F, I, K), n = 9 images from 3 mice (3 images per mouse). In graphs of (F, I),
826 data relative to LREs values; in (J, K, M), relative to WT values. In (E), graph represents mean + SD; in (J),
827 mean + SEM. In violin plots of (F, I, K, M), the median (thick line) and IQR (thin lines) are shown and dots
828 represent individual images.

829 Statistical analyses: Kruskal–Wallis test (E: *Bnip3*), one-way ANOVA (E [*Prkn*, *Pink1*], I), Student's *t*-test
830 (F, J, K, M). *p< 0.05, **p< 0.01, ***p < 0.001.

831 **See also Figure S4.**

832

833 **Figure 4. *Atg16*cKO Neonatal Mice Exhibit Increased Mitochondrial Damage and Oxidative Stress in**
834 **Enterocytes**

835 **(A)** Representative transmission electron microscopy (TEM) micrographs of ileal sections from WT and
836 *Atg16*cKO mice at P14 (n = 3). Note the reduction of the endolysosomal system and the absence of
837 lysosomal vacuole in the *Atg16*cKO enterocytes. Dashed boxes indicate magnified areas. N, nucleus; LV,
838 lysosomal vacuole; AEC, apical endosomal complex; L, lumen. Asterisks indicate damaged mitochondria.
839 Scale bars: 2 µm (main); 500 nm (insets).

840 **(B)** TEM-based classification of mitochondria into three categories based on electron density and cristae
841 integrity: Class I (normal), Class II (partially affected), and Class III (damaged). Classification based on
842 Moschandrea et al. (2023). See Electron Microscopy Section in Methods. Scale bar: 500 nm.

843 **(C)** Distribution of mitochondrial integrity classes in *Atg16*cKO neonatal enterocytes. Quantification of the
844 number, percentage, area and aspect ratio (long axis / short axis) of each mitochondria class in (A), as
845 defined in (B). In count and percentage graphs, dots represent individual enterocytes; in area and aspect
846 ratio graphs, dots represent individual mitochondria. Sample sizes are indicated in Table S1.

847 **(D)** Flow cytometry analysis of mitochondrial status of *Atg16*cKO neonatal enterocytes. Graphs show
848 relative mean fluorescence intensity (MFI) for Mitotracker Green (mitochondrial mass, MM), Mitotracker

849 Red CMXROS (mitochondrial membrane potential, MMP) and CM-H_2DCFDA (ROS) in ileal EpCAM$^+$CD24$^-$
850 cKit$^-$ cells from WT and *Atg16*cKO mice at P14. See Figure S3 for gating strategy. Dots represent individual
851 mice (MM, n = 23,17; MMP, n = 10,9; ROS, n = 19,13).

852 In (C), dot plots represent mean ± SEM (black lines). In (D), bar chart show mean + SEM.

853 Statistics analyses: Mann–Whitney test (C, D [MM]), Student's *t*-test (D: MMP, ROS). *p < 0.05, **p < 0.01,
854 ***p < 0.001, ****p < 0.0001.

855 **See also Figure S3 and Table S1.**

856

857 **Figure 5. Autophagy Deficiency Causes Premature Metabolic Transition in LREs**

858 **(A)** RT-qPCR analysis of transcription factor (*Mafb*, *c-maf*, *Blimp1*), neonatal (*Ass1*, *Glb1*) and adult (*Treh*,
859 *Sis*, *Arg2*) enzyme genes in ileal epithelial cells from WT and *Atg16*cKO mice at late neonatal stage (P14)
860 and from WT mice at post-weaning stage (P21–30). Sample sizes: *Mafb* (n = 8, 9, 3), *c-maf* (n = 8, 11, 3),
861 *Blimp1* (n = 11, 9, 4), neonatal enzymes (n = 6, 5, 4), *Treh* (n = 5, 3, 4), *Sis* (n = 5, 5, 4), *Arg2* (n = 5, 6, 4).

862 **(B)** Confocal images of ileal sections from WT and *Atg16*cKO mice at P14 (n = 5), and from post-weaning
863 (P21–30) WT mice (n = 2–3), labelled with anti-MAFB (green, top) or anti-BLIMP1 (green, bottom), and with
864 phalloidin for F-actin (magenta) and DAPI (blue). Arrowheads point to nuclear localization of MAFB and
865 BLIMP1 in WT LREs.

866 **(C)** Violin plot of nuclear MAFB (n = 20, 21, 11) and BLIMP1 (n = 21, 16, 9) intensity (integrated density) in
867 (B), normalised to epithelial nuclear area.

868 **(D)** Confocal images of ileal sections from WT and *Atg16*cKO mice at P14, labelled with anti-ASS1 (green,
869 top) (n = 3) or anti-TREH (green, bottom) (n = 5), anti-E-cadherin (Ecad, magenta), and DAPI (blue).

870 **(E)** Violin plots of ASS1 (top; n = 12, 10) and TREH (bottom; n = 15,16) intensity (integrated density) in (D),
871 normalised to epithelial area.

872 **(F)** Western blot of TREH protein from ileal epithelial cells of WT and *Atg16*cKO mice at P14. USP7, loading
873 control.

874 **(G)** Bar chart quantifying TREH protein levels from (F) (n = 5, 4).

875 **(H)** Met-Flow profiling of ileal EpCAM$^+$CD24$^-$ cells from WT (n = 10–13) and *Atg16*cKO (n = 7–9) mice at
876 P14, and from post-weaning (P21–30) WT mice (n = 8). Bubble colour and size reflect group means for
877 each marker. See Figure S3 for the gating strategy and Table S2 for statistical significance.

878 In (B, D), dashed boxes indicate magnified areas; L, lumen. Scale bars: 10 μm (main); 5 μm (insets).

879 In (A, C, E, G, H), data relative to WT P14 values. In (A, G), graphs show mean + SEM and dots represent
880 individual mice. In (C, E), violin plots depict the median (thick line) and IQR (thin lines) and dots are
881 individual images (2–5 images per mouse, 2–5 mice per group).

882 Statistical analyses: one-way ANOVA (A, C [MAFB], H), Kruskal–Wallis test (C: BLIMP1), Mann–Whitney
883 test (E), Student's t test (G). *p < 0.05, **p < 0.01, ***p < 0.001, ****p < 0.0001.

884 **See also Figures S3 and S5, and Table S2.**

885

886 **Figure 6. *Tfam*cKO Neonates Recapitulate Endolysosomal and Metabolic Defects Observed in**
887 ***Atg16*cKO Enterocytes, and Exhibit Weight Loss and Early Lethality**

888 **(A)** Representative images of WT and *Tfam*cKO mice at postnatal day 14 (P14).

889 **(B)** Kaplan–Meier survival curves of WT and *Tfam*cKO mice. Animals were euthanized if they failed to gain
890 weight for two consecutive days or exhibited marked weight loss beginning at P9.

891 **(C)** Relative body weight of WT and *Tfam*cKO mice at P8, P10, P12, and P14, expressed as percentage.
892 Sample sizes are indicated at the bottom of the graph.

893 **(D)** RT-qPCR analysis of *Tfam* mRNA in ileal epithelial cells from WT and *Tfam*cKO mice at P10 and P14
894 (n = 12,12,12,10).

895 **(E)** *Tfam*cKO neonatal enterocytes show damaged mitochondria. TEM micrographs of ileal sections from
896 WT (n = 3) and *Tfam*cKO (n = 4) mice at P10 and P14. Asterisks indicate damaged mitochondria. Scale
897 bar, 1 μm.

898 **(F)** Quantification of mitochondrial classes in (E), as defined in Figure 4B. Dots represent individual
899 enterocytes. Sample sizes are indicated in Table S1.

900 **(G)** Flow cytometry analysis of mitochondrial status of *Tfam*cKO neonatal enterocytes. Bar charts show
901 relative MFI for Mitotracker Green (mitochondrial mass, MM), Mitotracker Red CMXROS (mitochondrial
902 membrane potential, MMP) and CM-H_2DCFDA (ROS) in ileal EpCAM$^+$CD24$^-$cKit$^-$ cells from WT and
903 *Tfam*cKO mice at P10 and P14. Sample sizes: MM (n = 5, 5, 8, 14), MMP (n = 3, 4, 10, 13), ROS (n = 9, 6,
904 10, 9). See Figure S3 for gating strategy.

905 **(H)** Confocal images of ileal sections from WT and *Tfam*cKO mice at P14 (n = 3–4), stained with anti-MAFB
906 (green, top) or anti-BLIMP1 (green, bottom), phalloidin (magenta), and DAPI (blue). Arrowheads mark
907 nuclear localization of MAFB and BLIMP1 in WT LREs.

908 **(I)** Violin plots quantifying nuclear MAFB (top; n = 15, 10) and BLIMP1 (bottom; n = 16, 16) intensity in (H),
909 normalised to epithelial nuclear area.

910 **(J)** Confocal images of ileal sections from WT and *Tfam*cKO mice at P14 (n = 3–4). Top: labelled with anti-
911 ASS1 (green), anti-E-cadherin (Ecad, magenta), and DAPI (blue). Bottom: labelled with anti-TREH (green)
912 and anti-Ecad (magenta).

913 **(K)** Violin plots quantifying ASS1 (top; n = 14, 16) and apical TREH (bottom; n = 9, 10) intensity in (J),
914 normalised to epithelial area.

915 **(L)** Met-Flow profiling of ileal $EpCAM^{+}CD24^{-}$ cells from WT (n = 6) and *Tfam*cKO (n = 5) mice at P14. Bubble
916 colour and size reflect group means for each marker. See Figure S3 for the gating strategy and Table S2
917 for statistical significance.

918 **(M)** Confocal images of ileal sections from WT (n = 4) and *Tfam*cKO (n = 3) mice at P14 gavaged with
919 rhodamine B–dextran (Rd-dext, red) 3 hours before sacrifice. Sections were stained with anti-LAMP1
920 (green), anti-β-catenin (white), and DAPI (blue). Arrow: endolysosomal system in WT LREs; arrowhead:
921 reduced $LAMP1^{+}$ vesicles in *Tfam*cKO enterocytes. Images deconvolved with Huygens software.

922 **(N)** Violin plot quantifying Rd-dextran uptake (integrated density) in (M), normalised to epithelial area (n =
923 11, 7).

924 **(O)** Quantification of lysosomal occupation and content in (M). Dot plots show the $LAMP1^{+}$ area as a
925 percentage of cell area (n = 167, 145) and LAMP1 intensity (integrated density) per enterocyte (n = 148,
926 139).

927 In (D–O), mice aged P9–11 and P13–15 were grouped as "P10" and "P14," respectively.

928 In (H, J, M), dashed boxes indicate magnified areas; L, lumen. Scale bars: 10 μm (main); 5 μm (insets).

929 In (C, D, G, I, K, L, N), data relative to WT values. In (C, D, G), graphs depict mean + SEM and dots
930 represent individual mice. In (F, O), dot plots show mean ± SEM (red lines) and dots represent individual
931 enterocytes. In (I, K, N), violin plots show median (thick line) and IQR (thin lines) and dots represent
932 individual images (2–4 per mouse).

933 Statistical analyses: Gehan–Breslow–Wilcoxon test (B), Student's *t*-test (C, D, F [P14 Class III only], G, K,
934 L, N), Mann–Whitney test (F [except P14 Class III], I, O). *$p < 0.05$, **$p < 0.01$, ***$p < 0.001$, ****$p < 0.0001$.

935 **See also Figures S3, S6 and S7, and Tables S1 and S2.**

936

937 **Figure 7. High Antioxidant Activity in LREs Regulates the Timing of Metabolic Transition**

938 **A)** Bar chart showing the relative mean fluorescence intensity (MFI) of MitoSOX (mitochondrial ROS) and
939 CM-H_2DCFDA (total ROS) in ileal $EpCAM^{+}CD24^{-}$ cells from WT mice at P7 (LREs) and P21–30 (PECs) (n
940 = 4). Data relative to LREs values. See Figure S3 for gating strategy.

941 **(B)** Bubble plot and list of ROS-related GO terms from over-representation analysis (ORA) of DEGs
942 between LREs and PECs. The x-axis represents the z-score, the y-axis shows the significance as –

943 log_{10}(adjusted p-value), bubble size reflects the number of associated genes, and colors indicate GO
944 categories (BP, biological process; CC, cellular component; MF, molecular function).

945 **(C)** GSEA enrichment plot of antioxidant activity gene set (LREs vs PECs).

946 **(D)** RT-qPCR analysis of *Gpx3* and *Cat* genes in ileal epithelial cells from WT mice at the indicated time
947 points (n = 3). Values are expressed as log_{10} fold change relative to E18.5 embryonic levels.

948 **(E)** RT-qPCR analysis of *Gpx3* and *Cat* genes in ileal epithelial cells from WT and *Atg16*cKO mice at P14
949 (n = 6).

950 **(F)** RT-qPCR analysis of *Gpx3* (n = 7, 5) and *Cat* (n = 5, 7) in ileal epithelial cells from WT and *Tfam*cKO
951 mice at P14.

952 **(G)** Confocal images of ileal sections from WT and *Atg16*cKO mice at P14 (n = 3), stained with anti-GPX3
953 (green), anti-E-cadherin (Ecad, magenta), and DAPI (blue).

954 **(H)** Violin plot of GPX3 intensity from (G), normalised to epithelial area (n = 12, 9).

955 **(I)** Confocal images of ileal sections from WT and *Tfam*cKO mice at P14 (n = 4), labelled as in (F).

956 **(J)** Violin plot of GPX3 intensity from (H), normalised to epithelial area (n = 16).

957 **(K)** RT-qPCR analysis of transcription factor (*Mafb*, *c-maf*, *Blimp1*), neonatal (*Ass1*, *Glb1*) and adult (*Treh*,
958 *Arg2*) enzyme genes in ileal epithelial cells from control and H_2O_2 treated mice at P12. Sample sizes: *Mafb*
959 (n = 7, 6), *c-maf* (n = 7, 6), *Blimp1* (n = 7, 7), neonatal enzymes (n = 7, 7), *Treh* (n = 5, 6), *Arg2* (n = 6, 6).

960 **(L)** Confocal images of ileal sections from control (n = 4) and H_2O_2-treated (n = 4–5) mice at P12, stained
961 with anti-BLIMP1 (green, left) or anti-ASS1 (green, centre) or anti-TREH (green, right), and DAPI (blue). L,
962 lumen. Scale bars, 10 µm.

963 **(M)** Violin plots of BLIMP1, ASS1 and TREH intensity (integrated density) from (L). BLIMP1 data were
964 normalised to epithelial nuclear area; ASS1 and TREH data, to epithelial area. Sample sizes: BLIMP1 (n =
965 12, 15), ASS1 (n = 12, 16), TREH (n = 13, 12).

966 **(N)** Flow cytometry analysis of BLIMP1 (n = 7, 7) and ASS1 (n = 6, 7) in control and H_2O_2-treated mice at
967 P12. Bar charts show relative median fluorescent intensity of BLIMP1 and ASS1 in ileal $EpCAM^+CD24^-cKit^-$
968 cells. See Figure S3 for gating strategy.

969 **(O)** Working model: In *Atg16*cKO and *Tfam*cKO neonatal enterocytes, mitochondrial dysfunction and
970 reduced antioxidant responses elevate ROS levels, which repress *Blimp1* and *Mafb* expression and drive
971 premature metabolic transition. Enterocyte's design inspired by Fujita et al. (1990). Figure created with
972 BioRender.com.

973 In (G, I), dashed boxes indicate magnified areas; L, lumen. Scale bars: 10 µm (main); 5 µm (insets).

974 In (E, F, H, J), data relative to WT values; in (K, M, N), relative to control values. In (A, E, F, K, N), graphs
975 represent mean + SEM and dots represent individual mice; in (C), mean + SD. In (H, J, M), violin plots show
976 median (thick line) and IQR (thin lines) and dots represent individual images (2–4 per mouse, 3–5 mice per
977 group).

978 Statistical analyses: Student's t test (A, E, F, H, K, M [ASS1], N), one-way ANOVA (D), Mann–Whitney test
979 (J, M [BLIMP1, TREH]). *p < 0.05, **p < 0.01, ***p < 0.001, ****p < 0.0001.

980 **See also Figure S3.**

981

982 **SUPPLEMENTAL INFORMATION**

983 **Figure S1. Characterization of LREs in the Neonatal Mouse Ileum**
984 ***Related to Figures 1 and 2***

985 (**A**) Representative TEM image of LREs from the distal small intestine of a P7 mice (n = 3). The profile of
986 an LRE is outlined by a dashed line. Dashed boxes indicate magnified areas. N, nucleus; LV, lysosomal
987 vacuole; AEC, apical endosomal complex; e, endosome; mvb, multivesicular body; L, lumen. Scale bars:
988 5 μm (main); 2 μm (insets).

989 (**B**) Confocal microscopy images of ileal sections from P7 mice (n = 3), stained with anti-LAMP1 (green),
990 anti-Dab2 (magenta), anti-β-catenin (white), and DAPI (cyan). Dashed boxes highlight magnified areas.
991 Arrows indicate the endolysosomal system; arrowheads point to apical Dab2 localization. Scale bars: 20 μm
992 (main); 10 μm (first magnification); 5 μm (second magnification).

993 (**C**) Western blot of mCherry and GFP-LC3 isoforms in ileal epithelial cells from GFP-LC3 mice at P7 and
994 P21, gavaged with mCherry 3 hours before sacrifice. USP7, loading control.

995 (**D**) Sequential fluorescent dextran uptake assay. P7 mice were gavaged with Alexa 647-dextran (FR-dext,
996 green), followed by rhodamine B–dextran (Rd-dext, red) 3 hours later. Mice were sacrificed at 4 and 8 hours
997 post-initial gavage to assess uptake via confocal microscopy (n = 3). Arrows point to lysosomal vacuoles
998 containing both dextrans at 8 hours. Arrowheads indicate endosomes. Scale bars: 5 μm (main); 2 μm
999 (insets).

1000

1001 **Figure S2. Phenotype of *Atg16*cKO Mice**
1002 ***Related to Figures 1 and 2***

1003 **(A)** Relative body weight of WT and *Atg16*cKO mice at postnatal days P7, P14, and P30. Sample sizes are
1004 indicated in the graph.

1005 **(B)** Representative images of intestines from WT and *Atg16*cKO mice at the post-weaning stage (P30).

1006 **(C)** Quantification of intestinal lengths shown in (B). Bar graphs show the relative lengths of the small
1007 intestine (SI) and the colon–rectum (CR) segments (n = 7, 9).

1008 **(D)** Representative histological images of ileum and colon sections from WT and *Atg16*cKO post-weaning
1009 (P30) mice (n = 3). Ileal sections are stained with periodic acid-Schiff (PAS) and haematoxylin; colon
1010 sections are stained with haematoxylin and eosin (H&E). Asterisks denote oedema in *Atg16*cKO ileum;
1011 arrowheads indicate goblet cells. Scale bars: 200 μm (ileum), 400 μm (colon).

1012 **(E and F)** Flow cytometry analysis of immune and epithelial cell populations in the ileum of WT and
1013 *Atg16*cKO mice at P14 (E) and P30 (F). Left: B lymphocytes (LB) and T-helper lymphocytes (LTh)
1014 percentages. Centre: Innate immune cells (IIC) and intestinal epithelial cells (IEC) percentages. Right:
1015 Enterocyte and enterocytic progenitors (EC), goblet cell (GC), Paneth cell (PC), and enteroendocrine cell
1016 (EEC) percentages. See Figure S3 for gating strategy. (E): Left, n = 17,8–11; Centre, n = 22,16–17; Right,
1017 n = 15,12–13. (F): n = 6–7, 9–10.

1018 **(G)** RT-qPCR analysis of *Dab2* (n = 10,6,6,5), *Mcoln3* (n = 9,8,6,5), and *Lamp2* (n = 10,6,6,6) in epithelial
1019 cells from the proximal small intestine of WT and *Atg16*cKO mice at P7 and P14.

1020 **(H)** RT-qPCR analysis of *Amn* (n = 6,5), *Mamdc4* (n = 9,10), and *Ctsl1* (n = 9,11) in ileal epithelial cells
1021 from WT and *Atg16*cKO mice at P14.

1022 In (A, C, G, H), graphs represent mean + SEM. In (E, F), violin plots depict median (thick line) and
1023 interquartile range (IQR, thin lines). In all graphs, data relative to WT values, dots represent individual mice
1024 and Student's t test was conducted. *$p < 0.05$, **$p < 0.01$, ***$p < 0.001$, ****$p < 0.0001$.

1025

1026 **Figure S3. Gating Strategies Used for Cell Population Characterization by Flow Cytometry**
1027 ***Related to Figures 4–7, S2 and S4–S6***

1028 Biopool is the combination of immune cell markers anti-CD11c, anti-CD3e, anti-CD11b, anti-CD19, and
1029 anti-CD45.2. The strategy for selecting IEC subtypes is based on Asano et al. (2017). GD, ghost dye; LT_h,
1030 T-helper lymphocytes; LB, B lymphocytes; IIC, innate immune cells; IEC, intestinal epithelial cells; EEC,
1031 enteroendocrine cells; PC, Paneth cells; EC, enterocytes and enterocytic progenitors; GC, goblet cells.

1032

1033 **Figure S4. RNA-seq Analysis Comparing Gene Expression of LREs and PECs**
1034 ***Related to Figure 3***

1035 **(A)** FACS gating strategy used to isolate LREs and PECs from GFP-LC3 mice at P7 (gavaged with Rd-
1036 dextran, 16 hours) and P42, respectively, for RNA-seq analysis. Single-living $EpCAM^{+}CD24^{-}Biopool^{-}$ cells
1037 were gated. For LREs, $Dextran^{+}GFP^{high}$ cells were selected.

1038 **(B)** Heatmap with hierarchical clustering of differentially expressed genes (DEGs) with q-value < 0.05
1039 reveals distinct expression patterns between LREs and PECs. Each row represents a single gene and each

1040 column represents a condition sample. Each sub-column represents an individual sample (3 samples per
1041 group). Gene expression intensities were log_2-transformed and visualized as a colour gradient from yellow
1042 to light blue, representing the shift from downregulation to upregulation, as indicated in the key.

1043 **(C)** Principal component analysis (PCA) plotting for 2 groups based on normalised overall transcriptomic
1044 reads. The PCA figure represents a two-dimensional scatterplot of the first two principal components of the
1045 RNA-Seq data. Analyses in panels (B) and (C) show that replicates of the same cell population are more
1046 similar to each other than to replicates from a different population.

1047 (**D**) Bubble plot of selected Kyoto Encyclopaedia of Genes and Genomes (KEGG) pathways from over-
1048 representation analysis (ORA) of the differential gene expression data from the LREs vs PECs. The x-axis
1049 represents the z-score, the y-axis shows the significance as –log10(adjusted p-value), bubble size reflects
1050 the number of associated genes, and colours indicate KEGG pathway categories.

1051 **(E)** RT-qPCR validation of *Ctsl1* expression in LREs and PECs from WT mice at P7 (gavaged with Rd-
1052 dextran, 16 hours) and P42, respectively. FACS was used for cell sorting, selecting single-living
1053 $EpCAM^+CD24^-Biopool^-$ cells, with $Dextran^+$ cells further gated for LREs. In LREs, each dot represents one
1054 of three pooled samples (n = 3), each composed of multiple mice; in PECs, each dot corresponds to an
1055 individual mouse (n = 3). Data relative to LREs values.

1056 **(F)** Analysis of lysosomal content in LREs and PECs by measuring Lysotracker MFI by flow cytometry. Bar
1057 chart depicts Lysotracker MFI of LREs and PECs from WT mice at P7 (gavaged with mCherry, 16 hours)
1058 and P42 respectively. Single-living $EpCAM^+CD24^-Biopool^-$ cells were gated. For LREs, $mCherry^+$ cells were
1059 selected. See Figure S3 for gating strategy. Dots represent individual mice (n = 3).

1060 Graphs in (E, F) represent mean + SEM. In (E), Student's t test; in (F), Mann–Whitney test. *$p < 0.05$, **p
1061 < 0.01.

1062

1063

1064 **Figure S5. Metabolic Transition in the Small Gut During Postnatal Development**
1065 ***Related to Figure 5***

1066 (**A)** Expression and statistical data of selected genes encoding transcription factors (TFs: *Mafb, c-maf,*
1067 *Blimp1*), neonatal enzymes (*Ass1, Glb1*), and adult enzymes (*Treh, Sis, Arg2*) from the LREs vs PECs
1068 RNA-seq analysis.

1069 **(B and C)** RT-qPCR analysis of *Mafb* and *Blimp1* (B), and of *Ass1, Glb1, Treh,* and *Sis* (C) genes in
1070 epithelial cells isolated from proximal and distal small intestinal segments of WT mice at the indicated
1071 postnatal time points (n = 3). Data are normalised to the expression levels in the proximal small intestine of
1072 E18.5 embryos and expressed as log_{10}fold change (log_{10}FC).

1073 **(D)** Schematic representation of the cellular metabolic pathways. Enzymes used in the Met-flow panel are
1074 shown in red. Scheme adapted from Iborra et al. (2024) (CC BY 4.0).

1075 **(E)** Met-Flow analysis of ileal EpCAM^{+}CD24^{-} cells from WT mice at P7 (LREs) and P42 (PECs) (n = 2–4).
1076 Data relative to LREs values. Bubble colour and size reflect group means for each marker. See Figure S3
1077 for the gating strategy and Table S2 for statistical significance.

1078 In (B, C), graphs represent mean + SD, two-way ANOVA was conducted and only the most relevant
1079 statistically significant comparisons are shown. In (E), Student's *t*-test. *p < 0.05, **p < 0.01, ***p < 0.001,
1080 ****p < 0.0001.

1081

1082 **Figure S6. Validation and Intestinal Phenotype of *Tfamc*KO Neonatal Mice**
1083 ***Related to Figure 6***

1084 **(A)** Relative mitochondrial DNA (mtDNA) levels of *Nd1*, *Co1*, *Co2*, and *Atp6* in ileal epithelial cells from WT
1085 and *Tfam*cKO mice at P10 (n = 2) and P14 (n = 4), measured by qPCR.

1086 **(B)** RT-qPCR analysis of mitochondrial genes *mt-Nd1*, *mt-Co2*, and *Sdha* in ileal epithelial cells from WT
1087 and *Tfam*cKO mice at P10 (n = 5–6).

1088 **(C)** Confocal images of ileal sections from WT (n = 3) and *Tfam*cKO (n = 2) mice at P14, labelled with anti-
1089 MTCO1 (green) and anti-β-catenin (magenta). Arrows point to mitochondria in WT LREs.

1090 **(D)** Violin plot shows MTCO1 intensity (integrated density) from (C), normalised to epithelial area. Dots
1091 represent individual images (n = 9,7; 3–4 images per mouse).

1092 **(E)** PAS and haematoxylin staining of ileal sections from WT and *Tfam*cKO mice at P10 and P14 (n = 4–6)
1093 shows inflamed and disorganized epithelium in *Tfam*cKO mice. Phenotypes include shortened villi (double
1094 red arrows), thickened submucosa and lower mucosa (double black arrows), oedema (asterisks), reduced
1095 PAS+ goblet cells (arrowheads), and abnormal vacuoles in enterocytes (arrows).
1096 Scale bars: 200 µm (main); 100 µm (insets).

1097 **(F–H)** Quantification of villi length (F), percentage of villi with goblet cells (G), and the maximum thickness
1098 of submucosa and lower mucosa (H) from (E). In (F), each dot represents a villus (n = 50,60,50,50; 10 villi
1099 per mouse). For (G–H), n = 4–6 mice.

1100 **(I–K)** Flow cytometry analysis of innate immune cells (IIC, I), B lymphocytes (LB, J), and T-helper cells (LT_h,
1101 K) percentages in the ileal of WT and *Tfam*cKO mice at P10 and P14 (n = 3–5). See Figure S3 for gating
1102 strategy.

1103 **(L–O)** Confocal imaging and quantification of stem and Paneth cells in WT and *Tfam*cKO ileal at P10 and
1104 P14:

1105 - (**L**) Olfm4 (green) labels crypt stem cells; arrows point to Olfm4^{+} crypts.

1106 • (**M**) Quantification of Olfm4^{+} crypts (30-100 crypts/mouse).

1107 • (**N**) Lysozyme (green) marks Paneth cells; arrows show normal crypt localization, arrowheads
1108 indicate mislocalised Paneth cells in villi.

1109 • (**O**) Quantification Paneth cells/mm² of epithelial area.

1110 For (L, N), sections are also stained with anti-Ecad (white) and DAPI (blue). Scale bars: 200 µm (main);
1111 50 µm (insets). For all panels, n = 3 mice.

1112 **(P)** Distribution of mitochondrial integrity classes in *Tfam*cKO neonatal enterocytes. Quantification of the
1113 percentage, area and aspect ratio (long axis / short axis) of each mitochondria class in Figure 6E, as defined
1114 in Figure 4B. In percentage graph, dots represent individual enterocytes; in area and aspect ratio graphs,
1115 dots are individual mitochondria. Sample sizes are indicated in Table S1.

1116 In (C, E, L, N), dashed boxes indicate magnified areas; L, lumen.

1117 In (A, B, D, I–K), data relative to WT values. In (A, G–K, M, O), graphs represent mean + SEM and dots
1118 represent individual mice. In (B, D), violin plots show the median (thick line) and IQR (thin lines). In (F, P),
1119 dot plots show mean ± SEM (red lines).

1120 Statistical analyses: Student's t test (A, B, I–K, M, O), Mann–Whitney test (D, P), two-way ANOVA (F, H),
1121 Kruskal–Wallis test (G). In (F–H), only statistically significant comparisons between WT and *Tfam*cKO are
1122 indicated within each time group. *p < 0.05, **p < 0.01, ***p < 0.001, ****p < 0.0001.

1123

1124 **Figure S7. *Tfam*cKO Neonatal Enterocytes Exhibit a Decreased Endolysosomal System and**
1125 **Undergo an Early Metabolic Switch**
1126 ***Related to Figure 6***

1127 **(A)** RT-qPCR analysis of transcription factor (*Mafb*, *c-maf*, *Blimp1*), neonatal (*Ass1*, *Glb1*) and adult (*Treh*,
1128 *Sis*, *Arg2*) enzyme genes in ileal epithelial cells from WT and *Tfam*cKO mice at P10 and P14.

1129 **(B)** RT-qPCR analysis of *Dab2*, *Amn*, and *Mamdc4* genes in ileal epithelial cells from WT and *Tfam*cKO
1130 mice at P10 and P14.

1131 **(C)** Confocal images of ileal sections from WT and *Tfam*cKO mice at P10 (n = 3) and P14 (n = 2–3), labelled
1132 with anti-Dab2 (green), anti-β-catenin (white), and DAPI (blue). Arrowheads indicate apical Dab2
1133 localisation.

1134 **(D)** Violin plot shows apical Dab2 intensity (integrated density) from (C), normalised to epithelial area and
1135 relative to WT values. Dots represent individual images (n = 6, 6, 6, 4; 2 images per mouse).

1136 **(E)** RT-qPCR analysis of *Lamp2*, *Mcoln3*, and *Ctsl1* in ileal epithelial cells from WT and *Tfam*cKO mice at
1137 P10 and P14.

1138 **(F)** Confocal images of ileal sections from WT and *Tfam*cKO mice at P10 (n = 3), labelled with anti-LAMP1
1139 (green), anti-β-catenin (white), and DAPI (blue). Arrows indicate endolysosomal system in WT cells;
1140 arrowheads highlight the reduced lysosomal vesicles in *Tfam*cKO enterocytes.

1141 **(G)** Quantification of lysosomal occupation and content in (E). Dot plots show the LAMP1$^+$ area as a
1142 percentage of cell area (n = 157,99) and LAMP1 intensity (integrated density) per enterocyte (n = 117,74).
1143 Dots represent individual enterocytes.

1144 In (C, F), dashed boxes indicate magnified areas; L, lumen. Scale bars: 10 μm (main); 5 μm (insets).

1145 In (A, B, E), data relative to WT-P10 values, dots represent individual mice (n = 4–7), and graphs represent
1146 mean + SEM. In (D), violin plot shows the median (thick line) and IQR (thin lines). In (G), dot plots depict
1147 mean ± SEM (red lines).

1148 Statistical analyses: Kruskal–Wallis test (A [*Treh*], B [*Dab2*], E [*Lamp2*]), two-way ANOVA (A, B, E; except
1149 *Treh*, *Dab2*, *Lamp2*), Student's t test (D), Mann–Whitney test (G). In (A, B, E), only statistically significant
1150 comparisons between WT and *Tfam*cKO are indicated within each time group. *p < 0.05, **p < 0.01, ***p <
1151 0.001, ****p < 0.0001.

1152

1153 **Table S1. Sample sizes in TEM graphs**

1154 ***Related to Figures 4, 6 and S6***

1155 Values in the number (No.) and percentage columns correspond to enterocytes; in the area and aspect
1156 ratio columns, values correspond to individual mitochondria. For more detailed information on sample size
1157 of the analyses, see the TEM section in the Methods.

1158

1159 **Table S2. Statistical Significance of Met-Flow Experiments**

1160 ***Related to Figures 5, 6 and S5***

1161 For Figure 5H, statistical results are shown only for comparisons between WT and the two other groups.
1162 No statistical test was applied for HK1 of Figure S5E (n = 2). *p < 0.05, **p < 0.01, ***p < 0.001, ****p <
1163 0.0001. NS, not significant.

1164

1165

1166 **REFERENCES**

1167 Ahl, P.J., Hopkins, R.A., Xiang, W.W., Au, B., Kaliaperumal, N., Fairhurst, A.-M., Connolly, J.E., 2020. Met-
1168 Flow, a strategy for single-cell metabolic analysis highlights dynamic changes in immune
1169 subpopulations. Commun. Biol. 3, 305. https://doi.org/10.1038/s42003-020-1027-9

1170 Asano, J., Sato, T., Ichinose, S., Kajita, M., Onai, N., Shimizu, S., Ohteki, T., 2017. Intrinsic Autophagy Is
1171 Required for the Maintenance of Intestinal Stem Cells and for Irradiation-Induced Intestinal
1172 Regeneration. Cell Rep. 20, 1050–1060. https://doi.org/10.1016/j.celrep.2017.07.019

1173 Baixauli, F., Acín-Pérez, R., Villarroya-Beltrí, C., Mazzeo, C., Nuñez-Andrade, N., Gabandé-Rodriguez, E.,
1174 Ledesma, M.D., Blázquez, A., Martin, M.A., Falcón-Pérez, J.M., Redondo, J.M., Enríquez, J.A.,
1175 Mittelbrunn, M., 2015. Mitochondrial Respiration Controls Lysosomal Function during Inflammatory
1176 T Cell Responses. Cell Metab. 22, 485–498. https://doi.org/10.1016/j.cmet.2015.07.020

1177 Bara, A.M., Chen, L., Ma, C., Underwood, J., Moreci, R.S., Sumigray, K., Sun, T., Diao, Y., Verzi, M.,
1178 Lechler, T., 2022. Maf family transcription factors are required for nutrient uptake in the mouse
1179 neonatal gut. Dev. Camb. Engl. 149, dev201251. https://doi.org/10.1242/dev.201251

1180 Becker, K., Pons-Kühnemann, J., Fechner, A., Funk, M., Gromer, S., Gross, H.-J., Grünert, A., Schirmer,
1181 R.H., 2005. Effects of antioxidants on glutathione levels and clinical recovery from the malnutrition
1182 syndrome kwashiorkor--a pilot study. Redox Rep. Commun. Free Radic. Res. 10, 215–226.
1183 https://doi.org/10.1179/135100005X70161

1184 Beumer, J., Clevers, H., 2021. Cell fate specification and differentiation in the adult mammalian intestine.
1185 Nat. Rev. Mol. Cell Biol. 22, 39–53. https://doi.org/10.1038/s41580-020-0278-0

1186 Bhutta, Z.A., Berkley, J.A., Bandsma, R.H.J., Kerac, M., Trehan, I., Briend, A., 2017. Severe childhood
1187 malnutrition. Nat. Rev. Dis. Primer 3, 17067. https://doi.org/10.1038/nrdp.2017.67

1188 Birchenough, G.M.H., Schroeder, B.O., Sharba, S., Arike, L., Recktenwald, C.V., Puértolas-Balint, F.,
1189 Subramani, M.V., Hansson, K.T., Yilmaz, B., Lindén, S.K., Bäckhed, F., Hansson, G.C., 2023.
1190 Muc2-dependent microbial colonization of the jejunal mucus layer is diet sensitive and confers local
1191 resistance to enteric pathogen infection. Cell Rep. 42, 112084.
1192 https://doi.org/10.1016/j.celrep.2023.112084

1193 Birgisdottir, Å.B., Johansen, T., 2020. Autophagy and endocytosis – interconnections and
1194 interdependencies. J. Cell Sci. 133, jcs228114. https://doi.org/10.1242/jcs.228114

1195 Boyle, E.I., Weng, S., Gollub, J., Jin, H., Botstein, D., Cherry, J.M., Sherlock, G., 2004. GO::TermFinder—
1196 open source software for accessing Gene Ontology information and finding significantly enriched
1197 Gene Ontology terms associated with a list of genes. Bioinformatics 20, 3710–3715.
1198 https://doi.org/10.1093/bioinformatics/bth456

1199 Cadwell, K., Liu, J.Y., Brown, S.L., Miyoshi, H., Loh, J., Lennerz, J.K., Kishi, C., Kc, W., Carrero, J.A., Hunt,
1200 S., Stone, C.D., Brunt, E.M., Xavier, R.J., Sleckman, B.P., Li, E., Mizushima, N., Stappenbeck,
1201 T.S., Virgin IV, H.W., 2008. A key role for autophagy and the autophagy gene Atg16l1 in mouse
1202 and human intestinal Paneth cells. Nature 456, 259–263. https://doi.org/10.1038/nature07416

1203 Campbell, C.T., Kolesar, J.E., Kaufman, B.A., 2012. Mitochondrial transcription factor A regulates
1204 mitochondrial transcription initiation, DNA packaging, and genome copy number. Biochim. Biophys.
1205 Acta 1819, 921–929. https://doi.org/10.1016/j.bbagrm.2012.03.002

1206 Chen, P.-M., Lin, C.-H., Li, N.-T., Wu, Y.-M., Lin, M.-T., Hung, S.-C., Yen, M.-L., 2015. c-Maf regulates
1207 pluripotency genes, proliferation/self-renewal, and lineage commitment in ROS-mediated
1208 senescence of human mesenchymal stem cells. Oncotarget 6, 35404–35418.
1209 https://doi.org/10.18632/oncotarget.6178

1210 Choo, J., Glisovic, N., Matic Vignjevic, D., 2022. Gut homeostasis at a glance. J. Cell Sci. 135.
1211 https://doi.org/10.1242/jcs.260248

1212 Chung, K.W., Dhillon, P., Huang, S., Sheng, X., Shrestha, R., Qiu, C., Kaufman, B.A., Park, J., Pei, L.,
1213 Baur, J., Palmer, M., Susztak, K., 2019. Mitochondrial Damage and Activation of the STING
1214 Pathway Lead to Renal Inflammation and Fibrosis. Cell Metab. 30, 784-799.e5.
1215 https://doi.org/10.1016/j.cmet.2019.08.003

1216 Cosovanu, C., Resch, P., Jordan, S., Lehmann, A., Ralser, M., Farztdinov, V., Spranger, J., Mülleder, M.,
1217 Brachs, S., Neumann, C., 2022. Intestinal epithelial c-Maf expression determines enterocyte
1218 differentiation and nutrient uptake in mice. J. Exp. Med. 219, e20220233.
1219 https://doi.org/10.1084/jem.20220233

1220 Cox, C.M., Lu, R., Salcin, K., Wilson, J.M., 2018. The Endosomal Protein Endotubin Is Required for
1221 Enterocyte Differentiation. Cell. Mol. Gastroenterol. Hepatol. 5, 145–156.
1222 https://doi.org/10.1016/j.jcmgh.2017.11.001

1223 el Marjou, F., Janssen, K.-P., Chang, B.H.-J., Li, M., Hindie, V., Chan, L., Louvard, D., Chambon, P.,
1224 Metzger, D., Robine, S., 2004. Tissue-specific and inducible Cre-mediated recombination in the
1225 gut epithelium. Genes. N. Y. N 2000 39, 186–193. https://doi.org/10.1002/gene.20042

1226 Foerster, E.G., Mukherjee, T., Cabral-Fernandes, L., Rocha, J.D.B., Girardin, S.E., Philpott, D.J., 2022.
1227 How autophagy controls the intestinal epithelial barrier. Autophagy 18, 86–103.
1228 https://doi.org/10.1080/15548627.2021.1909406

1229 Fujita, M., Reinhart, F., Neutra, M., 1990. Convergence of apical and basolateral endocytic pathways at
1230 apical late endosomes in absorptive cells of suckling rat ileum in vivo. J. Cell Sci. 97, 385–394.
1231 https://doi.org/10.1242/jcs.97.2.385

1232 Fujita, N., Itoh, T., Omori, H., Fukuda, M., Noda, T., Yoshimori, T., 2008. The Atg16L complex specifies the
1233 site of LC3 lipidation for membrane biogenesis in autophagy. Mol. Biol. Cell 19, 2092–2100.
1234 https://doi.org/10.1091/mbc.e07-12-1257

1235 Gong, G., Song, M., Csordas, G., Kelly, D.P., Matkovich, S.J., Dorn, G.W., 2015. Parkin-mediated
1236 mitophagy directs perinatal cardiac metabolic maturation in mice. Science 350, aad2459.
1237 https://doi.org/10.1126/science.aad2459

1238 Gonnella, P.A., Neutra, M.R., 1984. Membrane-bound and fluid-phase macromolecules enter separate
1239 prelysosomal compartments in absorptive cells of suckling rat ileum. J. Cell Biol. 99, 909–917.
1240 https://doi.org/10.1083/jcb.99.3.909

1241 Hansson, J., Panchaud, A., Favre, L., Bosco, N., Mansourian, R., Benyacoub, J., Blum, S., Jensen, O.N.,
1242 Kussmann, M., 2011. Time-resolved Quantitative Proteome Analysis of *In Vivo* Intestinal
1243 Development. Mol. Cell. Proteomics 10, M110.005231. https://doi.org/10.1074/mcp.M110.005231

1244 Harper, J., Mould, A., Andrews, R.M., Bikoff, E.K., Robertson, E.J., 2011. The transcriptional repressor
1245 Blimp1/Prdm1 regulates postnatal reprogramming of intestinal enterocytes. Proc. Natl. Acad. Sci.
1246 U. S. A. https://doi.org/10.1073/pnas.1105852108

1247 He, C., 2022. Balancing nutrient and energy demand and supply via autophagy. Curr. Biol. 32, R684–R696.
1248 https://doi.org/10.1016/j.cub.2022.04.071

1249 Henning, S.J., 1985. Ontogeny of Enzymes in the Small Intestine. Annu. Rev. Physiol. 47, 231–245.
1250 https://doi.org/10.1146/annurev.ph.47.030185.001311

1251 Henning, S.J., 1981. Postnatal development: coordination of feeding, digestion, and metabolism. Am. J.
1252 Physiol.-Gastrointest. Liver Physiol. https://doi.org/10.1152/ajpgi.1981.241.3.G199

1253 Hodzic, Z., Bolock, A.M., Good, M., 2017. The Role of Mucosal Immunity in the Pathogenesis of Necrotizing
1254 Enterocolitis. Front. Pediatr. 5. https://doi.org/10.3389/fped.2017.00040

1255 Hulzebos, C.V., Sauer, P.J.J., 2007. Energy requirements. Semin. Fetal. Neonatal Med., Nutrition 12, 2–
1256 10. https://doi.org/10.1016/j.siny.2006.10.008

1257 Hwang, S., Maloney, N.S., Bruinsma, M.W., Goel, G., Duan, E., Zhang, L., Shrestha, B., Diamond, M.S.,
1258 Dani, A., Sosnovtsev, S.V., Green, K.Y., Lopez-Otin, C., Xavier, R.J., Thackray, L.B., Virgin, H.W.,
1259 2012. Nondegradative role of Atg5-Atg12/ Atg16L1 autophagy protein complex in antiviral activity
1260 of interferon gamma. Cell Host Microbe 11, 397–409. https://doi.org/10.1016/j.chom.2012.03.002

1261 Iborra-Pernichi, M., Ruiz García, J., Velasco de la Esperanza, M., Estrada, B.S., Bovolenta, E.R., Cifuentes,
1262 C., Prieto Carro, C., González Martínez, T., García-Consuegra, J., Rey-Stolle, M.F., Rupérez, F.J.,
1263 Guerra Rodriguez, M., Argüello, R.J., Cogliati, S., Martín-Belmonte, F., Martínez-Martín, N., 2024.
1264 Defective mitochondria remodelling in B cells leads to an aged immune response. Nat. Commun.
1265 15, 2569. https://doi.org/10.1038/s41467-024-46763-1

1266 Jiménez-Loygorri, J.I., Villarejo-Zori, B., Viedma-Poyatos, Á., Zapata-Muñoz, J., Benítez-Fernández, R.,
1267 Frutos-Lisón, M.D., Tomás-Barberán, F.A., Espín, J.C., Area-Gómez, E., Gomez-Duran, A., Boya,

1268 P., 2024. Mitophagy curtails cytosolic mtDNA-dependent activation of cGAS/STING inflammation
1269 during aging. Nat. Commun. 15, 830. https://doi.org/10.1038/s41467-024-45044-1

1270 Kaur, J., Debnath, J., 2015. Autophagy at the crossroads of catabolism and anabolism. Nat. Rev. Mol. Cell
1271 Biol. 16, 461–472. https://doi.org/10.1038/nrm4024

1272 Kawamura, N., Sun-Wada, G.-H., Aoyama, M., Harada, A., Takasuga, S., Sasaki, T., Wada, Y., 2012.
1273 Delivery of endosomes to lysosomes via microautophagy in the visceral endoderm of mouse
1274 embryos. Nat. Commun. 3, 1071. https://doi.org/10.1038/ncomms2069

1275 Kleinman, R.E., Walker, W.A., 1984. Antigen processing and uptake from the intestinal tract. Clin. Rev.
1276 Allergy 2, 25–37. https://doi.org/10.1007/BF02991209

1277 Kulkarni, D.H., Newberry, R.D., 2019. Intestinal Macromolecular Transport Supporting Adaptive Immunity.
1278 Cell. Mol. Gastroenterol. Hepatol. 7, 729–737. https://doi.org/10.1016/j.jcmgh.2019.01.003

1279 Kuma, A., Hatano, M., Matsui, M., Yamamoto, A., Nakaya, H., Yoshimori, T., Ohsumi, Y., Tokuhisa, T.,
1280 Mizushima, N., 2004. The role of autophagy during the early neonatal starvation period. Nature
1281 432, 1032–1036. https://doi.org/10.1038/nature03029

1282 Larabi, A., Barnich, N., Nguyen, H.T.T., 2020. New insights into the interplay between autophagy, gut
1283 microbiota and inflammatory responses in IBD. Autophagy 16, 38–51.
1284 https://doi.org/10.1080/15548627.2019.1635384

1285 Larsson, N.-G., Wang, J., Wilhelmsson, H., Oldfors, A., Rustin, P., Lewandoski, M., Barsh, G.S., Clayton,
1286 D.A., 1998. Mitochondrial transcription factor A is necessary for mtDNA maintance and
1287 embryogenesis in mice. Nat. Genet. 18, 231–236. https://doi.org/10.1038/ng0398-231

1288 Lennicke, C., Cochemé, H.M., 2021. Redox metabolism: ROS as specific molecular regulators of cell
1289 signaling and function. Mol. Cell 81, 3691–3707. https://doi.org/10.1016/j.molcel.2021.08.018

1290 Li, A., Gao, M., Liu, B., Qin, Y., Chen, L., Liu, H., Wu, H., Gong, G., 2022. Mitochondrial autophagy:
1291 molecular mechanisms and implications for cardiovascular disease. Cell Death Dis. 13, 444.
1292 https://doi.org/10.1038/s41419-022-04906-6

1293 Liang, H., Wu, S., Zhang, Z., Khan, M.Z., Zhan, Y., Zhu, M., Wang, S., Liu, W., Wang, C., Cao, G., Han,
1294 Y., 2024. Establishment of a mouse model of ovarian oxidative stress induced by hydrogen
1295 peroxide. Front. Vet. Sci. 11. https://doi.org/10.3389/fvets.2024.1484388

1296 Massaquoi, M.S., Guillemin, K., 2019. Packing in the Proteins. Dev. Cell 51, 1–2.
1297 https://doi.org/10.1016/j.devcel.2019.09.013

1298 McWilliams, T.G., Prescott, A.R., Allen, G.F.G., Tamjar, J., Munson, M.J., Thomson, C., Muqit, M.M.K.,
1299 Ganley, I.G., 2016. mito-QC illuminates mitophagy and mitochondrial architecture in vivo. J. Cell
1300 Biol. 214, 333–345. https://doi.org/10.1083/jcb.201603039

1301 Mizushima, N., Kuma, A., Kobayashi, Y., Yamamoto, A., Matsubae, M., Takao, T., Natsume, T., Ohsumi,
1302 Y., Yoshimori, T., 2003. Mouse Apg16L, a novel WD-repeat protein, targets to the autophagic
1303 isolation membrane with the Apg12-Apg5 conjugate. J. Cell Sci. 116, 1679–1688.
1304 https://doi.org/10.1242/jcs.00381

1305 Mizushima, N., Yamamoto, A., Matsui, M., Yoshimori, T., Ohsumi, Y., 2004. In vivo analysis of autophagy
1306 in response to nutrient starvation using transgenic mice expressing a fluorescent autophagosome
1307 marker. Mol. Biol. Cell 15, 1101–1111. https://doi.org/10.1091/mbc.e03-09-0704

1308 Mizushima, N., Yoshimorim, T., Levine, B., 2010. Methods in Mammalian Autophagy Research. Cell 140,
1309 313–326. https://doi.org/10.1016/j.cell.2010.01.028

1310 Morris, O., Jasper, H., 2021. Reactive Oxygen Species in intestinal stem cell metabolism, fate and function.
1311 Free Radic. Biol. Med. 166, 140–146. https://doi.org/10.1016/j.freeradbiomed.2021.02.015

1312 Moschandrea, C., Kondylis, V., Evangelakos, I., Herholz, M., Schneider, F., Schmidt, C., Yang, M., Ehret,
1313 S., Heine, M., Jaeckstein, M.Y., Szczepanowska, K., Schwarzer, R., Baumann, L., Bock, T.,
1314 Nikitopoulou, E., Brodesser, S., Krüger, M., Frezza, C., Heeren, J., Trifunovic, A., Pasparakis, M.,

1315 2023. Mitochondrial dysfunction abrogates dietary lipid processing in enterocytes. Nature 1–8.
1316 https://doi.org/10.1038/s41586-023-06857-0

1317 Muncan, V., Heijmans, J., Krasinski, S.D., Büller, N.V., Wildenberg, M.E., Meisner, S., Radonjic, M.,
1318 Stapleton, K.A., Lamers, W.H., Biemond, I., Van Den Bergh Weerman, M.A., O'Carroll, D.,
1319 Hardwick, J.C., Hommes, D.W., Van Den Brink, G.R., 2011. Blimp1 regulates the transition of
1320 neonatal to adult intestinal epithelium. Nat. Commun. https://doi.org/10.1038/ncomms1463

1321 Murphy, M.P., 2008. How mitochondria produce reactive oxygen species. Biochem. J. 417, 1–13.
1322 https://doi.org/10.1042/BJ20081386

1323 Ni, H.-M., Bockus, A., Wozniak, A.L., Jones, K., Weinman, S., Yin, X.-M., Ding, W.-X., 2011. Dissecting the
1324 dynamic turnover of GFP-LC3 in the autolysosome. Autophagy 7, 188–204.
1325 https://doi.org/10.4161/auto.7.2.14181

1326 Park, J., Levic, D.S., Sumigray, K.D., Bagwell, J., Eroglu, O., Block, C.L., Eroglu, C., Barry, R., Lickwar,
1327 C.R., Rawls, J.F., Watts, S.A., Lechler, T., Bagnat, M., 2019. Lysosome-Rich Enterocytes Mediate
1328 Protein Absorption in the Vertebrate Gut. Dev. Cell. https://doi.org/10.1016/j.devcel.2019.08.001

1329 Picca, A., Faitg, J., Auwerx, J., Ferrucci, L., D'Amico, D., 2023. Mitophagy in human health, ageing and
1330 disease. Nat. Metab. 5, 2047–2061. https://doi.org/10.1038/s42255-023-00930-8

1331 Popov, L.-D., 2023. Mitochondria as intracellular signalling organelles. An update. Cell. Signal. 109,
1332 110794. https://doi.org/10.1016/j.cellsig.2023.110794

1333 Qi, T., Sun, M., Zhang, C., Chen, P., Xiao, C., Chang, X., 2020. Ascorbic Acid Promotes Plasma Cell
1334 Differentiation through Enhancing TET2/3-Mediated DNA Demethylation. Cell Rep. 33.
1335 https://doi.org/10.1016/j.celrep.2020.108452

1336 Rath, E., Moschetta, A., Haller, D., 2018. Mitochondrial function — gatekeeper of intestinal epithelial cell
1337 homeostasis. Nat. Rev. Gastroenterol. Hepatol. 15, 497–516. https://doi.org/10.1038/s41575-018-
1338 0021-x

1339 Remis, N.N., Wiwatpanit, T., Castiglioni, A.J., Flores, E.N., Cantú, J.A., García-Añoveros, J., 2014.
1340 Mucolipin Co-deficiency Causes Accelerated Endolysosomal Vacuolation of Enterocytes and
1341 Failure-to-Thrive from Birth to Weaning. PLoS Genet. 10.
1342 https://doi.org/10.1371/journal.pgen.1004833

1343 Rodríguez-Colman, M.J., Schewe, M., Meerlo, M., Stigter, E., Gerrits, J., Pras-Raves, M., Sacchetti, A.,
1344 Hornsveld, M., Oost, K.C., Snippert, H.J., Verhoeven-Duif, N., Fodde, R., Burgering, B.M.T., 2017.
1345 Interplay between metabolic identities in the intestinal crypt supports stem cell function. Nature 543,
1346 424–427. https://doi.org/10.1038/nature21673

1347 Rodríguez-Fraticelli, A.E., Bagwell, J., Bosch-Fortea, M., Boncompain, G., Reglero-Real, N., García-León,
1348 M.J., Andrés, G., Toribio, M.L., Alonso, M.A., Millán, J., Perez, F., Bagnat, M., Martín-Belmonte,
1349 F., 2015. Developmental regulation of apical endocytosis controls epithelial patterning in vertebrate
1350 tubular organs. Nat. Cell Biol. 17, 241–250. https://doi.org/10.1038/ncb3106

1351 Rombout, J.H., Lamers, C.H., Helfrich, M.H., Dekker, A., Taverne-Thiele, J.J., 1985. Uptake and transport
1352 of intact macromolecules in the intestinal epithelium of carp (Cyprinus carpio L.) and the possible
1353 immunological implications. Cell Tissue Res. 239, 519–530. https://doi.org/10.1007/BF00219230

1354 Schneider, C.A., Rasband, W.S., Eliceiri, K.W., 2012. NIH Image to ImageJ: 25 years of image analysis.
1355 Nat. Methods 9, 671–675. https://doi.org/10.1038/nmeth.2089

1356 Sena, L.A., Chandel, N.S., 2012. Physiological roles of mitochondrial reactive oxygen species. Mol. Cell
1357 48, 158–167. https://doi.org/10.1016/j.molcel.2012.09.025

1358 Sies, H., Berndt, C., Jones, D.P., 2017. Oxidative Stress. Annu. Rev. Biochem. 86, 715–748.
1359 https://doi.org/10.1146/annurev-biochem-061516-045037

1360 Skrzypek, T., Valverde Piedra, J.L., Skrzypek, H., Kazimierczak, W., Biernat, M., Zabielski, R., 2007.
1361 Gradual disappearance of vacuolated enterocytes in the small intestine of neonatal piglets. J.
1362 Physiol. Pharmacol. Off. J. Pol. Physiol. Soc. 58 Suppl 3, 87–95.

1363 Spence, J.R., Lauf, R., Shroyer, N.F., 2011. Vertebrate intestinal endoderm development. Dev. Dyn.
1364 https://doi.org/10.1002/dvdy.22540

1365 Srivillibhuthur, M., Warder, B.N., Toke, N.H., Shah, P.P., Feng, Q., Gao, N., Bonder, E.M., Verzi, M.P.,
1366 2018. TFAM is required for maturation of the fetal and adult intestinal epithelium. Dev. Biol. 439,
1367 92–101. https://doi.org/10.1016/j.ydbio.2018.04.015

1368 Stirling, D.R., Swain-Bowden, M.J., Lucas, A.M., Carpenter, A.E., Cimini, B.A., Goodman, A., 2021.
1369 CellProfiler 4: improvements in speed, utility and usability. BMC Bioinformatics 22, 433.
1370 https://doi.org/10.1186/s12859-021-04344-9

1371 Subramanian, A., Tamayo, P., Mootha, V.K., Mukherjee, S., Ebert, B.L., Gillette, M.A., Paulovich, A.,
1372 Pomeroy, S.L., Golub, T.R., Lander, E.S., Mesirov, J.P., 2005. Gene set enrichment analysis: A
1373 knowledge-based approach for interpreting genome-wide expression profiles. Proc. Natl. Acad.
1374 Sci. 102, 15545–15550. https://doi.org/10.1073/pnas.0506580102

1375 Trehan, I., Manary, M.J., 2015. Management of severe acute malnutrition in low-income and middle-income
1376 countries. https://doi.org/10.1136/archdischild-2014-306026

1377 Treuting, P.M., Arends, M.J., Dintzis, S.M., 2018. 11 - Upper Gastrointestinal Tract, in: Treuting, P.M.,
1378 Dintzis, S.M., Montine, K.S. (Eds.), Comparative Anatomy and Histology (Second Edition).
1379 Academic Press, San Diego, pp. 191–211. https://doi.org/10.1016/B978-0-12-802900-8.00011-7

1380 Walker, W.A., 2013. Initial Intestinal Colonization in the Human Infant and Immune Homeostasis. Ann. Nutr.
1381 Metab. 63, 8–15. https://doi.org/10.1159/000354907

1382 Wallaeys, C., Garcia-Gonzalez, N., Libert, C., 2023. Paneth cells as the cornerstones of intestinal and
1383 organismal health: a primer. EMBO Mol. Med. 15, e16427.
1384 https://doi.org/10.15252/emmm.202216427

1385 Walter, W., Sánchez-Cabo, F., Ricote, M., 2015. GOplot: an R package for visually combining expression
1386 data with functional analysis. Bioinformatics 31, 2912–2914.
1387 https://doi.org/10.1093/bioinformatics/btv300

1388 Wang, S., Long, H., Hou, L., Feng, B., Ma, Z., Wu, Y., Zeng, Y., Cai, J., Zhang, D., Zhao, G., 2023. The
1389 mitophagy pathway and its implications in human diseases. Signal Transduct. Target. Ther. 8, 304.
1390 https://doi.org/10.1038/s41392-023-01503-7

1391 Wilson, J.M., Whitney, J.A., Neutra, M.R., 1991. Biogenesis of the apical endosome–lysosome complex
1392 during differentiation of absorptive epithelial cells in rat ileum. J. Cell Sci. 100, 133–143.
1393 https://doi.org/10.1242/jcs.100.1.133

1394 Yang, Y., Chen, X., Liao, X., Jiang, W., Zhou, Y., Sun, Y., Zheng, B., 2024. Identification of MAP1LC3A as
1395 a promising mitophagy-related gene in polycystic ovary syndrome. Sci. Rep. 14, 16982.
1396 https://doi.org/10.1038/s41598-024-67969-9

1397 Yim, W.W.-Y., Mizushima, N., 2020. Lysosome biology in autophagy. Cell Discov. 6, 6.
1398 https://doi.org/10.1038/s41421-020-0141-7

1399 Yu, G., Wang, L.-G., Han, Y., He, Q.-Y., 2012. clusterProfiler: an R Package for Comparing Biological
1400 Themes Among Gene Clusters. OMICS J. Integr. Biol. 16, 284–287.
1401 https://doi.org/10.1089/omi.2011.0118

1402 Zemirli, N., Morel, E., Molino, D., 2018. Mitochondrial Dynamics in Basal and Stressful Conditions. Int. J.
1403 Mol. Sci. 19, 564. https://doi.org/10.3390/ijms19020564

1404 Zhao, Y.G., Codogno, P., Zhang, H., 2021. Machinery, regulation and pathophysiological implications of
1405 autophagosome maturation. Nat. Rev. Mol. Cell Biol. 22, 733–750. https://doi.org/10.1038/s41580-
1406 021-00392-4

1407 Zhong, Y., Xia, S., Wang, G., Liu, Q., Ma, F., Yu, Y., Zhang, Y., Qian, L., Hu, L., Xie, J., 2024. The interplay
1408 between mitophagy and mitochondrial ROS in acute lung injury. Mitochondrion 78, 101920.
1409 https://doi.org/10.1016/j.mito.2024.101920

1410

1411 **METHODS**

1412 **KEY RESOURCES TABLE**

REAGENT or RESOURCE	SOURCE	IDENTIFIER
Antibodies		
Mouse monoclonal anti-GFP, HRP-conjugated (clone GG4-2C2.12.10)	Miltenyi Biotec	130-091-833
Rat monoclonal anti-RFP (clone 5F8)	Chromotek	5F8
Rabbit polyclonal anti-USP7	Bethyl	A300-033A
Rabbit polyclonal anti-ATG16L1	MBL	PM040
Mouse monoclonal anti-LC3C (clone E5Q2K)	CST	83506
Rabbit polyclonal anti-Actin	Sigma	A2103
Mouse monoclonal anti-SQSTM1 (clone 2C11)	Abnova	H00008878-M01
Mouse monoclonal anti-Dab2 (clone 52/p96)	BD Biosciences	610464
Rat monoclonal anti-LAMP1 (clone 1D4B)	DSHB	1D4B
Rabbit polyclonal anti-Trehalase	GeneTex	GTX109979
Rabbit polyclonal anti-β-catenin	Santa Cruz Biotechnology	sc-7199
Rabbit polyclonal anti-Parkin	Abcam	ab15494
Rabbit polyclonal anti-MafB	Novus Biologicals	NBP1-81342
Rabbit polyclonal anti-Blimp1	Invitrogen	PA5-20310
Mouse monoclonal anti-E-Cadherin (clone 36/E)	BD Biosciences	610181
Goat polyclonal anti-GPX3	R&D Systems	AF4199
Mouse monoclonal anti-MTCO1 (clone 1D6E1A8)	Thermo Fisher Scientific	459600
Rabbit monoclonal anti-Olfm4 (clone D6Y5A)	CST	39141
Rabbit polyclonal anti-Lysozyme	Dako	A0099
Alexa Fluor 647 rabbit monoclonal anti-ASS1 (clone EPR12398)	Abcam	ab311083
Rat monoclonal anti-CD16/32 (clone 93)	Biolegend	101330
PerCP-eFluor710 rat monoclonal anti-EpCAM (clone G8.8)	Invitrogen	46-5791-82
APC rat monoclonal anti-EpCAM (clone G8.8)	Biolegend	118214
BV605 rat monoclonal anti-EpCAM (clone G8.8)	Biolegend	118227
Pacific Blue rat monoclonal anti-CD24 (Clone M1/69)	Biolegend	101820
PE rat monoclonal anti-c-Kit (clone 2B8)	Biolegend	105807
BV785 rat monoclonal anti-c-Kit (clone 2B8)	Biolegend	105841
Alexa Fluor 700 rat monoclonal anti-CD11b (clone M1/70)	Biolegend	101222
Biotin rat monoclonal anti-CD11c (clone N418)	Biolegend	105841
APC-Fire810 rat monoclonal anti-B220 (clone RA3-6B2)	Biolegend	103278
APC-Fire810 rat monoclonal anti-CD4 (clone GK1.5)	Biolegend	100480
RY586 rat monoclonal anti-CD4 (clone GK1.5)	BD Biosciences	568162
Biotin rat monoclonal anti-CD19 (clone 6D5)	Biolegend	115504
Biotin rat monoclonal anti-CD3e (clone 145-2C11)	Biolegend	79751
Biotin rat monoclonal anti-CD45.2 (clone 104)	Biolegend	109804
Rabbit polyclonal anti-GLS	Thermo Fisher Scientific	PA5-35365
Alexa Fluor 647 rabbit monoclonal anti-HK1 (clone EPR10134(B))	Abcam	ab197864

Alexa Fluor 488 mouse monoclonal anti-CPT1A (clone 8F6AE9)	Abcam	ab171449
Rabbit monoclonal anti-ACAC (clone EPR23235-147)	Abcam	ab269273
Alexa Fluor 488 rabbit monoclonal anti-CS (clone EPR8067)	Abcam	ab197488
PE rabbit monoclonal anti-IDH2 (clone EPR7577)	Abcam	ab212122
Alexa Fluor 594 rabbit monoclonal anti-ATP5A (clone EPR23235- 147)	Abcam	ab216385
BB700 rat monoclonal anti-BLIMP1 (clone 5E7)	BD Biosciences	567830
Alexa Fluor 488 donkey polyclonal anti-mouse IgGs	Thermo Fisher Scientific	A-21202
Alexa Fluor 488 donkey polyclonal anti-rabbit IgGs	Thermo Fisher Scientific	A-21206
Alexa Fluor 488 donkey polyclonal anti-rat IgGs	Thermo Fisher Scientific	A-21208
Alexa Fluor 555 donkey polyclonal anti-mouse IgGs	Thermo Fisher Scientific	A-31570
Alexa Fluor 647 donkey polyclonal anti-rabbit IgGs	Thermo Fisher Scientific	A-31573
Alexa Fluor 647 donkey polyclonal anti-mouse IgGs	Thermo Fisher Scientific	A-31571
Peroxidase AffiniPure donkey polyclonal Anti-Mouse IgG	Jackson Immunoresearch	715-035-151
HRP donkey anti-rabbit IgG	Cytiva	NA934
Peroxidase AffiniPure goat polyclonal Anti-Rat IgG	Jackson Immunoresearch	112-035-003
Chemicals, peptides, and recombinant proteins		
Tamoxifen	Merck	T5648
Leupeptin	Sigma	L2884
Hydrogen Peroxide 30%	Merck	108597
Dextran rhodamine B, 10000MW, neutral	Invitrogen	D1824
Dextran Alexa Fluor 647, 10000MW, anionic, fixable	Invitrogen	D22914
Paraformaldehyde, powder, TECHNICAL	VWR Chemicals	28794.295
Tissue-Tek O.C.T. Compound	Sakura	4583
Sucrose	Merck	1076511000
DAPI	Merck	268298
Phalloidin Alexa Fluor™ 488	ThermoFisher	A12379
Phalloidin Alexa Fluor™ 647	ThermoFisher	A22287
ProLong™ Glass Antifade Mountant	Thermo Fisher	P36984
Ghost Dye Violet 540	TONBO Biosciences	13-0879-T100
Ghost Dye Red 780	TONBO Biosciences	13-0865-T100
Streptavidin-BV421	Biolegend	405225
CM-H2DCFDA	Invitrogen	C6827
MitoTracker Green FM	Invitrogen	M7514
MitoTracker Red CMXRos	Invitrogen	M7512
MitoSOX	Invitrogen	M36008
LysoTracker Green DND-26	Invitrogen	L7526
eBioscience FOXP3/Transcription Factor Staining Buffer Set	Invitrogen	00-5523-00
ECL Western Blotting Reagents	Cytiva	RPN2106
DTT	Thermo Scientific	R0861
Oligonucleotides		
Genotyping primers for *Atg16l1*$^{fl/fl}$: forward: 5' CTTTCTCAACAGAACCAGCAGTAC 3'	IDT	N/A
Genotyping primers for *Atg16l1*$^{fl/fl}$: reverse: 5' GTTCAGGTCAATCACCAACTGAGC 3'	IDT	N/A

Genotyping primers for *Tfam*$^{fl/fl}$: forward: 5' CTGCCTTCCTCTAGCCCGGG 3'	IDT	N/A
Genotyping primers for *Tfam*$^{fl/fl}$: reverse: 5' GTAACAGCAGACAACTTGTG 3'	IDT	N/A
Genotyping primers for *Tfam*$^{fl/fl}$: reverse-2: 5' CTCTGAAGCACATGGTCAAT- 3'	IDT	N/A
Genotyping primers for *Villin-creER*^{T2}: forward: 5'- CAAGCCTGGCTCGACGGCC -3'	Sigma	N/A
Genotyping primers for *Villin-creER*^{T2}: reverse: 5'-CGCGAACATCTTCAGGTTCT-3'	Sigma	N/A
Genotyping primers for m*ito-QC*: forward: 5'- CAAAGACCCCAACGAGAAGC -3'	IDT	N/A
Genotyping primers for *mito-QC*: forward-2: 5'- CCCAAGGCACACAAAAAACC -3'	IDT	N/A
Genotyping primers for *mito-QC*: reverse: 5'-CTCTTCCCTCGTGACCTGCAACTCC-3'	IDT	N/A
Genotyping primers for *mito-QC*: reverse-2: 5'- CATGTCTTTAATCTACCTCGATGG -3'	IDT	N/A
Genotyping primers for *GFP-LC3*: forward: 5'-ATAACTTGCTGGCCTTTCCACT -3'	IDT	N/A
Genotyping primers for *GFP-LC3*: reverse: 5'- CGGGCCATTTACCGTAAGTTAT-3'	IDT	N/A
Genotyping primers for *GFP-LC3*: reverse-2: 5'-GCAGCTCATTGCTGTTCCTCAA-3'	IDT	N/A
RT-qPCR primers for *Atg16l1*: forward: 5' ACATGATGGTGCGTGGAATG 3'	Sigma	N/A
RT-qPCR primers for *Atg16l1*: reverse: 5' TCCTTGTCCTTCTGCTGCAT 3'	Sigma	N/A
RT-qPCR primers for *Tfam*: forward: 5' CAGGAGGCAAAGGATGATTC 3'	Sigma	N/A
RT-qPCR primers for *Tfam*: reverse: 5' CCAAGACTTCATTTCATTGTCG 3'	Sigma	N/A
RT-qPCR primers for *Dab2*: forward: 5' CGAAAGCGCCATCAAAGAAG 3'	IDT	N/A
RT-qPCR primers for *Dab2*: reverse: 5' CCTTTGAACCTGGCCAACAA 3'	IDT	N/A
RT-qPCR primers for *Mcoln3*: forward: 5' ATGGAGTTCATCAACGGGTG 3'	IDT	N/A
RT-qPCR primers for *Mcoln3*: reverse: 5' ATAGTTGACGTCCCGAGAAG 3'	IDT	N/A
RT-qPCR primers for *Lamp2*: forward: 5' TGCAGAATGGGAGATGAATTT 3'	IDT	N/A
RT-qPCR primers for *Lamp2*: reverse: 5' GGCACTATTCCGGTCATCC 3'	IDT	N/A
RT-qPCR primers for *Ctsl1*: forward: 5' CCAGCTACACAACGGGGAAT 3'	IDT	N/A
RT-qPCR primers for *Ctsl1*: reverse: 5' AGCATCAGCGGTTCCTGAAA 3'	IDT	N/A
RT-qPCR primers for *Bnip3*: forward: 5' TGTTGGATGCCCAGCATGAA 3'	IDT	N/A
RT-qPCR primers for *Bnip3*: reverse: 5' AATCTTCCTCAGACAGAGTGCT 3'	IDT	N/A
RT-qPCR primers for *Prkn*: forward: 5' AAACCGGATGAGTGGTGAGT 3'	IDT	N/A

RT-qPCR primers for *Prkn*: reverse: 5' AGCTACCGACGTGTCCTTGT 3'	IDT	N/A
RT-qPCR primers for *Pink1*: forward: 5' GCTGATCGAGGAGAAGCAG 3'	IDT	N/A
RT-qPCR primers for *Pink1*: reverse: 5' GATAATCCTCCAGACGGAAGC 3'	IDT	N/A
RT-qPCR primers for *Mafb*: forward: 5' AGAGGCGGACCCTGAAAAAC 3'	IDT	N/A
RT-qPCR primers for *Mafb*: reverse: 5' GTTTTCTCGGAAGCCGTTGC 3'	IDT	N/A
RT-qPCR primers for *c-maf*: forward: 5' GCATGCTGGACATGTATGGT 3'	IDT	N/A
RT-qPCR primers for *c-maf*: reverse: 5' ATGTACAACGGGAGGCTGAA 3'	IDT	N/A
RT-qPCR primers for *Blimp1*: forward: 5' TTCTTGTGTGGTATTGTCGGGACTT 3'	Sigma	N/A
RT-qPCR primers for *Blimp1*: reverse: 5' TTGGGGACACTCTTTGGGTAGAGTT 3'	Sigma	N/A
RT-qPCR primers for *Ass1*: forward: 5' CATTGGAATGAAGTCCCGAG 3'	IDT	N/A
RT-qPCR primers for *Ass1*: reverse: 5' GATTTTGCGTACTTCCCGAT 3'	IDT	N/A
RT-qPCR primers for *Glb1*: forward: 5' ACTGCTGCAACTGCTGGG 3'	Sigma	N/A
RT-qPCR primers for *Glb1*: reverse: 5' AATGGCTGTCCATCCTTGAG 3'	Sigma	N/A
RT-qPCR primers for *Treh*: forward: 5' GCACCTGCTGCTTCTGCT 3'	Sigma	N/A
RT-qPCR primers for *Treh*: reverse: 5' CATCTGAACTTGGTGCAGGA 3'	Sigma	N/A
RT-qPCR primers for *Sis*: forward: 5' GCCCACGCGTTTGGTGAGAC 3'	Sigma	N/A
RT-qPCR primers for *Sis*: reverse: 5' ATCAGCAGTGCAGGGCCCCA 3'	Sigma	N/A
RT-qPCR primers for *Arg2*: forward: 5' TGATTGGCAAAAGGCAGAGG 3'	Sigma	N/A
RT-qPCR primers for *Arg2*: reverse: 5' CTAGGAGTAGGAAGGTGGTC 3'	Sigma	N/A
RT-qPCR primers for *Gpx3*: forward: 5' AATTAGGCACAAAGCCCCCA 3'	IDT	N/A
RT-qPCR primers for *Gpx3*: reverse: 5' CATTCTGGGCTTCCCTTCCA 3'	IDT	N/A
RT-qPCR primers for *Cat*: forward: 5' GAACGGCAATAGGGGTCCTC 3'	IDT	N/A
RT-qPCR primers for *Cat*: reverse: 5' TGGTACACGCAAAAGGAGCA 3'	IDT	N/A
RT-qPCR primers for *Amn*: forward: 5' ATCTGTGAGAGCCTCGGCG 3'	IDT	N/A
RT-qPCR primers for *Amn*: reverse: 5' GTTGGAGGCAGTATCGAAGGA 3'	IDT	N/A
RT-qPCR primers for *Mamdc4*: forward: 5' TCACCACTGCCAGAACAAGG 3'	IDT	N/A
RT-qPCR primers for *Mamdc4*: reverse: 5' CTAACTGGTTCCACGGTCCC 3'	IDT	N/A

RT-qPCR primers for *mt-Nd1*: forward: 5' TCCCCTACCAATACCACACC 3'	Sigma	N/A
RT-qPCR primers for *mt-Nd1*: reverse: 5' TGAAATTGTTTGGGCTACGG 3'	Sigma	N/A
RT-qPCR primers for *mt-Co2*: forward: 5' ACGAAATCAACAACCCCGTA 3'	Sigma	N/A
RT-qPCR primers for *mt-Co2*: reverse: 5' GGCAGAACGACTCGGTTATC 3'	Sigma	N/A
RT-qPCR primers for *Sdha*: forward: 5' GCGGCTTTCACTTCTCTGTT 3'	IDT	N/A
RT-qPCR primers for *Sdha*: reverse: 5' CTCAGAAAGGCCAAATGCAG 3'	IDT	N/A
qPCR primers for *mt-Co1*: forward: 5' ATCCCTTGACATCGTGCTTC 3'	Sigma	N/A
qPCR primers for *mt-Co1*: reverse: 5' AAGTGGGCTTTTGCTCATGT 3'	Sigma	N/A
qPCR primers for *mt-Atp6*: forward: 5' ACAGGCTTCCGACACAAACT 3'	Sigma	N/A
qPCR primers for *mt-Atp6*: reverse: 5' GGTAGCTGTTGGTGGGCTAA 3'	Sigma	N/A
qPCR primers for *Hk2*: forward: 5' GCCAGCCTCTCCTGATTTTAGTGT 3'	Sigma	N/A
qPCR primers for *Hk2*: reverse: 5' GGGAACACAAAAGACCTCTTCTGG 3'	Sigma	N/A
RT-qPCR primers for *Ppib*: forward: 5' CACCAATGGCTCACAGTTCTT 3'	IDT	N/A
RT-qPCR primers for *Ppib*: reverse: 5' ATGACATCCTTCAGTGGCTTG 3'	IDT	N/A

Mice

Atg16l1$^{fl/fl}$ (Hwang et al., 2012), *Tfam*$^{fl/fl}$ (Larsson et al., 1998), and GFP-LC3 (Mizushima et al., 2004) mice were kindly provided by N. Martínez-Martín (Centro de Biología Molecular "Severo Ochoa", CBM, CSIC-UAM, Madrid, Spain). The *mito*-QC mouse line (McWilliams et al., 2016) was obtained from P. Boya (Centro de Investigaciones Biológicas Margarita Salas, CSIC, Madrid, Spain; University of Fribourg, Switzerland). *Villin-creER*^{T2} mice (el Marjou et al., 2004) were provided by N. Djouder (Spanish National Cancer Research Centre, CNIO, Madrid, Spain). *Atg16l1* $^{fl/fl}$, *Tfam* $^{fl/fl}$ mice were crossed at the CBM animal facility with *Villin-creER*^{T2} mice to generate intestinal epithelial-specific conditional knockout (cKO) mice: *Atg16*cKO and *Tfam*cKO, respectively. In turn, *Atg16*cKO mice were crossed with *mito*-QC mice to establish *the mQ-Atg16*cKO mouse line. Tamoxifen (0.12–0.5 mg in corn oil containing 10% ethanol) was administered subcutaneously at postnatal days 1 and 2 to pups from *Atg16*cKO, *mQ-Atg16*cKO, and *Tfam*cKO litters, following a protocol similar to that described by Gong et al. (2015). Cre-positive animals were classified as KO, and Cre-negative mice as WT. Neonatal mice were humanely sacrificed by decapitation; adult mice were euthanized via CO_2 inhalation. *Tfam*cKO neonates were sacrificed after two consecutive days without weight gain or upon observing approximately a 10% weight loss, in accordance with humane endpoint criteria. No test was performed to determine the influence of sex, as no apparent differences were found.

1432 Mouse colonies were maintained at CBM under specific pathogen-free conditions and on a C57BL/6 genetic
1433 background. Mice were housed four/five per cage with food and water available ad libitum and maintained
1434 in a temperature-controlled environment on a 12 h–12 h light–dark cycle with light onset at 08:00. Animal
1435 experiments were performed under protocols approved by the CBM and Comunidad Autónoma de Madrid
1436 ethical committees under the following protocol approval number (PROEX 307.2/21). All animal procedures
1437 conformed to EU Directive 86/609/EEC and Recommendation 2007/526/EC regarding the protection of
1438 animals used for experimental and other scientific purposes, enforced in Spanish law under Real Decreto
1439 1201/2005.
1440
1441 **mCherry / fluorescent-dextran uptake assay**
1442 Mice from GFP-LC3, *Atg16*cKO, and *Tfam*cKO lines were fasted for 1 hour and orally gavaged with either
1443 mCherry or 10 kDa fluorescent-dextran (0.3–1 mg/ml in PBS; 10 µl/g body weight). Following gavage, mice
1444 were sacrificed either 3 or 16 hours later, adapted from the protocol reported by Remis et al. (2014). To
1445 test the endocytic function in neonatal enterocytes, WT mice at postnatal day 7 (P7) were sequentially
1446 gavaged with two distinct 10 kDa fluorescent-dextrans (0.7 mg/ml in PBS; 10 µl/g body weight), following a
1447 modified version of the protocol established in mouse embryos by Kawamura et al. (2012). After a 1-hour
1448 fasting period, pups were first gavaged with Alexa Fluor 647-dextran and then returned to their mother.
1449 Three hours later, they were given rhodamine B–dextran again. Pups were subsequently sacrificed either
1450 1 or 5 hours after the second gavage, and ileal enterocytes were analysed by confocal microscopy to assess
1451 dextran uptake and intracellular localization.
1452
1453 **Leupeptin and hydrogen peroxide treatment**
1454 To inhibit lysosomal proteases and block autophagy, mice were injected subcutaneously with 40 mg/Kg
1455 leupeptin (Sigma) dissolved in PBS and sacrificed after 16h (Jiménez-Loygorri et al., 2024). To assess the
1456 effect of ROS on intestinal epithelial maturation, mice were injected intraperitoneally with hydrogen peroxide
1457 (5.1 µmol/g body weight; Merck) once daily from postnatal day (P)5 to P12 (day of sacrifice), following a
1458 protocol adapted from Liang et al. (2024).
1459
1460 **Histology and Immunofluorescence**
1461 Portions of the distal small intestine from mice were fixed in 4% PFA for 16 hours at 4 °C, embedded in
1462 paraffin resin, and cut transversely into 5-µm sections. Some samples were stained with hematoxylin-eosin
1463 (HE&E; Sigma and Merck, respectively), while others underwent Periodic Acid-Schiff (PAS) staining.
1464 Additionally, some samples were used for immunofluorescence. For immunofluorescence, sections were
1465 deparaffinized using xylene and then rehydrated through a series of decreasing ethanol concentrations
1466 (100%, 96%, 70%, 50%). For antigen retrieval, tissue was boiled at 100 °C on a heat block in sodium citrate
1467 buffer (10 mM Sodium citrate, 0.05% Tween 20, pH 6.0) for 20 min. Next, the slides were washed with
1468 water and PBS containing calcium and magnesium, and then incubated for 1 hour at room temperature

1469 with 3% bovine serum albumin (BSA) as a blocking solution. For O.C.T. embedded sections, portions of
1470 the distal small intestine were previously fixed in 4% PFA for 16 hours at 4 °C, incubated in 30% sucrose
1471 in PBS for 48-72 hours at 4 °C, and then embedded in O.C.T. compound and stored at -80 °C until use.
1472 O.C.T. blocks were cut transversely into 15 µm sections using Superfrost Plus Adhesion Microscope Slides
1473 (Epredia) and stored at -80 °C. For immunofluorescence, sections were dried at room temperature for 30
1474 minutes, washed with 0.1% Tween 20, and blocked for 1 hour at room temperature with BGT buffer (0.3%
1475 BSA, 0.75% Glycine, 0.3% Triton X-100 in PBS). For both paraffin-embedded and O.C.T.-embedded
1476 samples, the primary antibody was added and incubated overnight at 4 °C in the respective blocking buffer.
1477 After washing with PBS, the secondary antibody was incubated with DAPI for 1h at RT. Lastly, slides were
1478 assembled with coverslips with Prolong Glass Antifade (Thermo Fisher). Antibodies used are specified in
1479 the key resources table.
1480
1481 **Image Acquisition and Analysis**
1482 HE&E and PAS staining images were acquired using an Axio Imager M1 vertical wide-field microscope,
1483 coupled with a Leica DMC6200 CMOS Colour camera. The objective used was 10X/0.3 Air EC Plan-Neo.
1484 LASXv4.13 software was used to stitch the tiles into an image. The analysis of goblet cells, villi length, and
1485 submucosa–lower mucosa thickness was performed using Fiji (ImageJ 1.54f; https://fiji.sc/) (Wayne
1486 Rasband, NIH, USA) (Schneider et al., 2012). Lower mucosa was defined as the sum of the *muscularis*
1487 *mucosae*, *lamina propria* and epithelial compartment of the crypts. For villi length analysis, the 10 longest
1488 villi per section were chosen. One section per mouse was analysed from 3–6 mice per genotype. For
1489 immunofluorescence, images were acquired using a Zeiss LSM 900 confocal microscope mounted on an
1490 Axio Imager Z2 upright stand, with sequential acquisition and bidirectional scanning. For individual fields, a
1491 63×/1.4 NA oil-immersion Plan-Apochromat objective was used, with a voxel size of 50 × 50 × 520 nm. For
1492 tile scans, images were acquired using a 20×/0.8 NA air Plan-Apochromat objective, with a voxel size of
1493 0.624 × 0.624 × 1.9 µm, and stitched using ZEN Blue software version 3.4 (Zeiss;
1494 https://www.zeiss.com/zen). For the analysis of Paneth cells and Olfm4^{+} crypts in the ileum of *Tfam*cKO
1495 mice, all cells and all crypts were quantified per section (one section per mouse; 3 mice per genotype). For
1496 intensity analysis, all images were acquired with 16-bit resolution and under the same conditions. An
1497 average intensity projection was made, and the endothelial cells (lacteal vessel) were cropped. The same
1498 threshold was applied to all images to select positive areas. Images were analysed using CellProfiler 4.2.8
1499 (https://cellprofiler.org/) (Stirling et al., 2021) and Fiji (ImageJ 1.54f) (Schneider et al., 2012). Intensity
1500 values correspond to the integrated density, normalized to the epithelial nuclear area (defined by DAPI in
1501 epithelial cells) for BLIMP1 and MAFB, or to the epithelial area (delimited by β-catenin, E-cadherin, or F-
1502 actin) for all other markers, except for LAMP1 (in both KO models) and Rd-dextran (only in *Atg16*cKO mice),
1503 which were not normalized. For LAMP1 intensity and area analysis in *Tfam*cKO mice, images were
1504 deconvolved using Huygens Professional software (version 24.10; Scientific Volume Imaging,
1505 https://svi.nl/Huygens-Professional). For the analysis of Rd-dextran intensity and LAMP1 area and intensity

1506 in *Atg16*cKO mice, 25–40 and 26–36 enterocytes per condition were analysed, respectively. For LAMP1
1507 area and intensity analysis in *Tfam*cKO mice, a minimum of 30 enterocytes per mouse were quantified,
1508 across 3 mice per group (99–167 enterocytes per group). For all other intensity analyses, 2–5 random
1509 images per mouse were acquired from comparable villi, each containing approximately 50 cells, with 2–5
1510 mice per group.
1511
1512 **Transmission Electron Microscopy**
1513 Samples were processed by the Electron Microscopy Unit at CBM. Distal small intestine portions were fixed
1514 using 4% PFA (paraformaldehyde) and 2% glutaraldehyde in phosphate buffer 0.1M, pH 7.4, for 2 hours at
1515 room temperature. Then they were washed 3 times for 10 minutes with phosphate buffer. After fixation, the
1516 material was post-fixed in 1% osmium tetroxide and potassium ferricyanide for 1 hour at 4 °C, then
1517 embedded in tannic acid for 1 minute and block-stained with 2% uranyl acetate for 1 hour in the dark. Next,
1518 they were dehydrated in crescent concentrations of ethanol (30%, 50%, 70%, 95%, 3x100%; 10 minutes
1519 each) and infiltrated in propylene oxide for 45 minutes and Epon 100% for 1 hour. Finally, the samples were
1520 introduced into BEEM capsules (ESBE Scientific). Samples were observed using a JEM1400 Flash
1521 Transmission Electron Microscope (JEOL) equipped with a CMOS OneView camera (Gatan). Fiji (ImageJ
1522 1.54f) (Schneider et al., 2012) was used for image analysis. Mitochondria were classified into three
1523 categories, as in Moschandrea et al. (2023): class I (normal), characterized by mitochondria with narrow
1524 and well-defined cristae; class II (partly affected), with mitochondria exhibiting undefined cristae; and class
1525 III (damaged), including mitochondria with wide, short, and less electron-dense cristae, or those with
1526 ruptured membranes or internal inclusions. For the analysis of mitochondrial status in *Atg16*cKO mice, 291–
1527 340 mitochondria were analysed from 10–11 enterocytes (3 mice per genotype). For *Tfam*cKO mice, in the
1528 analysis of number and percentage of mitochondrial classes, 444–1040 mitochondria from 13–24
1529 enterocytes (3–4 mice per group) were used; for area and aspect ratio analysis, 261–520 mitochondria
1530 from 11–17 enterocytes (2–4 mice per group) were analysed. The graphs show data after outlier exclusion.
1531
1532 **Isolation of IEC**
1533 Mice were euthanized, and the abdominal cavity was opened to expose the intestine. The region of interest
1534 (proximal or distal intestine) was dissected, removed, and rinsed in PBS. The tissue was cut transversely
1535 into ~5 mm fragments, which were then opened longitudinally and incubated in epithelial dissociation buffer
1536 (1 mM DTT, 1 mM EDTA, 2% FBS in PBS) at 37°C with agitation for 20 minutes. After incubation, the
1537 samples were centrifuged at 1200 rpm for 5 minutes. The supernatant was discarded, and the pellet was
1538 resuspended in 10 mL of DMEM supplemented with 10% FBS at 4 °C. The suspension was passed through
1539 70 µm cell strainers (Falcon) and then centrifuged again at 1,200 rpm for 5 minutes. The resulting pellet
1540 was resuspended in FACS buffer (1 mM EDTA, 2% FBS in PBS) at 4 °C and centrifuged again under the
1541 same conditions. The final pellet containing epithelial cells was used for western blotting, flow cytometry,
1542 and RT-qPCR analysis.

1543

1544 **Immunoblotting**

1545 IECs pellets were lysed with lysis buffer (50 mM Tris-HCl, 150 mM NaCl, 1% NP-40, 50 mM NaF, 0.1%
1546 SDS, 1 mM Na_3VO_4, 30 mM β-glycerophosphate, 5 mM EDTA, protease inhibitors) and centrifuged for 10
1547 minutes at 4 °C, 15,000 rpm. Supernatants were collected and quantified using the Bradford protein assay
1548 (Biorad Protein Assay, Biorad). 25 µg of protein was loaded in 10 or 12% acrylamide gels for SDS-PAGE.
1549 After electrophoresis, proteins were transferred to an Immobilon-P transfer membrane (Millipore), blocked
1550 for 1 hour, and incubated overnight with primary antibodies at 4 °C. After washing with 0.05% Tween 20,
1551 they were incubated with HRP-conjugated secondary antibodies for 1 hour at room temperature. ECL
1552 western blotting reagents (Cytiva) were used for the chemiluminescence reaction. Bands were analysed
1553 using Fiji (ImageJ 1.54f) (Schneider et al., 2012). Antibodies used are specified in the key resources table.

1554

1555 **Flow Cytometry**

1556 Disaggregated epithelial cells were plated into a 96-well plate and incubated with FACS buffer with anti-
1557 CD16/CD32 Fc block and viability markers (Ghost Dye) for 10 min at room temperature. After centrifugation,
1558 cells were incubated for 20 min at 4ºC with the appropriate combination of the antibodies in FACS buffer to
1559 discern between the different epithelial and immune populations. Following protocols adapted from
1560 immunometabolic (Baixauli et al., 2015; Iborra-Pernichi et al., 2024) and intestinal studies (Asano et al.,
1561 2017), we assessed mitochondrial mass and membrane potential, cellular and mitochondrial ROS levels,
1562 and lysosomal content labelling cells with MitoTracker Green FM (50 nM), MitoTracker Red CMXRos (100
1563 nM), CM-H2DCFDA (2.5 µM), MitoSOX (1 µM), and Lysotracker Green DND-26 (100 nM), respectively.
1564 Probes were incubated for 15 min at room temperature and 15 min at 37 °C in DMEM with 5% FBS
1565 (Lysotracker), without FBS (MitoTracker and CM-H2DCFDA), or in HBSS (MitoSOX). Antibodies used are
1566 specified in the key resources table. Data were acquired using a Cytek Aurora full-spectrum cytometer at
1567 the CBM, and analysed with FlowJo software (versions 10 and 10.8.1; BD Biosciences). See Figure S3 for
1568 details on the gating strategies.

1569

1570 **Met-flow cytometry staining**

1571 Based on recent works on immune cell metabolism (Ahl et al., 2020; Iborra-Pernichi et al., 2024), we
1572 selected eight key metabolic enzymes to analyse their expression by flow cytometry in our epithelial cells:
1573 ASS1, GLS, HK1, CPT1A, ACAC, CS, IDH2, and ATP5A. After the disaggregated epithelial cells were
1574 incubated with surface antibodies according to the flow cytometry protocol, they were fixed and
1575 permeabilized using the eBioscience Foxp3/Transcription Factor Staining Buffer Set (Invitrogen). Next, they
1576 were washed in the provided wash buffer and blocked with 20% FBS in wash buffer and incubated for 2h
1577 at room temperature with the appropriate antibodies to detect the rate-limiting enzymes from different
1578 metabolic pathways. Lastly, they were rewashed with wash buffer. Antibodies used are specified in the key

1579 resources table. Data were acquired using a Cytek Aurora full-spectrum cytometer at the CBM, and
1580 analysed with FlowJo software (versions 10 and 10.8.1; BD Biosciences).
1581
1582 **RNA Sequencing and Bioinformatic Analyses**
1583 The FACS gating strategy used to isolate LREs and PECs for RNA sequencing (RNA-seq) is shown in
1584 Figure S4A. Cell sorting was performed using a FACSAria Fusion cytometer (BD Biosciences). Each
1585 population was collected in biological triplicate samples of 300,000–500,000 cells. For LREs, each replicate
1586 consisted of pooled cells from multiple neonatal litters; for PECs, each replicate corresponded to a single
1587 mouse at postnatal day 42 (P42). Cells were collected in RLT buffer (Qiagen), and total RNA was extracted
1588 using the RNeasy Plus Micro Kit (Qiagen). Samples with an RNA integrity number (RIN) >7.0 were selected
1589 for RNA-seq. Ultra-low input poly(A)-selected libraries (single-end) were prepared in triplicate and
1590 sequenced using the Illumina HiSeq 2500 platform (50 bp, single-end reads) at the Centro de Análisis
1591 Genómico (CNAG-CRG, Barcelona, Spain). Reads were aligned to the Mus musculus reference genome
1592 (mm39) using HISAT2 (v2.1.0), and gene counts were obtained using HTSeq-count (v0.11.2). Differential
1593 gene expression analysis was performed with DESeq2. Gene Set Enrichment Analysis (GSEA)
1594 (Subramanian et al., 2005) was conducted using the clusterProfiler (Yu et al., 2012) and enrichplot
1595 packages within the R environment. Predefined gene sets from the Gene Ontology (GO) database were
1596 assessed for statistically significant enrichment based on a ranked list of gene expression values. The full
1597 gene dataset, annotated with ENSEMBL identifiers and their associated statistical metrics (stat), was
1598 utilized as input for the GSEA. Enrichment was quantified by normalized enrichment scores (NES), with
1599 significance determined at an adjusted p-value threshold of < 0.05 following Benjamini-Hochberg
1600 correction. Over-Representation Analysis (ORA) (Boyle et al., 2004) was performed in R using the
1601 clusterProfiler package. Differentially expressed genes (DEGs) with an adjusted p-value < 0.05 and
1602 mapped using ENTREZID identifiers were used. Enriched GO terms and KEGG pathways were also filtered
1603 at an adjusted p-value < 0.05 (Benjamini-Hochberg correction). Selected GO and KEGG terms were
1604 visualized using bubble plots generated in R with the GOplot package (GOBubble function) (Walter et al.,
1605 2015). The biocomputational data analysis was carried out by the Biocomputational Analysis Service
1606 (SABio) at the Centro de Biologia Molecular "Severo Ochoa" (CSIC-UAM).
1607
1608 **RNA Extraction, cDNA Synthesis, and RT-qPCR**
1609 Epithelial cells were lysed in 500 µL of TRIzol (Invitrogen) and stored at -80 °C until RNA extraction. RNA
1610 was isolated using the RNeasy Micro Kit (Qiagen) according to the manufacturer's instructions. For cDNA
1611 synthesis, 500 ng of RNA was reverse transcribed using the High-Capacity cDNA Reverse Transcription
1612 Kit (Applied Biosystems). Gene expression was assessed by quantitative PCR (qPCR) using gene-specific
1613 primer pairs (listed in Kay Resources Table). Reactions were performed in 384-well plates using either the
1614 CFX384 Real-Time System (Bio-Rad) or the ABI 7900HT Fast Real-Time PCR System (Applied
1615 Biosystems), with SYBR Green Master Mix (Agilent, Santa Clara, CA). Each well contained 10 ng of cDNA

1616 and 2.5 µM of each primer in a final volume of 10 µL. All reactions were run in technical triplicates.
1617 Cyclophilin B (*Ppib*) was used as the reference gene for normalisation.
1618
1619 **mtDNA Quantification**
1620 Genomic DNA (gDNA) was extracted using the NZY Tissue gDNA Isolation Kit (NZYTech). Relative
1621 mitochondrial DNA (mtDNA) content was determined by qPCR using primers for the following mitochondrial
1622 genes: NADH dehydrogenase 1 (*mt-Nd1*), cytochrome c oxidase subunits 1 and 2 (*mt-Co1* and *mt-Co2*),
1623 and ATP synthase subunit 6 (*mt-Atp6*). Reactions were performed in 384-well plates using the CFX384
1624 Real-Time System (Bio-Rad) with SYBR Green Master Mix (Agilent, Santa Clara, CA). Each well contained
1625 10 ng of gDNA and 2.5 µM of each primer in a final volume of 10 µL. All reactions were run in technical
1626 triplicates. Hexokinase 2 (*HK2*) was used as the reference gene for normalization, with primers listed in the
1627 Kay Resources Table.
1628
1629 **QUANTIFICATION AND STATISTICAL ANALYSIS**
1630 GraphPad software (versions 8.0.1 and 9.5.1) and Microsoft Excel were used for data analysis and plotting.
1631 Results shown are either representative or cumulative from at least two independent experiments. Except
1632 for gene expression analyses during development, RT-qPCR and WB data were normalized to the average
1633 of at least two WT or control mice of their corresponding litter. Sample size, statistical tests, and the meaning
1634 of the dots in each graph are specified in figure legends, except for TEM graphs (Figures 4C, 6F and S6O;
1635 samples sizes indicated in Table S1). In violin plots, median and interquartile range (IQR) are shown; in dot
1636 plots, mean ± SEM; in bar plots with dots, the mean + SEM; and in standard bar plots, the mean + SD.
1637 Outliers were identified using the ROUT method (Q = 5%) or Grubbs' test ($\alpha = 0.05$) for datasets with $n \geq$
1638 6. Normality was assessed using the Shapiro–Wilk test ($n < 50$) or the Kolmogorov–Smirnov test ($n > 50$).
1639 Statistical significance between two groups was determined using Student's t-test for parametric data or
1640 the Mann–Whitney test for nonparametric data. Welch's correction was applied when variances between
1641 groups were unequal. For comparisons among more than two groups, one-way ANOVA or two-way ANOVA
1642 with Tukey's post hoc test was used for parametric data, and the Kruskal–Wallis test, followed by Dunn's
1643 multiple comparison test, was used for nonparametric data. Survival curves were compared using the
1644 Gehan–Breslow–Wilcoxon test. A critical value for significance of $p < 0.05$ was used throughout the study
1645 (*$p < 0.05$, **$p < 0.01$, ***$p < 0.001$, ****$p < 0.0001$). In Figures 1H, 2A, 2H, S5B–C, S6F–H, S7A, S7B, S7E,
1646 and Table S2, only the most relevant statistically significant comparisons are shown; non-significant results
1647 are not displayed. In all other figures, statistical significance is indicated only when differences are
1648 significant.

Figure 1

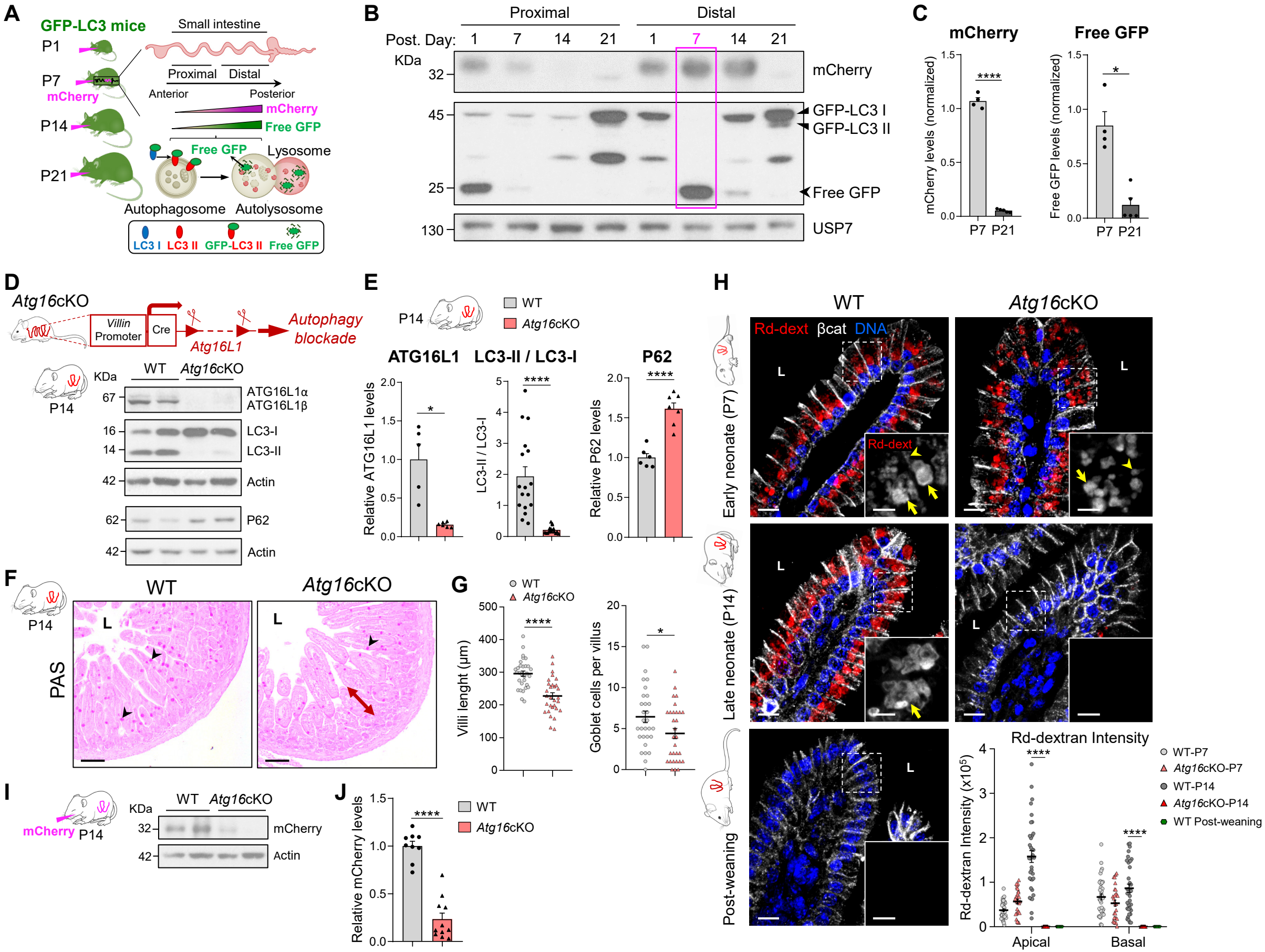
A
GFP-LC3 mice
P1
P7
mCherry
P14
P21
Small intestine
Proximal
Distal
Anterior
Posterior
mCherry
Free GFP
Free GFP
Lysosome
Autophagosome
Autolysosome
LC3 I
LC3 II
GFP-LC3 II
Free GFP
B
Proximal
Distal
Post. Day:
1
7
14
21
1
7
14
21
KDa
32
45
25
130
mCherry
GFP-LC3 I
GFP-LC3 II
Free GFP
USP7
C
mCherry
Free GFP
mCherry levels (normalized)
Free GFP levels (normalized)
****
*
P7
P21
D
Atg16cKO
Villin Promoter
Cre
Atg16L1
Autophagy blockade
P14
WT
Atg16cKO
KDa
67
16
14
42
62
42
ATG16L1α
ATG16L1β
LC3-I
LC3-II
Actin
P62
Actin
E
P14
WT
Atg16cKO
ATG16L1
LC3-II / LC3-I
P62
Relative ATG16L1 levels
LC3-II / LC3-I
Relative P62 levels
*
****
****
F
WT
Atg16cKO
P14
PAS
L
L
G
WT
Atg16cKO
Villi lenght (µm)
Goblet cells per villus
****
*
H
WT
Atg16cKO
Rd-dext
βcat
DNA
Early neonate (P7)
Late neonate (P14)
Post-weaning
L
Rd-dext
Rd-dextran Intensity
Rd-dextran Intensity (x10^5)
WT-P7
Atg16cKO-P7
WT-P14
Atg16cKO-P14
WT Post-weaning
****
****
Apical
Basal
I
mCherry
P14
KDa
WT
Atg16cKO
32
42
mCherry
Actin
J
Relative mCherry levels
WT
Atg16cKO
****

Figure 2

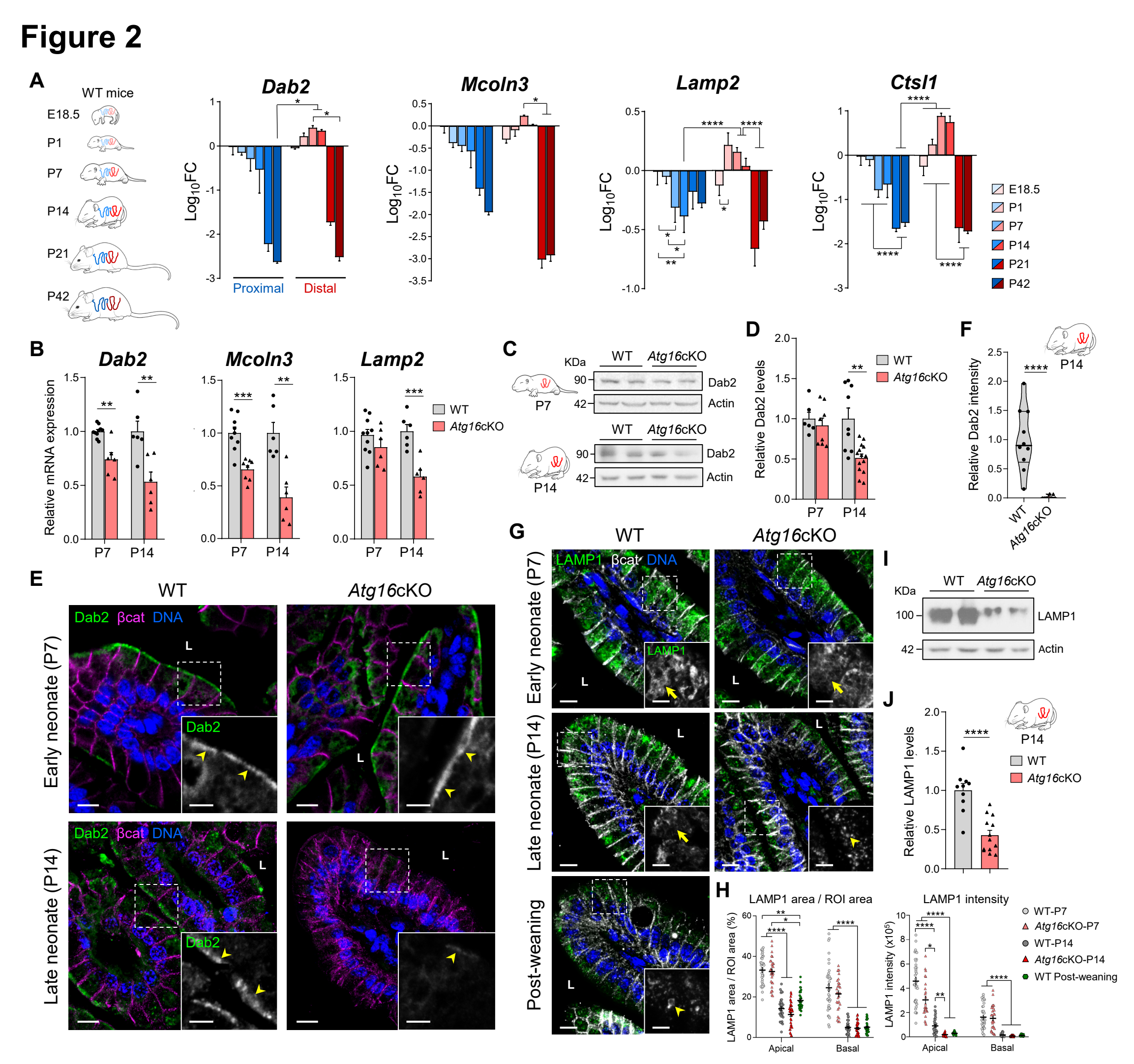
A
WT mice
E18.5
P1
P7
P14
P21
P42
Dab2
Mcoln3
Lamp2
Ctsl1
Log10FC
Proximal
Distal
E18.5
P1
P7
P14
P21
P42
B
Relative mRNA expression
WT
Atg16cKO
C
KDa
WT
Atg16cKO
90
42
Dab2
Actin
P7
P14
D
Relative Dab2 levels
F
Relative Dab2 intensity
WT
Atg16cKO
E
Dab2 βcat DNA
L
Early neonate (P7)
Late neonate (P14)
G
LAMP1 βcat DNA
LAMP1
Post-weaning
I
100
LAMP1
J
Relative LAMP1 levels
H
LAMP1 area / ROI area
LAMP1 intensity
LAMP1 intensity (x10^5)
Apical
Basal
WT-P7
Atg16cKO-P7
WT-P14
Atg16cKO-P14
WT Post-weaning

Figure 3

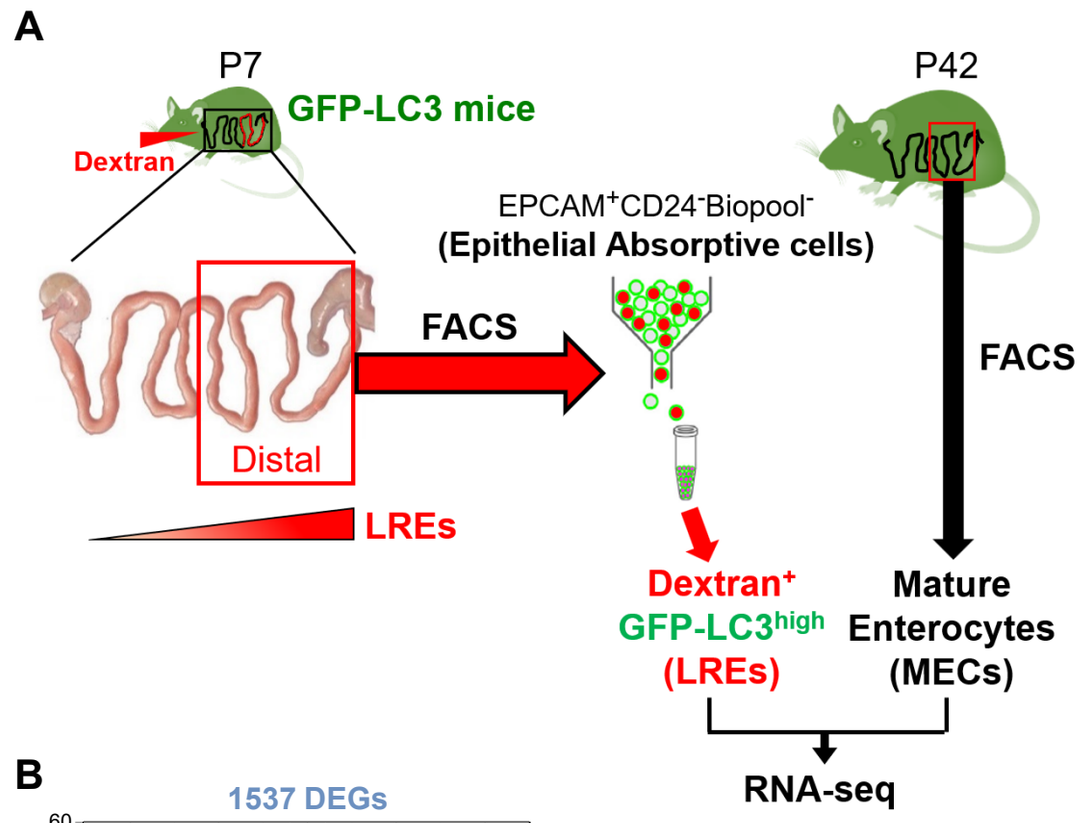
A
P7
GFP-LC3 mice
Dextran
Distal
LREs
EPCAM+CD24-Biopool-
(Epithelial Absorptive cells)
FACS
P42
FACS
Dextran+
GFP-LC3high
(LREs)
Mature
Enterocytes
(MECs)
RNA-seq

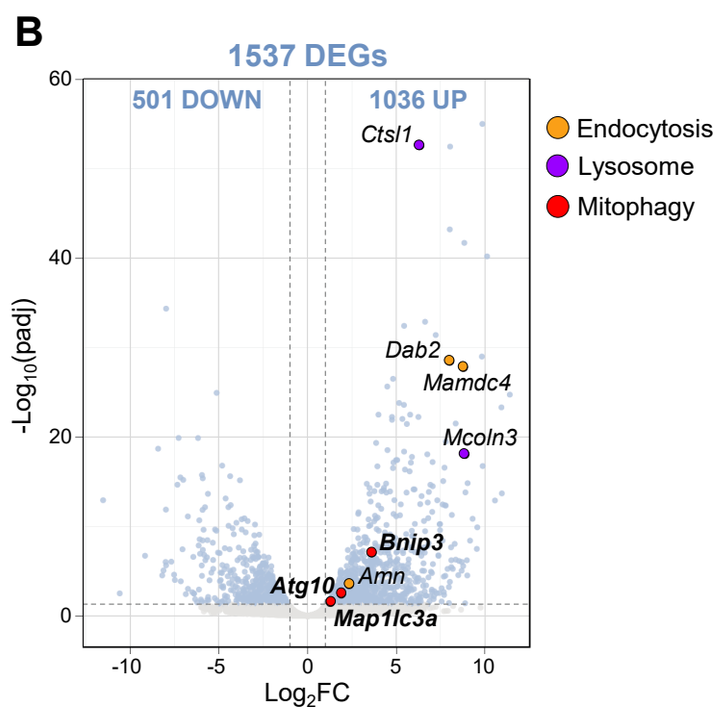
B
1537 DEGs
501 DOWN
1036 UP
Ctsl1
Dab2
Mamdc4
Mcoln3
Bnip3
Amn
Atg10
Map1lc3a
Endocytosis
Lysosome
Mitophagy
-Log10(padj)
Log2FC

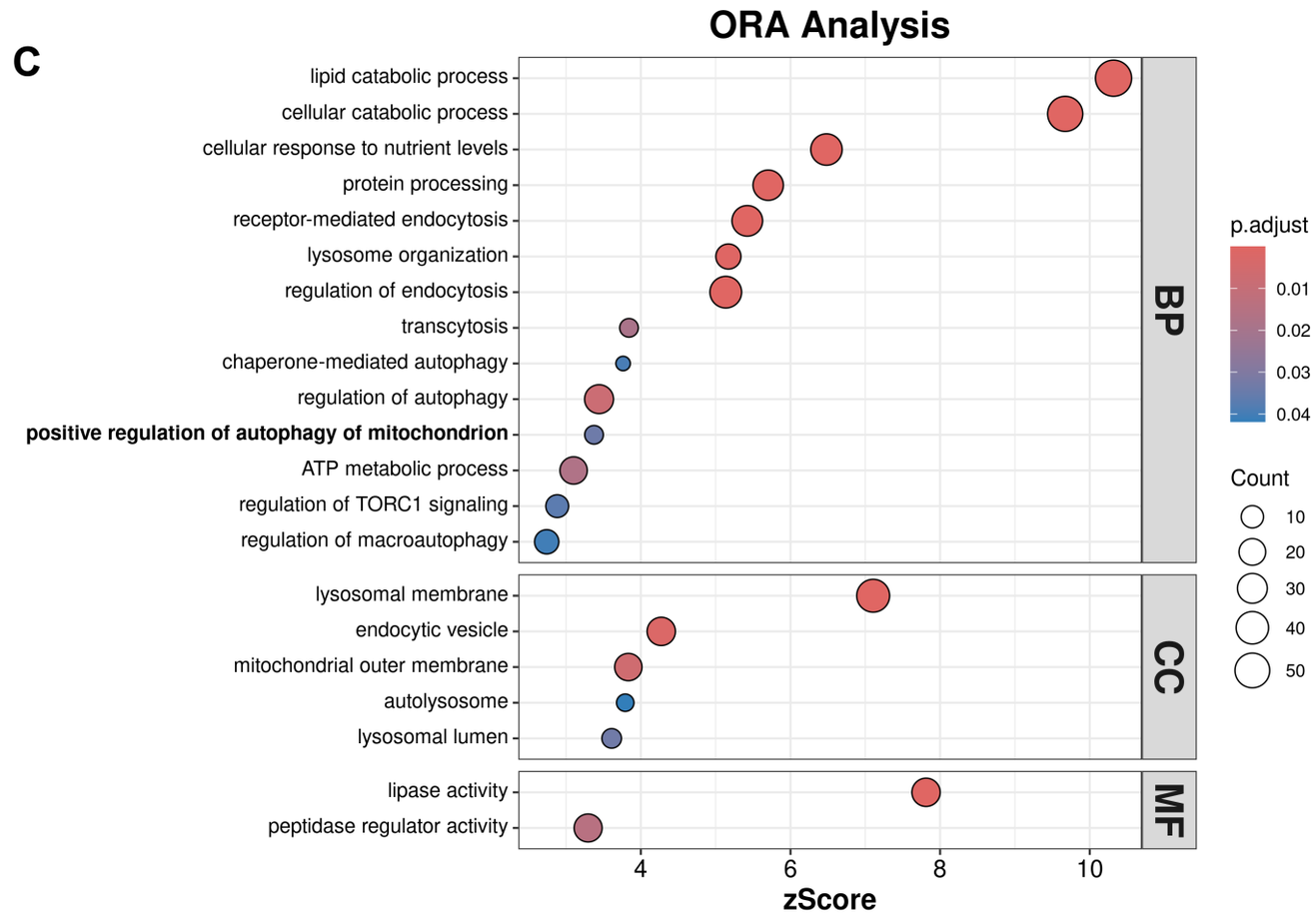
C
ORA Analysis
lipid catabolic process
cellular catabolic process
cellular response to nutrient levels
protein processing
receptor-mediated endocytosis
lysosome organization
regulation of endocytosis
transcytosis
chaperone-mediated autophagy
regulation of autophagy
positive regulation of autophagy of mitochondrion
ATP metabolic process
regulation of TORC1 signaling
regulation of macroautophagy
lysosomal membrane
endocytic vesicle
mitochondrial outer membrane
autolysosome
lysosomal lumen
lipase activity
peptidase regulator activity
BP
CC
MF
zScore
p.adjust
Count

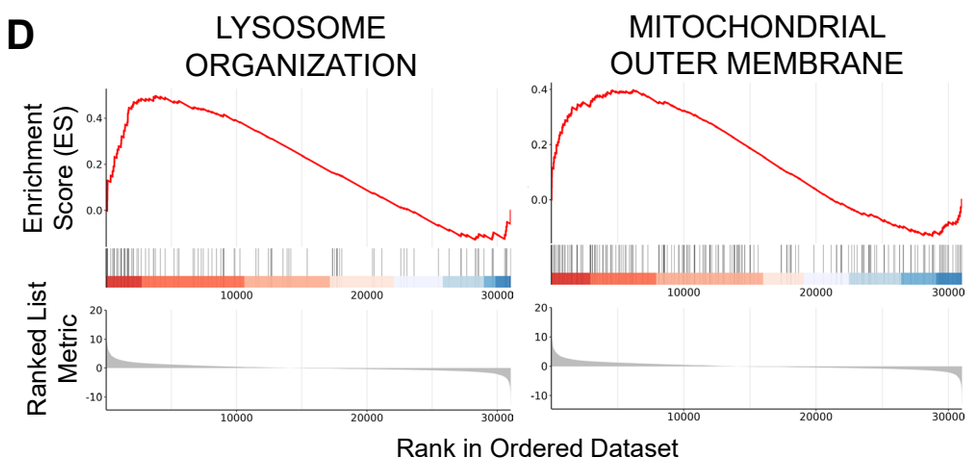
D
LYSOSOME ORGANIZATION
MITOCHONDRIAL OUTER MEMBRANE
Enrichment Score (ES)
Ranked List Metric
Rank in Ordered Dataset

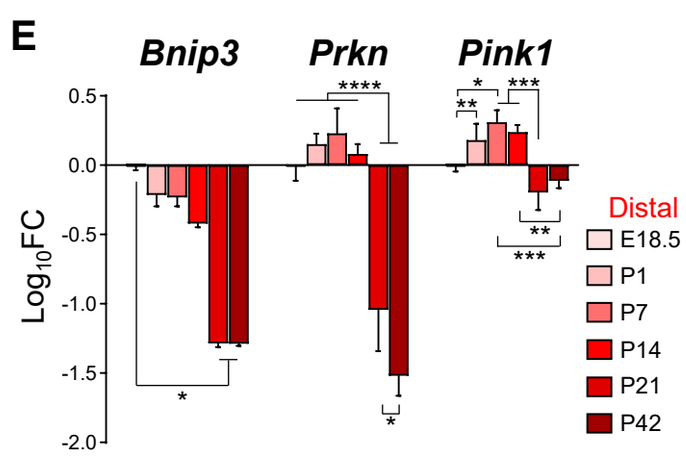
E
Bnip3
Prkn
Pink1
Log10FC
Distal
E18.5
P1
P7
P14
P21
P42

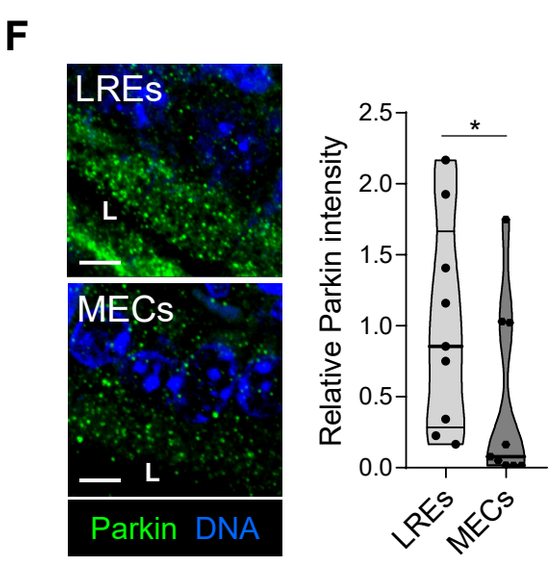
F
LREs
MECs
Parkin DNA
Relative Parkin intensity
LREs
MECs

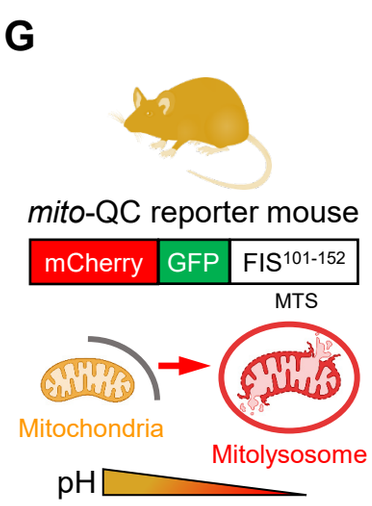
G
mito-QC reporter mouse
mCherry
GFP
FIS101-152
MTS
Mitochondria
Mitolysosome
pH

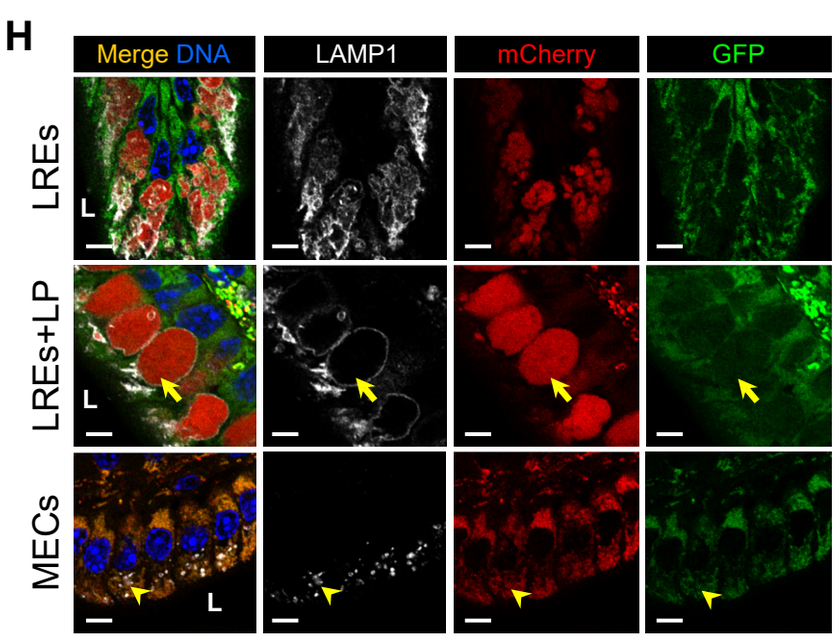
H
Merge DNA
LAMP1
mCherry
GFP
LREs
LREs+LP
MECs

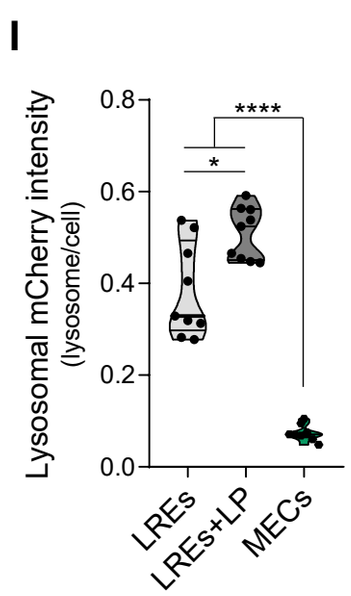
I
Lysosomal mCherry intensity
(lysosome/cell)
LREs
LREs+LP
MECs

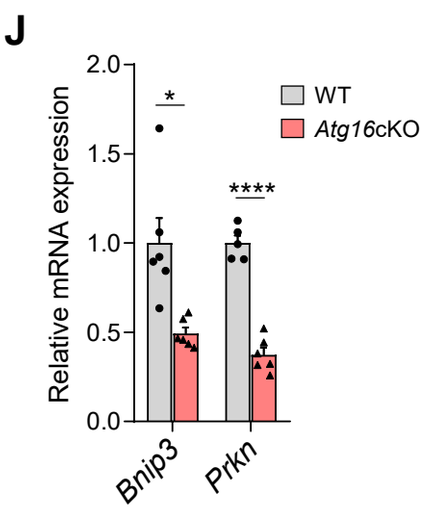
J
Relative mRNA expression
WT
Atg16cKO
Bnip3
Prkn

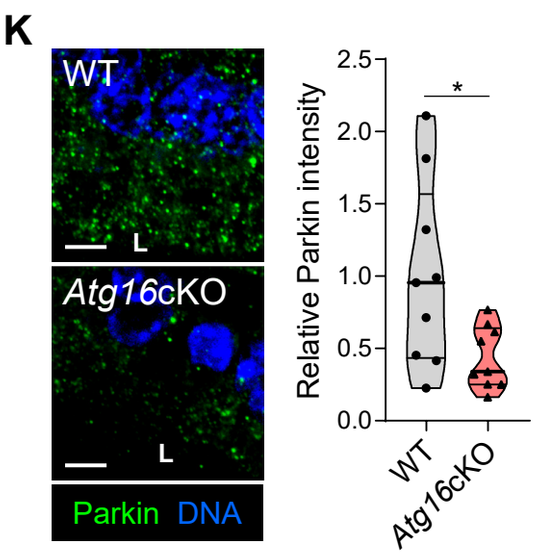
K
WT
Atg16cKO
Parkin DNA
Relative Parkin intensity
WT
Atg16cKO

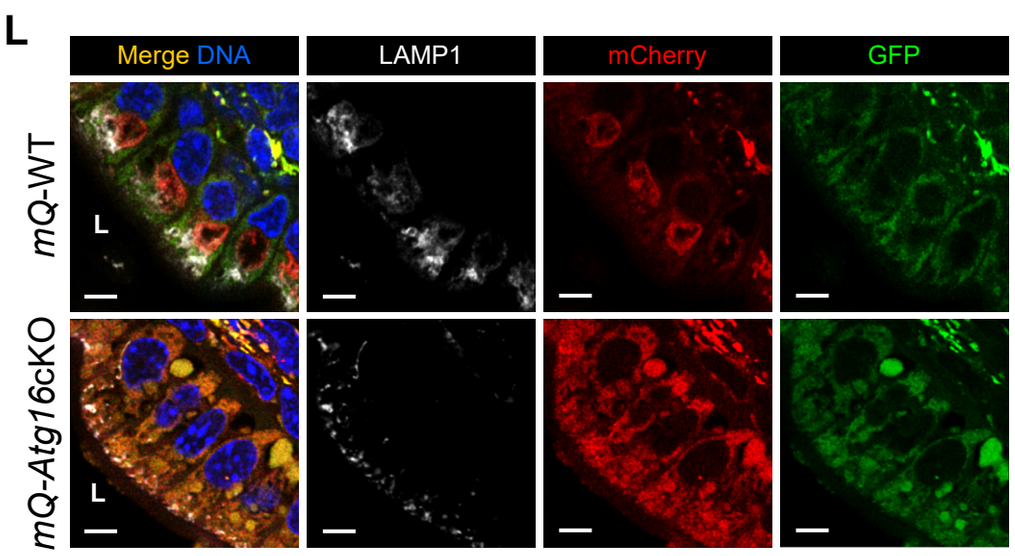
L
Merge DNA
LAMP1
mCherry
GFP
mQ-WT
mQ-Atg16cKO

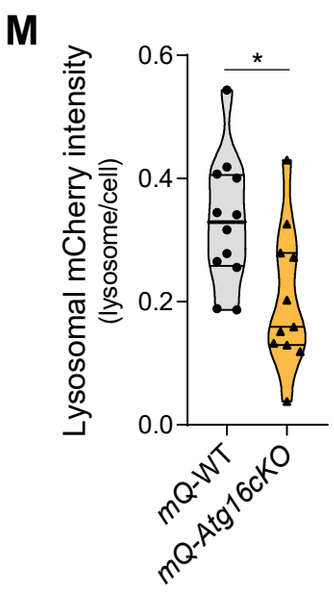
M
Lysosomal mCherry intensity
(lysosome/cell)
mQ-WT
mQ-Atg16cKO

Figure 4

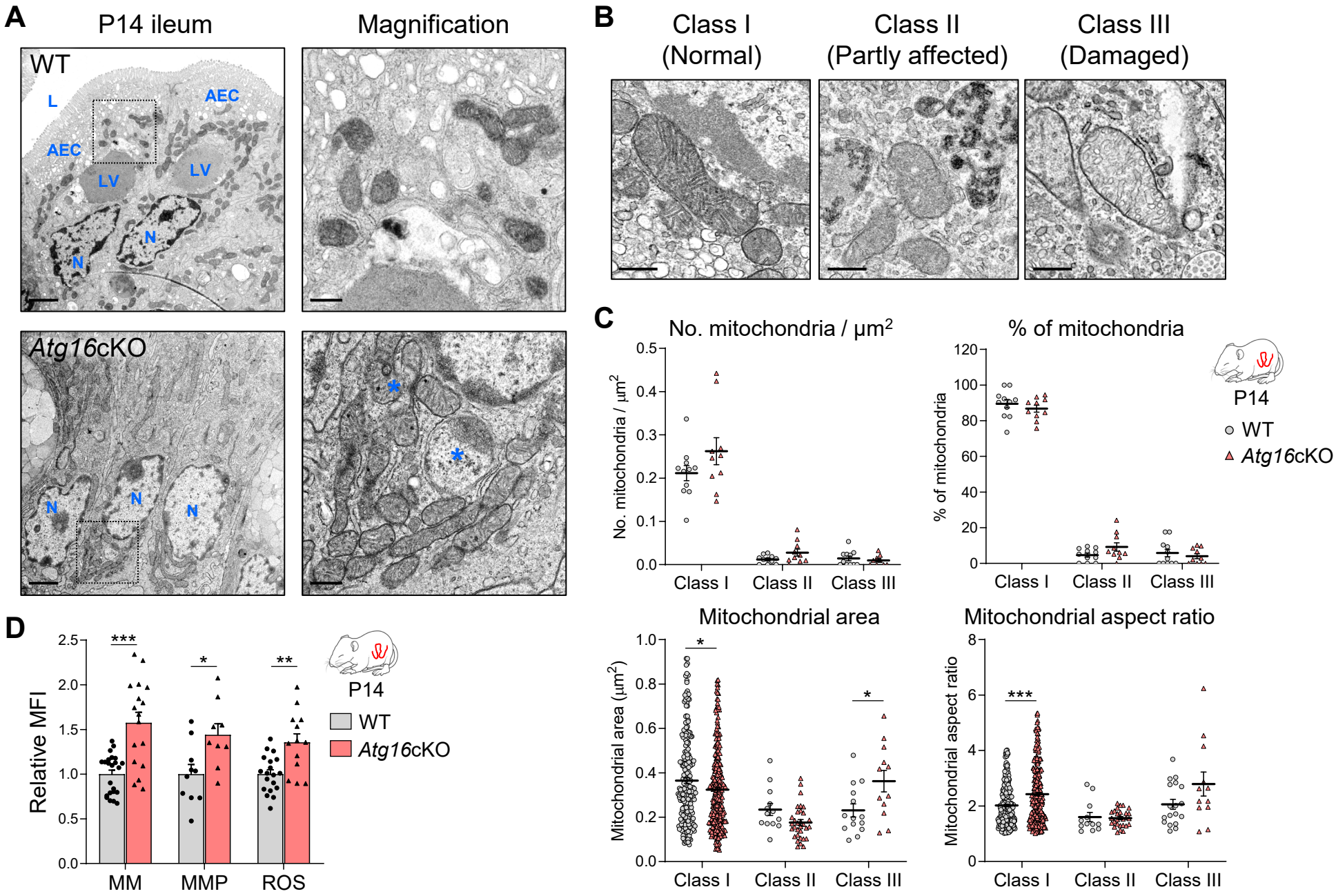
A
P14 ileum
Magnification
WT
L
AEC
AEC
LV
LV
N
N
Atg16cKO
N
N
N
B
Class I
(Normal)
Class II
(Partly affected)
Class III
(Damaged)
C
No. mitochondria / μm²
No. mitochondria / μm²
Class I
Class II
Class III
% of mitochondria
% of mitochondria
P14
WT
Atg16cKO
Mitochondrial area
Mitochondrial area (μm²)
Mitochondrial aspect ratio
Mitochondrial aspect ratio
D
Relative MFI
MM
MMP
ROS
P14
WT
Atg16cKO

Figure 5

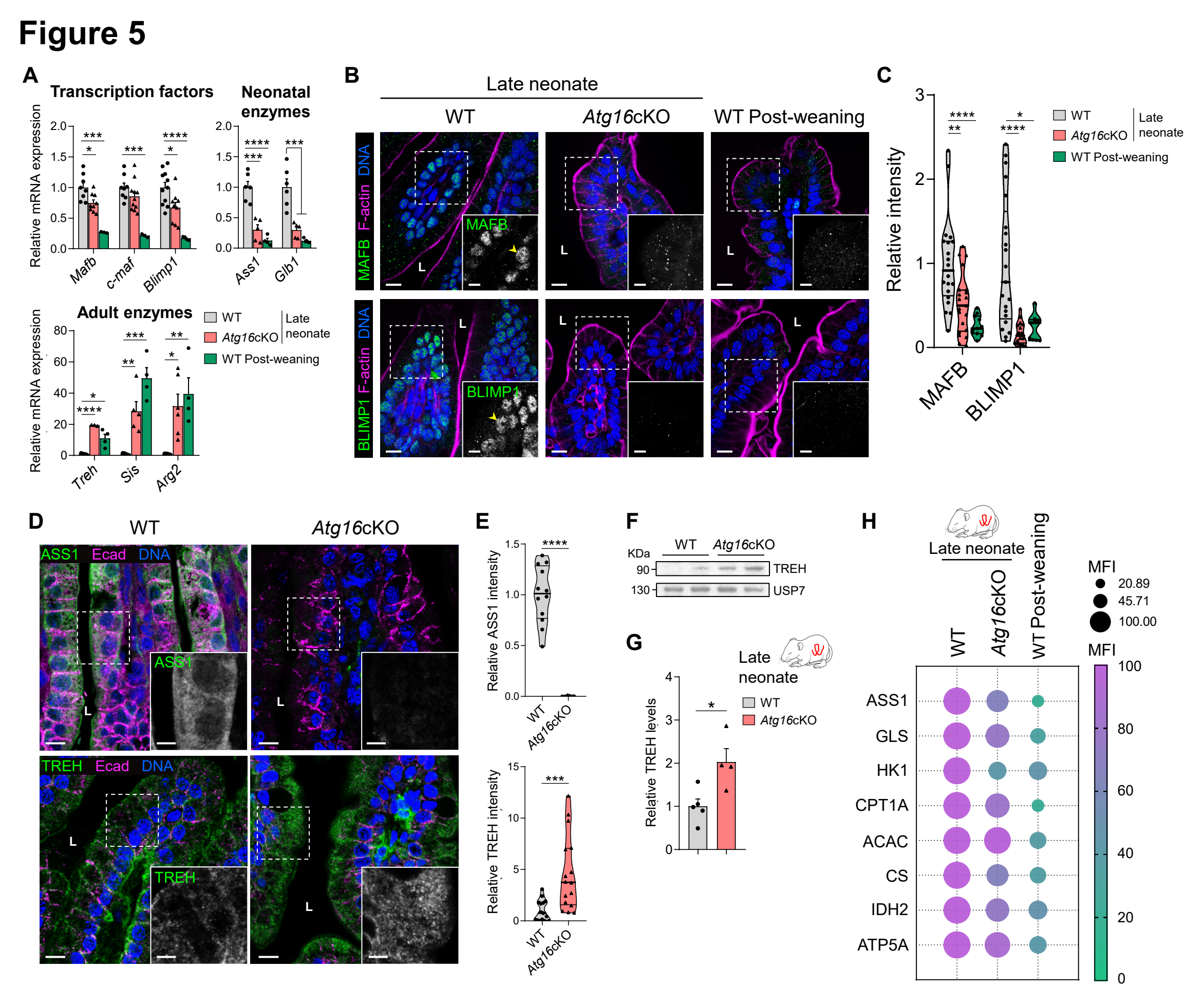
A
Transcription factors
Neonatal enzymes
Relative mRNA expression
Mafb
c-maf
Blimp1
Ass1
Glb1
Adult enzymes
Treh
Sis
Arg2
WT
Atg16cKO
WT Post-weaning
Late neonate
B
Late neonate
WT
Atg16cKO
WT Post-weaning
MAFB F-actin DNA
BLIMP1 F-actin DNA
MAFB
BLIMP1
L
C
Relative intensity
MAFB
BLIMP1
D
WT
Atg16cKO
ASS1 Ecad DNA
TREH Ecad DNA
ASS1
TREH
E
Relative ASS1 intensity
Relative TREH intensity
F
KDa
WT
Atg16cKO
90
130
TREH
USP7
G
Late neonate
Relative TREH levels
H
Late neonate
WT
Atg16cKO
WT Post-weaning
MFI
20.89
45.71
100.00
ASS1
GLS
HK1
CPT1A
ACAC
CS
IDH2
ATP5A

Figure 6

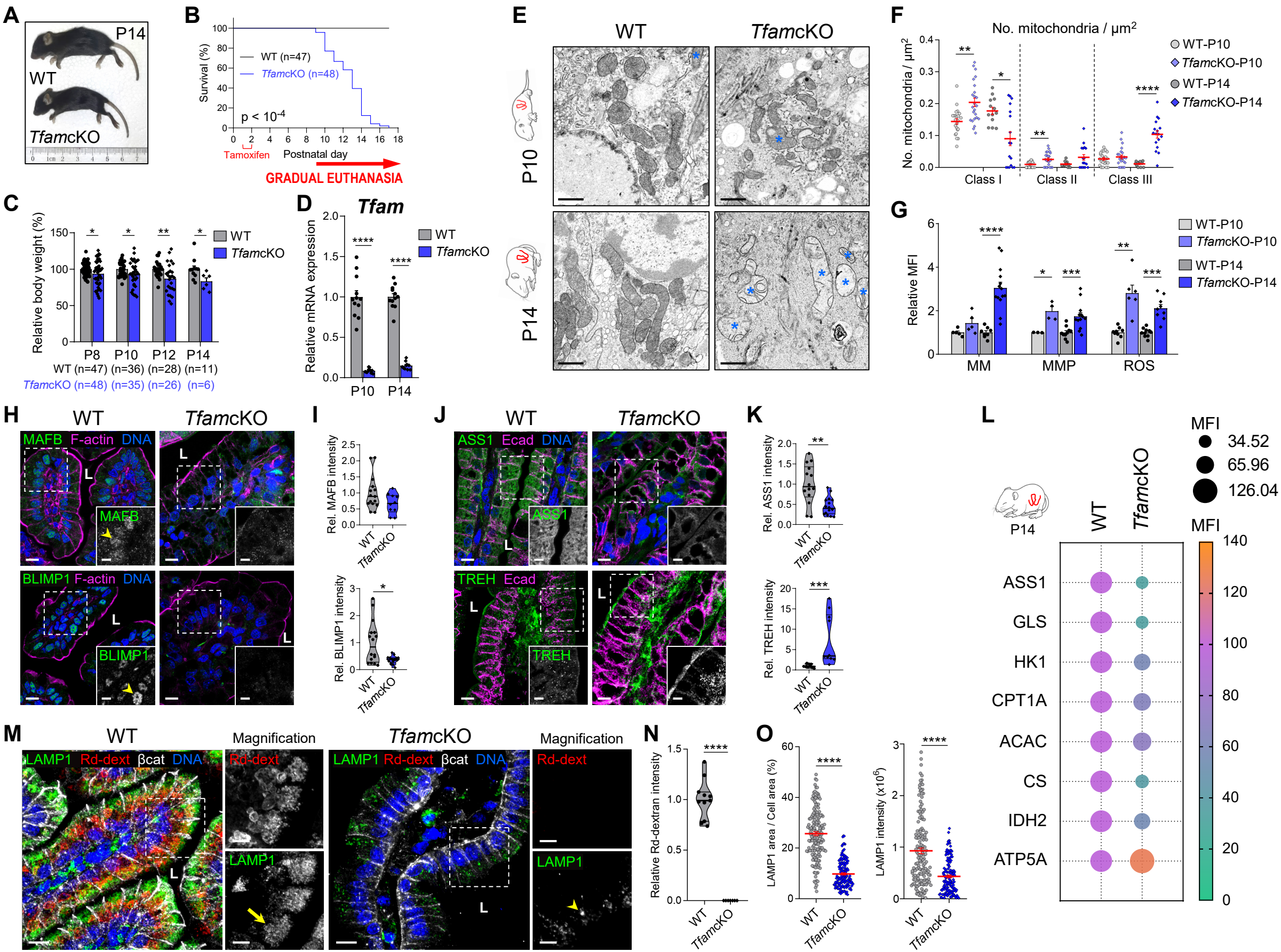
A
P14
WT
TfamcKO
B
Survival (%)
WT (n=47)
TfamcKO (n=48)
p < 10-4
Tamoxifen
Postnatal day
GRADUAL EUTHANASIA
C
Relative body weight (%)
WT
TfamcKO
P8 P10 P12 P14
WT (n=47) (n=36) (n=28) (n=11)
TfamcKO (n=48) (n=35) (n=26) (n=6)
D
Tfam
Relative mRNA expression
P10 P14
E
WT
TfamcKO
P10
P14
F
No. mitochondria / µm2
WT-P10
TfamcKO-P10
WT-P14
TfamcKO-P14
Class I
Class II
Class III
G
Relative MFI
MM
MMP
ROS
H
WT
TfamcKO
MAFB F-actin DNA
MAFB
BLIMP1 F-actin DNA
BLIMP1
Rel. MAFB intensity
Rel. BLIMP1 intensity
I
J
ASS1 Ecad DNA
ASS1
TREH Ecad
TREH
K
Rel. ASS1 intensity
Rel. TREH intensity
L
MFI
34.52
65.96
126.04
P14
ASS1
GLS
HK1
CPT1A
ACAC
CS
IDH2
ATP5A
M
WT
TfamcKO
Magnification
LAMP1 Rd-dext βcat DNA
Rd-dext
LAMP1
N
Relative Rd-dextran intensity
O
LAMP1 area / Cell area (%)
LAMP1 intensity (x10^6)

Figure 7

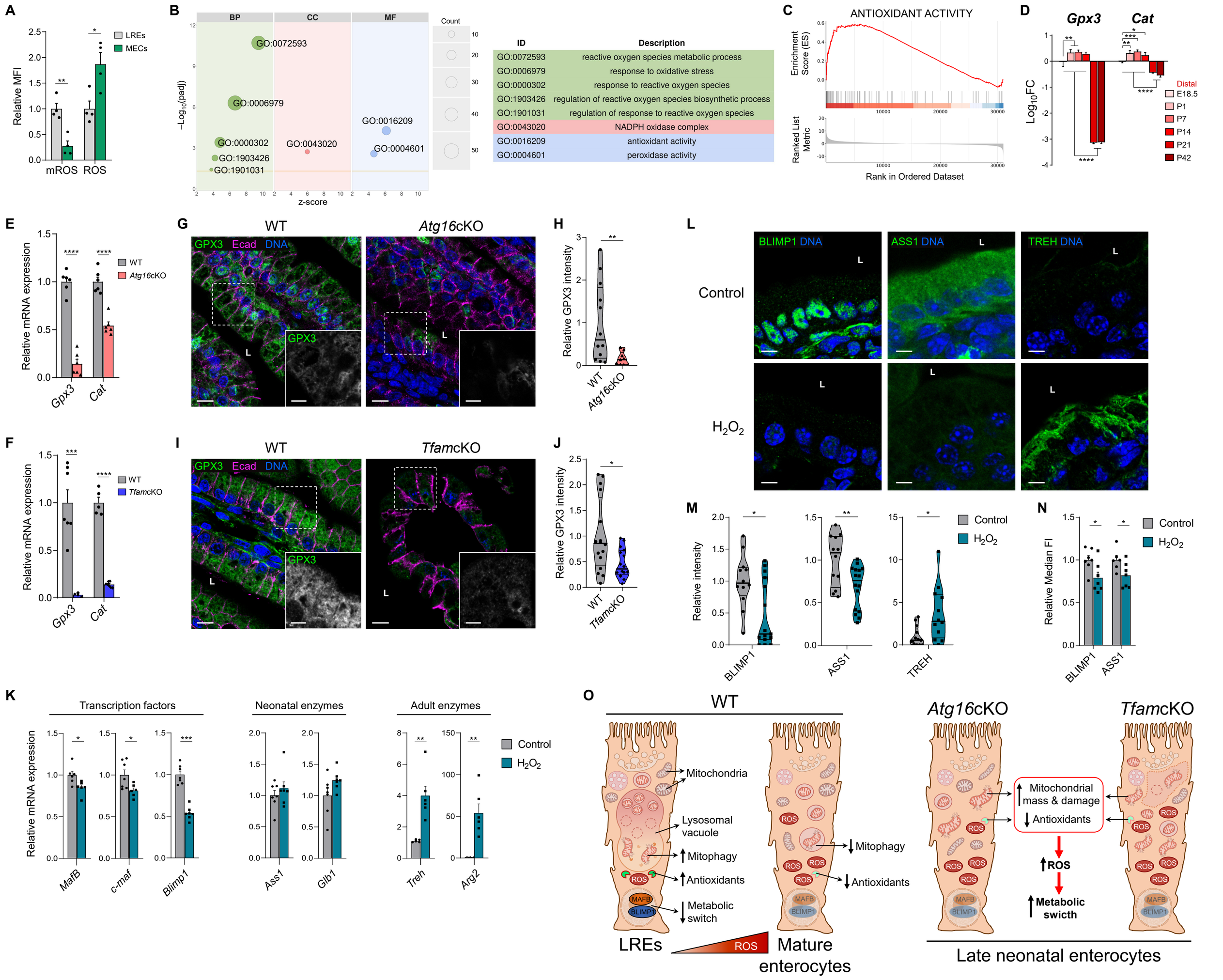
A
Relative MFI
LREs
MECs
mROS
ROS
B
BP
CC
MF
Count
GO:0072593
GO:0006979
GO:0000302
GO:1903426
GO:1901031
GO:0043020
GO:0016209
GO:0004601
z-score
ID
Description
GO:0072593 reactive oxygen species metabolic process
GO:0006979 response to oxidative stress
GO:0000302 response to reactive oxygen species
GO:1903426 regulation of reactive oxygen species biosynthetic process
GO:1901031 regulation of response to reactive oxygen species
GO:0043020 NADPH oxidase complex
GO:0016209 antioxidant activity
GO:0004601 peroxidase activity
C
ANTIOXIDANT ACTIVITY
Enrichment Score (ES)
Ranked List Metric
Rank in Ordered Dataset
D
Gpx3
Cat
Log10FC
Distal
E18.5
P1
P7
P14
P21
P42
E
Relative mRNA expression
WT
Atg16cKO
Gpx3
Cat
F
Relative mRNA expression
WT
TfamcKO
Gpx3
Cat
G
WT
Atg16cKO
GPX3 Ecad DNA
GPX3
L
H
Relative GPX3 intensity
WT
Atg16cKO
I
WT
TfamcKO
GPX3 Ecad DNA
GPX3
L
J
Relative GPX3 intensity
WT
TfamcKO
K
Transcription factors
Neonatal enzymes
Adult enzymes
Relative mRNA expression
Control
H2O2
MafB
c-maf
Blimp1
Ass1
Glb1
Treh
Arg2
L
BLIMP1 DNA
ASS1 DNA
TREH DNA
Control
H2O2
M
Relative intensity
Control
H2O2
BLIMP1
ASS1
TREH
N
Relative Median FI
Control
H2O2
BLIMP1
ASS1
O
WT
Mitochondria
Lysosomal vacuole
Mitophagy
Antioxidants
Metabolic switch
ROS
MAFB
BLIMP1
LREs
Mature enterocytes
Atg16cKO
TfamcKO
Mitochondrial mass & damage
Antioxidants
ROS
Metabolic switch
Late neonatal enterocytes

Figure S1

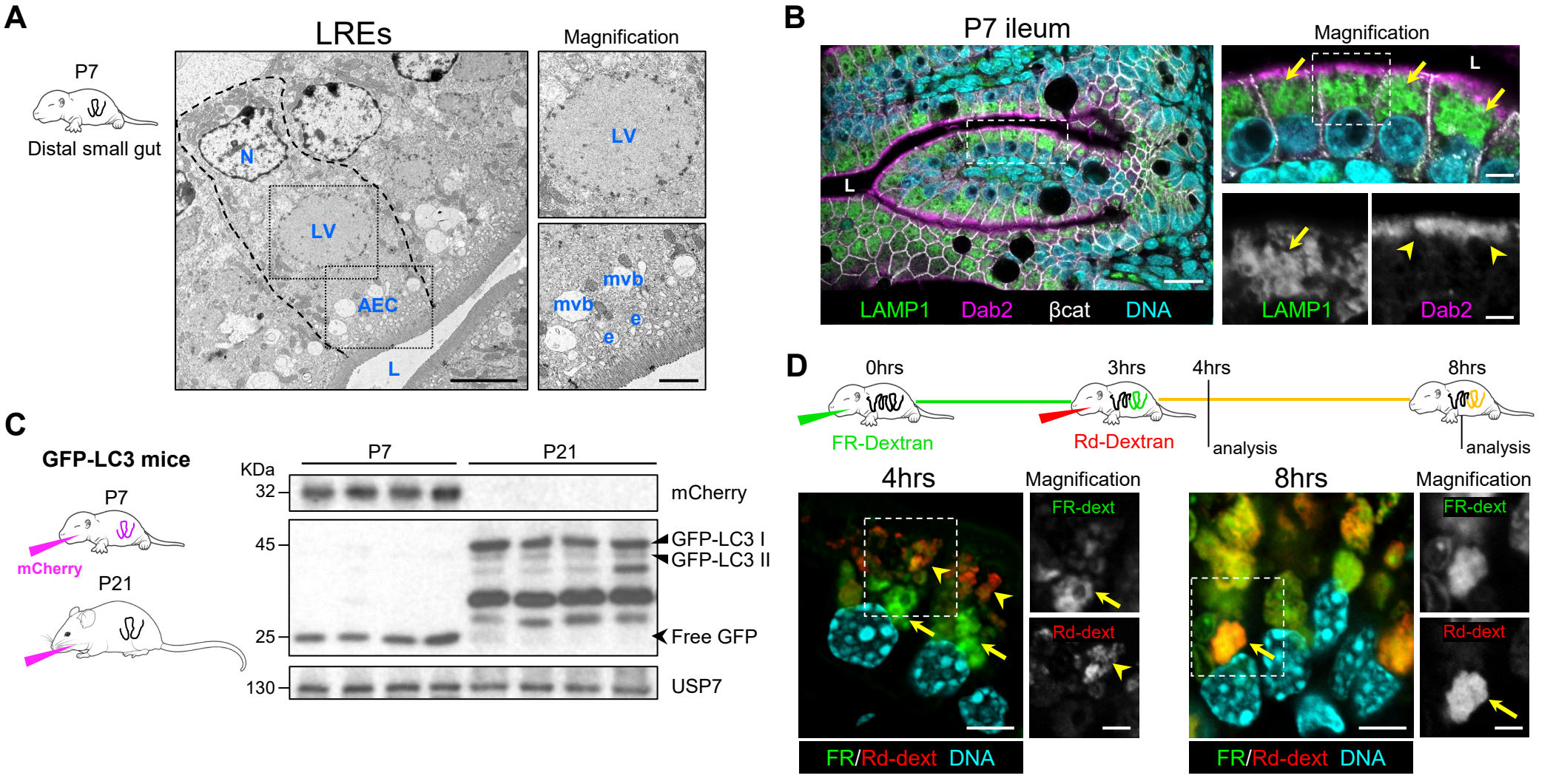
A
P7
Distal small gut
LREs
Magnification
N
LV
AEC
L
LV
mvb
mvb
e
e
B
P7 ileum
Magnification
L
L
LAMP1
Dab2
βcat
DNA
LAMP1
Dab2
C
GFP-LC3 mice
P7
mCherry
P21
KDa
P7
P21
32
45
25
130
mCherry
GFP-LC3 I
GFP-LC3 II
Free GFP
USP7
D
0hrs
3hrs
4hrs
8hrs
FR-Dextran
Rd-Dextran
analysis
analysis
4hrs
Magnification
8hrs
Magnification
FR-dext
Rd-dext
FR-dext
Rd-dext
FR/Rd-dext DNA
FR/Rd-dext DNA

Figure S2

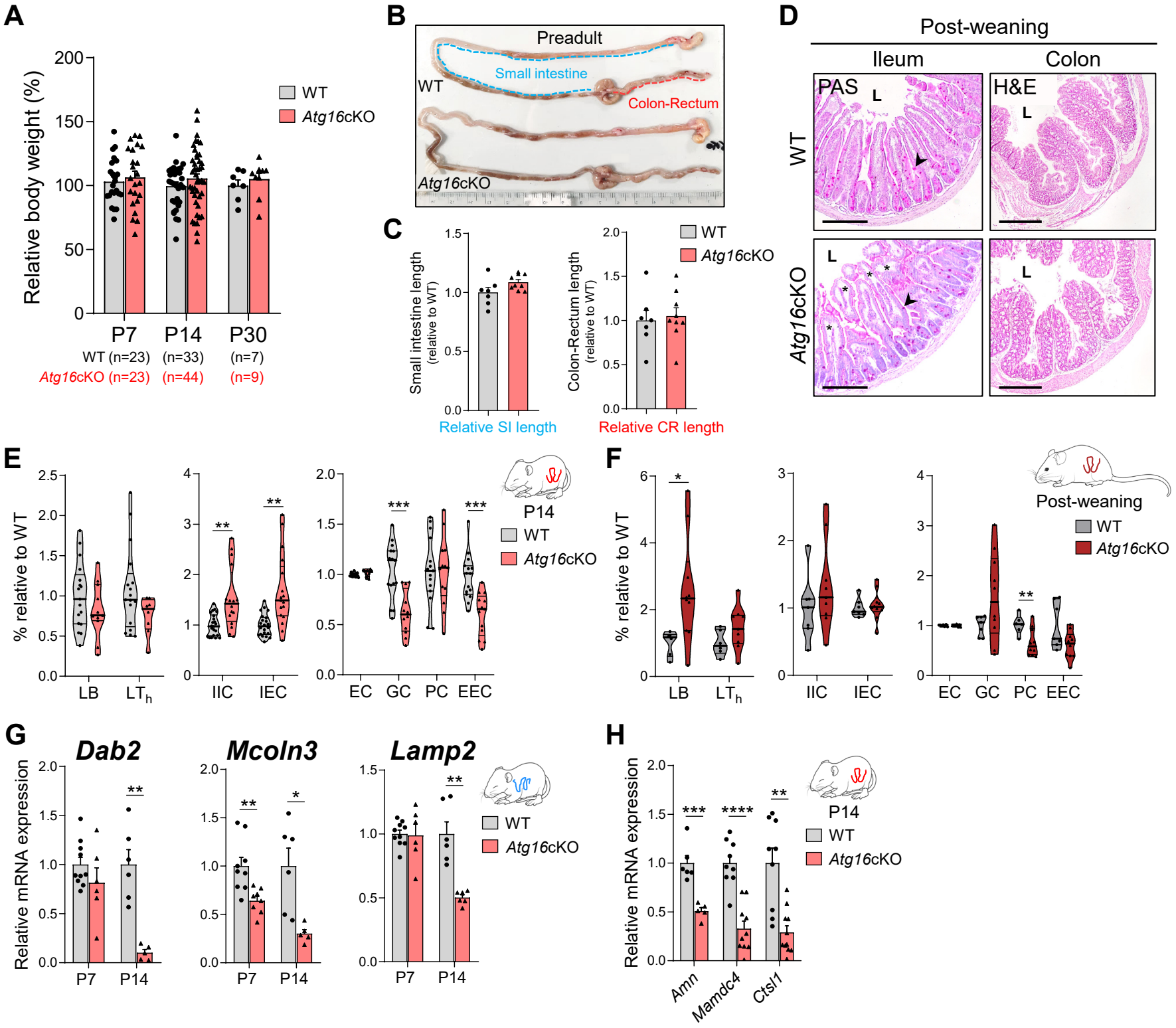
A
Relative body weight (%)
WT
Atg16cKO
P7
P14
P30
WT (n=23) (n=33) (n=7)
Atg16cKO (n=23) (n=44) (n=9)
B
Preadult
Small intestine
Colon-Rectum
WT
Atg16cKO
C
Small intestine length (relative to WT)
Colon-Rectum length (relative to WT)
Relative SI length
Relative CR length
D
Post-weaning
Ileum
Colon
PAS
H&E
L
E
% relative to WT
LB
LTh
IIC
IEC
EC
GC
PC
EEC
P14
F
Post-weaning
G
Dab2
Mcoln3
Lamp2
Relative mRNA expression
H
Amn
Mamdc4
Ctsl1

Figure S3

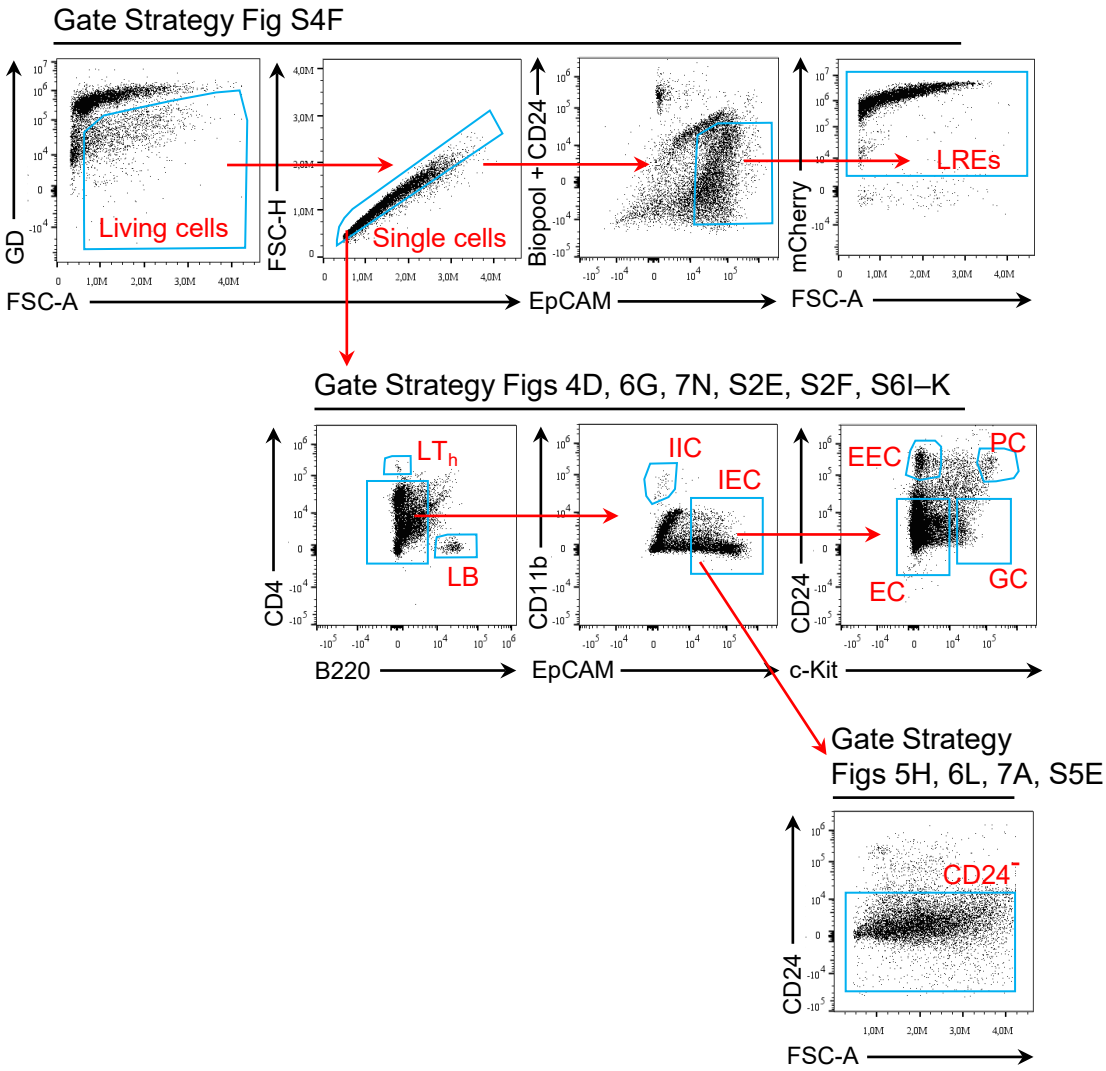
Gate Strategy Fig S4F
Living cells
Single cells
LREs
GD
FSC-A
FSC-H
Biopool + CD24
EpCAM
mCherry
FSC-A
Gate Strategy Figs 4D, 6G, 7N, S2E, S2F, S6I–K
LTh
LB
IIC
IEC
EEC
PC
EC
GC
CD4
B220
CD11b
EpCAM
CD24
c-Kit
Gate Strategy
Figs 5H, 6L, 7A, S5E
CD24-
CD24
FSC-A

Figure S4

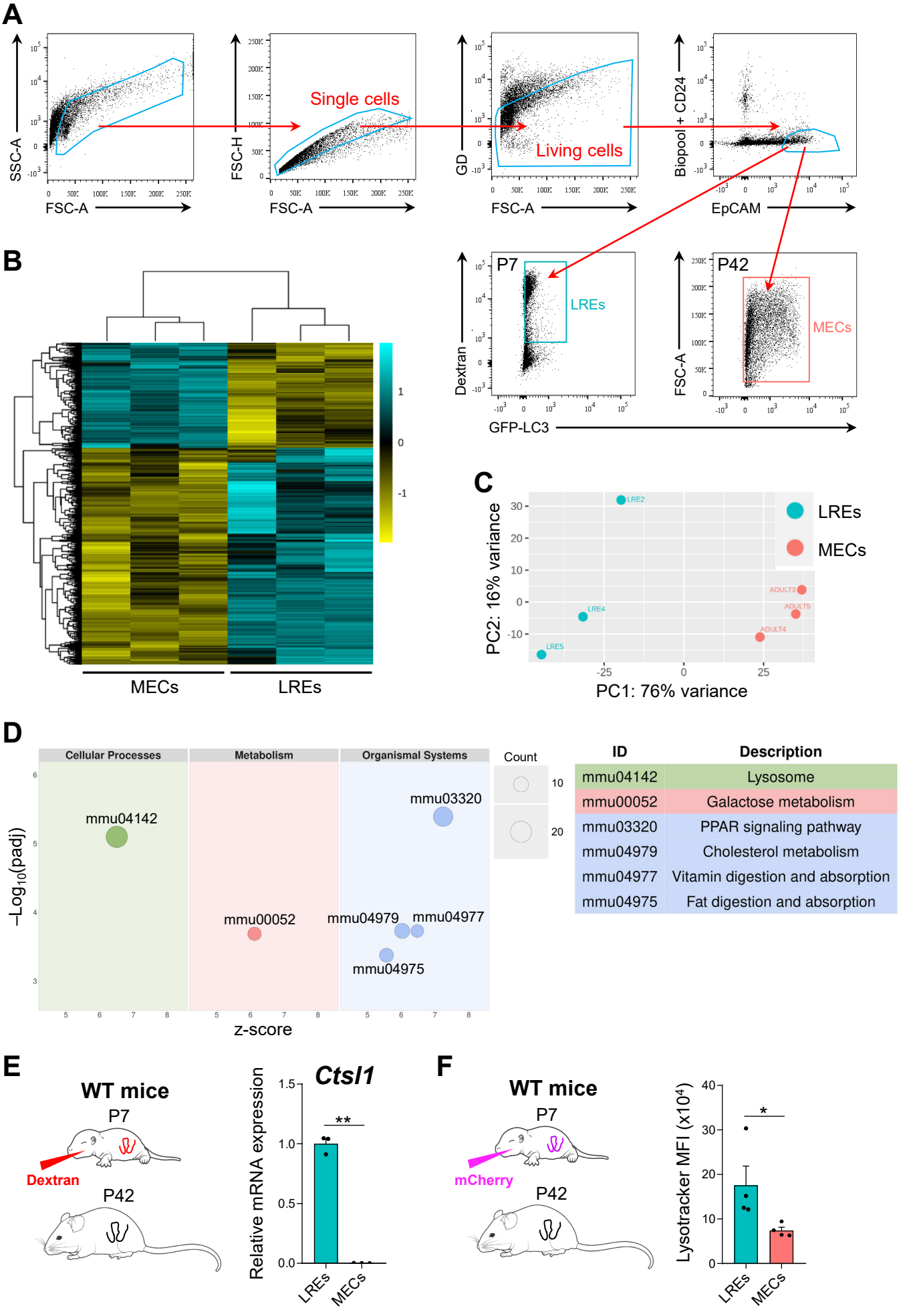
A
SSC-A
FSC-A
FSC-H
Single cells
GD
Living cells
Biopool + CD24
EpCAM
P7
LREs
P42
MECs
Dextran
FSC-A
GFP-LC3
B
1
0
-1
MECs
LREs
C
LREs
MECs
PC2: 16% variance
PC1: 76% variance
LRE2
LRE4
LRE5
ADULT3
ADULT5
ADULT4
D
Cellular Processes
Metabolism
Organismal Systems
Count
10
20
mmu04142
mmu03320
mmu00052
mmu04979
mmu04977
mmu04975
–Log10(padj)
z-score
ID
Description
mmu04142 Lysosome
mmu00052 Galactose metabolism
mmu03320 PPAR signaling pathway
mmu04979 Cholesterol metabolism
mmu04977 Vitamin digestion and absorption
mmu04975 Fat digestion and absorption
E
WT mice
P7
Dextran
P42
Ctsl1
Relative mRNA expression
**
LREs
MECs
F
WT mice
P7
mCherry
P42
Lysotracker MFI (x10⁴)
*
LREs
MECs

Figure S5

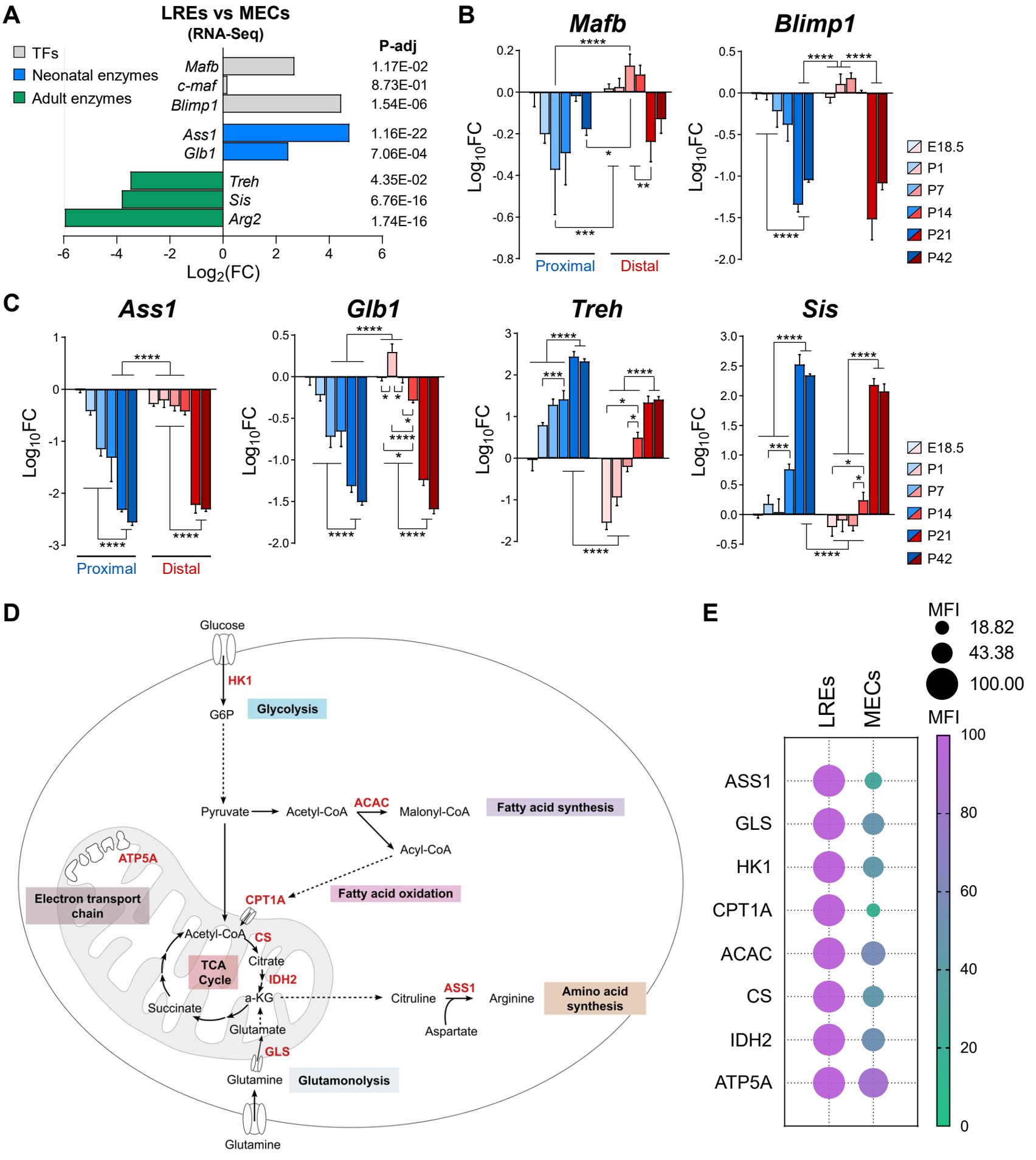
A
LREs vs MECs
(RNA-Seq)
TFs
Neonatal enzymes
Adult enzymes
P-adj
Mafb 1.17E-02
c-maf 8.73E-01
Blimp1 1.54E-06
Ass1 1.16E-22
Glb1 7.06E-04
Treh 4.35E-02
Sis 6.76E-16
Arg2 1.74E-16
Log2(FC)
B
Mafb
Blimp1
Log10FC
Proximal
Distal
E18.5
P1
P7
P14
P21
P42
C
Ass1
Glb1
Treh
Sis
D
Glucose
HK1
G6P
Glycolysis
Pyruvate
Acetyl-CoA
ACAC
Malonyl-CoA
Fatty acid synthesis
Acyl-CoA
ATP5A
Electron transport chain
CPT1A
Fatty acid oxidation
Acetyl-CoA
CS
Citrate
TCA Cycle
IDH2
a-KG
Succinate
Citruline
ASS1
Arginine
Amino acid synthesis
Aspartate
Glutamate
GLS
Glutamine
Glutamonolysis
Glutamine
E
MFI
18.82
43.38
100.00
LREs
MECs
ASS1
GLS
HK1
CPT1A
ACAC
CS
IDH2
ATP5A
100
80
60
40
20
0

Figure S6

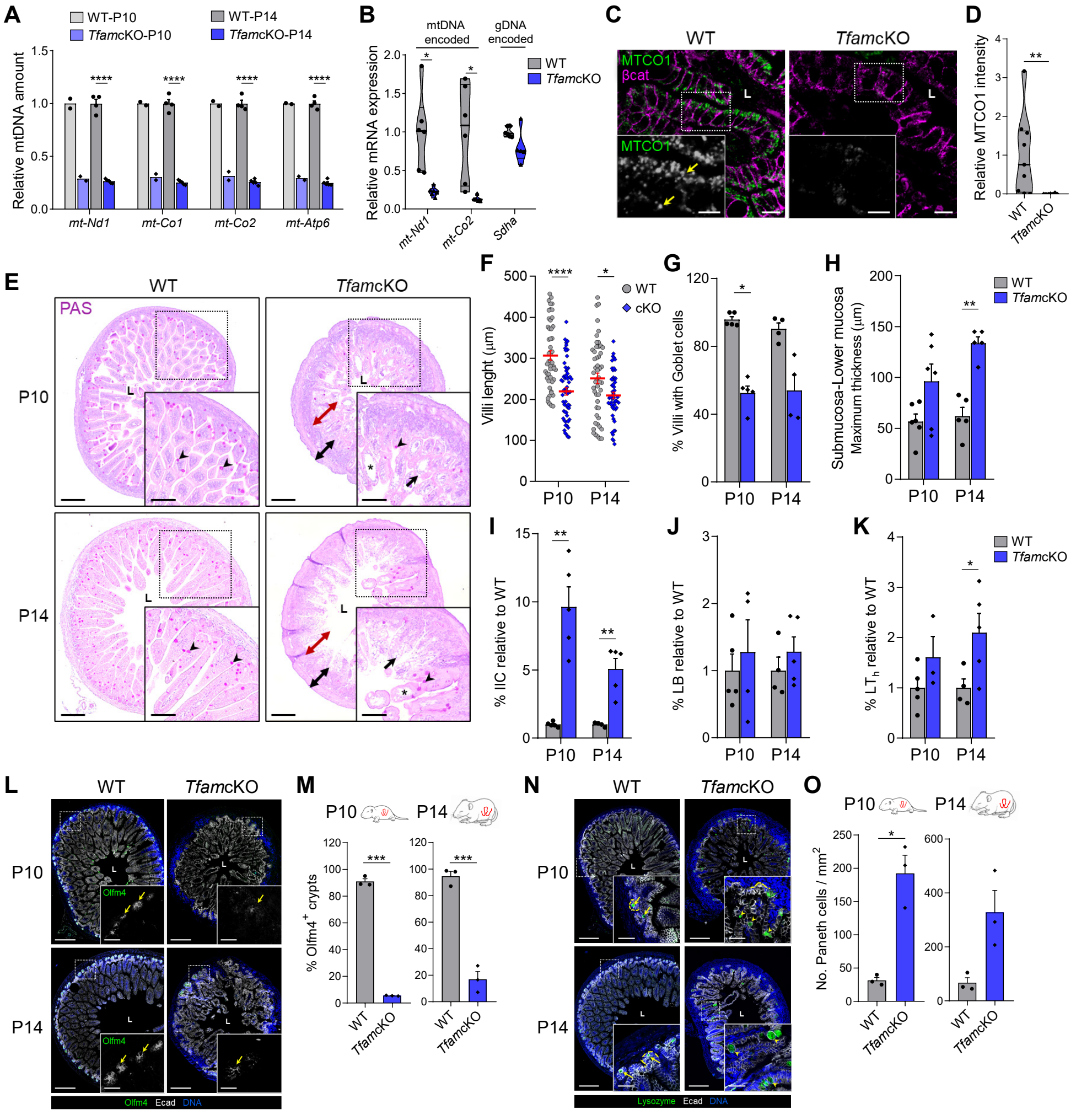
A
WT-P10
TfamcKO-P10
WT-P14
TfamcKO-P14
Relative mtDNA amount
mt-Nd1
mt-Co1
mt-Co2
mt-Atp6
B
mtDNA encoded
gDNA encoded
Relative mRNA expression
WT
TfamcKO
mt-Nd1
mt-Co2
Sdha
C
WT
TfamcKO
MTCO1
βcat
L
D
Relative MTCO1 intensity
E
WT
TfamcKO
PAS
P10
P14
F
Villi lenght (µm)
WT
cKO
G
% Villi with Goblet cells
H
Submucosa-Lower mucosa Maximum thickness (µm)
I
% IIC relative to WT
J
% LB relative to WT
K
% LTh relative to WT
L
Olfm4
Olfm4 Ecad DNA
M
% Olfm4+ crypts
N
Lysozyme Ecad DNA
O
No. Paneth cells / mm2
P
% of mitochondria
Mitochondrial area
Mitochondrial aspect ratio
Class I
Class II
Class III
WT-P10
TfamcKO-P10
WT-P14
TfamcKO-P14

Figure S7

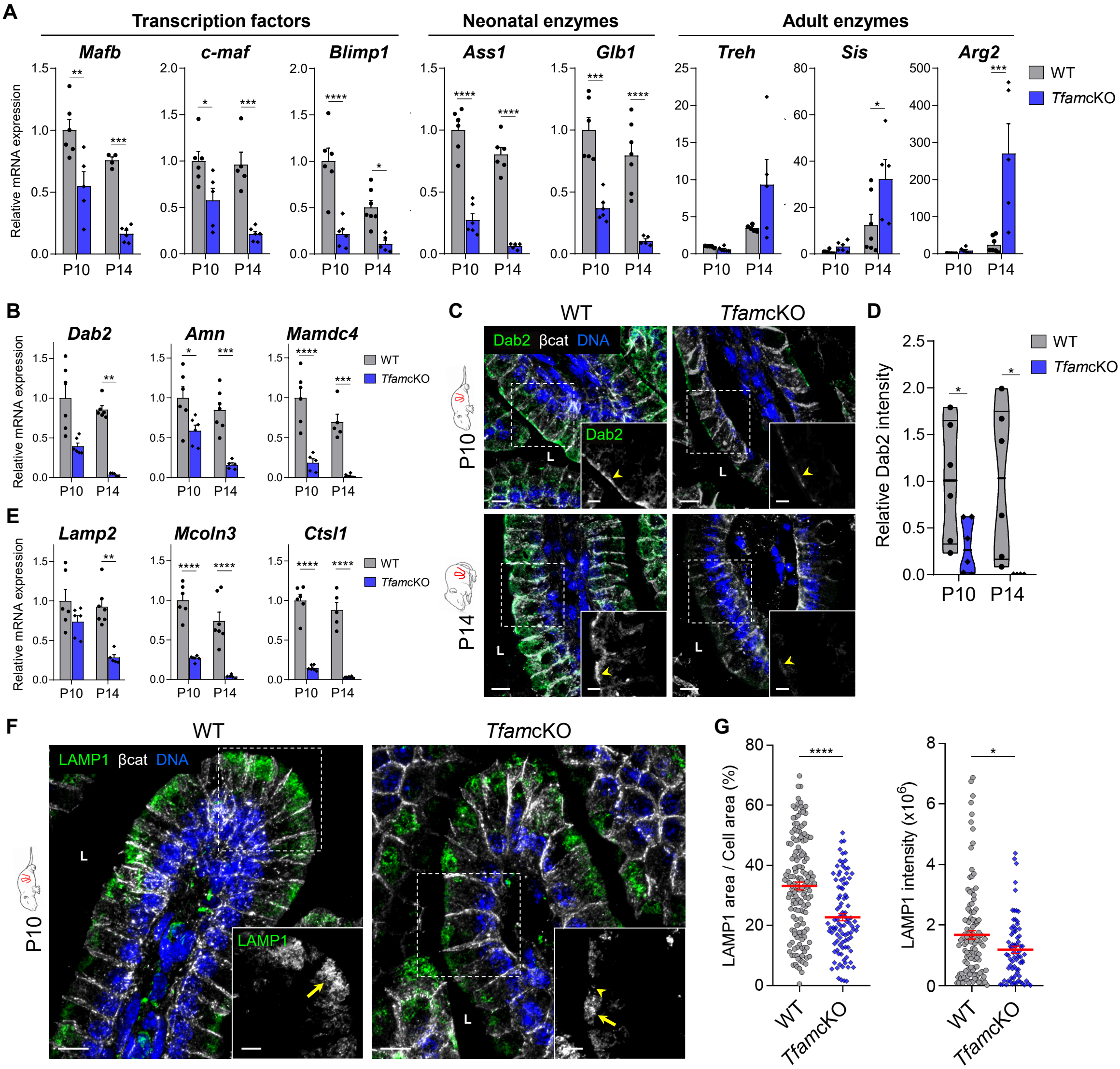
A
Transcription factors
Neonatal enzymes
Adult enzymes
Mafb
c-maf
Blimp1
Ass1
Glb1
Treh
Sis
Arg2
Relative mRNA expression
P10
P14
WT
TfamcKO
B
Dab2
Amn
Mamdc4
C
WT
TfamcKO
Dab2 βcat DNA
Dab2
L
P10
P14
D
Relative Dab2 intensity
E
Lamp2
Mcoln3
Ctsl1
F
LAMP1 βcat DNA
LAMP1
G
LAMP1 area / Cell area (%)
LAMP1 intensity (x10^6)

Table S1

	Class	No. mitochondria / μm^2	% of mitochondria	Mitochondrial area	Mitochondrial aspect ratio
Figure 4C	I	11, 10	11, 10	239, 271	239, 276
	II	11, 10	11, 10	13, 32	12, 28
	III	11, 9	11, 10	14, 12	18, 12
Figures 6F and S6P	I	23, 24, 13, 17	23, 24, 13, 17	184, 321, 259, 128	169, 329, 251, 130
	II	23, 24, 13, 17	23, 24, 12, 17	19, 73, 14, 45	21, 74, 15, 44
	III	23, 24, 13, 17	23, 24, 13, 17	45, 78, 17, 134	47, 78, 16, 149

Table S2

Protein	Figure 5H		Figure 6L	Figure S5E
	WT vs *Atg16*cKO	WT-P14 vs WT-Preadult		
ASS1	*	****	***	***
GLS	*	****	****	**
HK1	***	**	**	–
CPT1A	*	****	***	****
ACAC	NS	****	***	**
CS	****	****	***	****
IDH2	****	****	****	*
ATP5A	NS	****	*	NS